REPORT DOCUMENTATION PAGE

Form Approved OMB NO. 0704-0188

1. REPORT DATE (DD-MM-YYYY)	2. REPORT TYPE	3. DATES COVERED (From - To)
11-04-2013	Final Report	13-Aug-2009 - 12-Jan-2013

4. TITLE AND SUBTITLE

Final Report: Understanding Coatings that Protect Plasmonic Structures for Materials Characterization and Detection and Identification of Chemical, Biological and Explosive Agents

5a. CONTRACT NUMBER

W911NF-09-1-0424

5b. GRANT NUMBER

5c. PROGRAM ELEMENT NUMBER

611102

6. AUTHORS

Rebecca Agapov, Mark D. Foster

5d. PROJECT NUMBER

5e. TASK NUMBER

5f. WORK UNIT NUMBER

7. PERFORMING ORGANIZATION NAMES AND ADDRESSES

University of Akron
382 Carroll Street

Akron, OH 44325 -

8. PERFORMING ORGANIZATION REPORT NUMBER

9. SPONSORING/MONITORING AGENCY NAME(S) AND ADDRESS(ES)

U.S. Army Research Office
P.O. Box 12211
Research Triangle Park, NC 27709-2211

10. SPONSOR/MONITOR'S ACRONYM(S)

ARO

11. SPONSOR/MONITOR'S REPORT NUMBER(S)

55325-MS.9

12. DISTRIBUTION AVAILIBILITY STATEMENT

Approved for Public Release; Distribution Unlimited

13. SUPPLEMENTARY NOTES

The views, opinions and/or findings contained in this report are those of the author(s) and should not contrued as an official Department of the Army position, policy or decision, unless so designated by other documentation.

14. ABSTRACT

We have elucidated the means by which an Al2O3 protective coating prevents chemical and mechanical degradation of a silver plasmonic structure to enable Tip Enhanced Raman Spectroscopy for high resolution, high sensitivity characterization of nanostructures and detection of threats. The protective coating is very effective for measurements in air, preventing chemical degradation of the underlying silver plasmonic structure even after three months of aging. In addition, the protection is partially effective in aqueous environment. Notably, detection of

15. SUBJECT TERMS

Raman, TERS, Atomic Force Microscopy

16. SECURITY CLASSIFICATION OF:			17. LIMITATION OF ABSTRACT	15. NUMBER OF PAGES	19a. NAME OF RESPONSIBLE PERSON
a. REPORT	b. ABSTRACT	c. THIS PAGE			Mark Foster
UU	UU	UU	UU		19b. TELEPHONE NUMBER: 330-972-5904

Report Title

Final Report: Understanding Coatings that Protect Plasmonic Structures for Materials Characterization and Detection and Identification of Chemical, Biological and Explosive Agents

ABSTRACT

We have elucidated the means by which an Al2O3 protective coating prevents chemical and mechanical degradation of a silver plasmonic structure to enable Tip Enhanced Raman Spectroscopy for high resolution, high sensitivity characterization of nanostructures and detection of threats. The protective coating is very effective for measurements in air, preventing chemical degradation of the underlying silver plasmonic structure even after three months of aging. In addition, the protection is partially effective in aqueous environment. Notably, detection of different non-Raman resonant polymer isotopes at the surface was demonstrated for the first time and a new technique developed to independently measure isotopic compositions in the top monomolecular layer of a blend film using mass spectrometry. This technique we call Surface Layer-Matrix Assisted Laser Desorption/Ionization Time-of-Flight Mass Spectrometry (SL-MALDI-ToF MS).

Enter List of papers submitted or published that acknowledge ARO support from the start of the project to the date of this printing. List the papers, including journal references, in the following categories:

(a) Papers published in peer-reviewed journals (N/A for none)

Received		Paper
04/11/2013	7.00	Rebecca L. Agapov, Alexei P. Sokolov, Mark D. Foster. Protecting TERS probes from degradation: extending mechanical and chemical stability, Journal of Raman Spectroscopy, (02 2013): 0. doi: 10.1002/jrs.4268
08/22/2011	3.00	Rebecca L. Agapov, Andrey V. Malkovskiy, Alexei .P. Sokolov, Mark D. Foster. Prolonged Blinking from TERS Probes, J. Phys. Chem. C, (04 2011): 8900. doi:
08/28/2012	4.00	Shih-Fan Wang, Xiaopeng Li, Rebecca L. Agapov, Chrys Wesdemiotis, Mark D. Foster. Probing Surface Concentration of Cyclic/Linear Blend Films Using Surface Layer MALDI-TOF Mass Spectrometry, ACS Macro Letters, (08 2012): 1024. doi: 10.1021/mz300271w
TOTAL:	**3**	

Number of Papers published in peer-reviewed journals:

(b) Papers published in non-peer-reviewed journals (N/A for none)

Received		Paper
TOTAL:		

Number of Papers published in non peer-reviewed journals:

(c) Presentations

Agapov, R.L., Sokolov, A.P., Foster,M.D., "Protected tip enhanced Raman spectroscopy probes for the study of polymer surfaces," ACS Fall Meeting, Philadelphia, PA, Aug 19-23, 2012.

Agapov, R.L., Scherger, J., Foster,M.D. "Robust Plasmonics for High-Resolution Chemical Imaging," Trilateral Conference, The University of Akron, Akron, OH, June 21-22, 2012.

Li, X.; Wang, S-F., Agapov, R.L., Foster, M.D., Wesdemiotis,C. "Surface MALDI-ToF Mass Spectrometry: In-Situ Characterization of Polymer Surfaces Composition in Polymer Blend Films," ASMS 2012, Vancouver, BC, Canada, May 20-24, 2012.

Agapov, R.L., Foster, M.D., "Robust plasmonics for high-resolution chemical imaging," Eastman Chemical Co, Invited talk, May 22, 2012.

Agapov, R.L., Scherger, J., Foster,M.D., "Robust Plasmonics for High-Resolution Chemical Imaging," MSNO May Conference, John Carroll University, University Heights, OH, May 23, 2012.

Agapov, R.L., Sokolov, A.P., Foster, M.D., "Robust probes for high-resolution chemical detection and imaging," SPIE Defense Security & Sensing, Baltimore, MD April 23-27, 2012.

Agapov, R.L., Sokolov, A.P., Foster,M.D., "Protected TERS Probes for the Study of Polymer Surfaces," APS March Meeting, Boston, MA Feb 27-Mar 2, 2012.

Agapov, R.L., Sokolov, A.P., Foster, M.D. "Mechanically and Chemically Robust TERS Probes," Dept. of Polymer Science Sponsor's Day. The University of Akron, Akron, OH, Oct. 6, 2011.

Wang, S-F., Li, X., Agapov, R.L., Wesdemiotis, C., Foster, M.D. "Probing Surface Concentration of Cyclic/linear Blend Films Using Surface MALDI-TOF Mass Spectrometry," Dept. of Polymer Science Sponsor's Day. The University of Akron, Akron, OH, Oct. 6, 2011.

Number of Presentations: 9.00

Non Peer-Reviewed Conference Proceeding publications (other than abstracts):

Received		Paper
08/28/2012	5.00	Rebecca L. Agapov, Alexei P. Sokolov, Mark D. Foster. Robust Probes for High Resolution Chemical Imaging and Detection, Scanning Microscopies 2012: Advanced Technologies for Defense, Homeland Security, Forensic, Life, Environmental, and Industrial Sciences, Proceedings of SPIE Vol. 8378. 2012/04/24 00:00:00, . : ,
08/28/2012	6.00	Rebecca L. Agapov, Alexei P. Sokolov, Mark D. Foster. Protected Tip Enhanced Rasman Spectroscoy Probes for the Study of Polymer Surfaces, Polymer Preprints (American Chemical Society, Division of Polymer Chemistry) . 2012/08/19 00:00:00, . : ,
TOTAL:	**2**	

Number of Non Peer-Reviewed Conference Proceeding publications (other than abstracts):

Peer-Reviewed Conference Proceeding publications (other than abstracts):

Received	Paper

TOTAL:

Number of Peer-Reviewed Conference Proceeding publications (other than abstracts):

(d) Manuscripts

Received	Paper	
03/30/2011	1.00	R. Agapov, A. Malkovskiy, A. Sokolov, M. Foster. Prolonged Blinking with TERS Probes, (03 2011)
04/11/2013	8.00	Rebecca Agapov,, Jacob D. Scherger, Alexei P. Sokolov, Mark D. Foster, . Individual Detection of Isotopically Labeled Species in a Polymer Blend Using Tip Enhanced Raman Spectroscopy, ACS Macro Letters (11 2012)
TOTAL:	**2**	

Number of Manuscripts:

Books

Received	Paper

TOTAL:

Patents Submitted

Patents Awarded

Awards

Over the life of the grant:
Goodyear Tire and Rubber Fellowship
The University of Akron
September 2011
$7,500

Eastman Chemical Fellowship
Eastman Chemical Company
September 2011
$5,000

Personal Enrichment Grant from The University of Akron Graduate School
Feb 2012
Travel grant to attend APS Conference
$300

Department of Polymer Science Travel Grant
March 2012
Travel grant to attend SPIE Conference
$500

Graduate Students

NAME	PERCENT_SUPPORTED	Discipline
REbecca Agapov	1.00	
Jacob Scherger	0.50	
FTE Equivalent:	**1.50**	
Total Number:	**2**	

Names of Post Doctorates

NAME	PERCENT_SUPPORTED
FTE Equivalent:	
Total Number:	

Names of Faculty Supported

NAME	PERCENT_SUPPORTED	National Academy Member
Mark Foster	0.00	
FTE Equivalent:	**0.00**	
Total Number:	**1**	

Names of Under Graduate students supported

NAME	PERCENT_SUPPORTED
FTE Equivalent:	
Total Number:	

Student Metrics

This section only applies to graduating undergraduates supported by this agreement in this reporting period

The number of undergraduates funded by this agreement who graduated during this period:	0.00
The number of undergraduates funded by this agreement who graduated during this period with a degree in science, mathematics, engineering, or technology fields:.....	0.00
The number of undergraduates funded by your agreement who graduated during this period and will continue to pursue a graduate or Ph.D. degree in science, mathematics, engineering, or technology fields:.....	0.00
Number of graduating undergraduates who achieved a 3.5 GPA to 4.0 (4.0 max scale):	0.00
Number of graduating undergraduates funded by a DoD funded Center of Excellence grant for Education, Research and Engineering:	0.00
The number of undergraduates funded by your agreement who graduated during this period and intend to work for the Department of Defense	0.00
The number of undergraduates funded by your agreement who graduated during this period and will receive scholarships or fellowships for further studies in science, mathematics, engineering or technology fields:	0.00

Names of Personnel receiving masters degrees

NAME
Total Number:

Names of personnel receiving PHDs

NAME
Rebecca Agapov
Total Number: 1

Names of other research staff

NAME	PERCENT_SUPPORTED
FTE Equivalent:	
Total Number:	

Sub Contractors (DD882)

Inventions (DD882)

Scientific Progress

See pdf attachment of scientific progress report.

Technology Transfer

Executive Summary

Substantial progress on multiple goals of the project has been made in the final year as detailed below for each goal. The most important achievements and scientific conclusions for this project are:

1.) We have validated that an Al_2O_3 protective coating prevents chemical degradation of the underlying silver plasmonic structure even after three months of aging[1].
2.) We have confirmed that an Al_2O_3 protective coating prevents significant mechanical degradation to soft, underlying plasmonic structures even when scanning a hard silicon substrate[1].
3.) We have demonstrated that an Al_2O_3 coating slows the degradation of silver structures when exposed to an aqueous environment for two hours. When an adhesive layer of chromium is used under the protected silver film, the plasmonic structures resist delamination in both an aqueous environment and a salt water environment.
4.) We have demonstrated the detection of different isotopes of polymeric species by TERS for the first time using non-Raman resonant molecules. These studies were enabled using the extended lifetimes of Al_2O_3 protected silver probes.
5.) Since different isotopes could be detected, we developed a new technique to be able to independently measure isotopic compositions in the top monomolecular layer of a blend film at the UA laboratory using mass spectrometry. This technique we call Surface Layer-Matrix Assisted Laser Desorption/Ionization Time-of-Flight Mass Spectrometry (SL-MALDI-ToF MS)[2].
6.) First results indicate that gold conductive substrates for the SL-MALDI-ToF MS, which are costly and time-consuming to make, can be replaced with silver substrates without a loss in measurement capabilities.

Important subsidiary findings are:

1.) A protective SiO_x coating slows, but does not completely prevent chemical degradation to underlying silver structures after three months of aging[3].
2.) SiO_x coatings provide some protection from aqueous environments, but are not as efficient as Al_2O_3 coatings.
3.) The protection provided by diamond-like carbon coatings for plasmonic structures in both ambient and aqueous conditions proved to be inferior to that provided by SiO_x and Al_2O_3 coatings.

OBJECTIVE

The overall objective of this project is to develop material design principles for optimizing optically inactive ultrathin coatings that enhance the lifetimes of plasmonic structures useful for two transformational technologies: high resolution optical spectroscopies for characterization of material surfaces and very high sensitivity, highly selective detection of chemical, biological, and explosive threats in air or aqueous environments using surface enhanced Raman

spectroscopy (SERS). These plasmonic structures could be nanoparticles, nanoparticle arrays or clusters, rough coatings on scanning probe tips, or complex compound structures. The specific goals are to i.) characterize the chemical composition, density, and roughness of ultrathin protective coatings, ii.) quantify changes in the optical spectra of tips with plasmon structures before and after deposition of a protective coating, iii.) determine to what degree a protective coating prevents morphological changes in plasmonic structures on tips with heating, iv.) define the reduction in tip wear during imaging that the protective coating can offer, v.) demonstrate how such coatings can improve plasmonic structure robustness in aqueous environments, and vi.) define how addition of a coating changes (if at all) the spatial distribution of enhancement in plasmonic structures. The study focuses on alumina coatings.

In pursuing the general objective of developing material design principles for optimizing optically inactive ultrathin coatings that enhance the lifetimes of plasmonic structures we have identified four specific subgoals under goal vi, vi_a.) gain understanding of the geometry of hot spots in plasmonic structures, vi_b.) define the role of "blinking" in the enhancement achieved with coated plasmonic structures, vi_c.) determine the detection limit obtainable with TERS blinking for polymeric samples, and vi_d.). determine if TERS blinking data can be quantified to determine the surface composition of polymer blends. These specific goals are related to goal vi since they involve understanding from where on the plasmonic structure the predominant enhancement comes.

Experimental Methods:

Tip preparation:

Protected metallized tips were prepared by sequential physical vapor deposition at 10^{-5} Torr pressure of nominally 50 nm silver (Ag) and then 2-3 nm aluminum (Al) or silicon monoxide (SiO) onto Sharp Microlevers™ silicon nitride tips (earlier from Park Scientific, most recently from Veeco). Unprotected tips (with Ag only) were prepared for comparison. Thickness was monitored with a Sycon (STM-100) quartz-crystal microbalance. Silver and aluminum or silicon monoxide were evaporated from separate tungsten boats. A deposition rate of 1.0-1.5 Å/s was used for Ag deposition and a rate of 0.5 Å/s was used for the Al or SiO. The adhered Al layer easily generates a passivating alumina (Al_2O_3) coating due to the high reactivity of Al with environmental O_2 under normal conditions[4]. Alumina is transparent and has a very low porosity and high chemical stability.

Composite samples of alumina (or silicon oxide) coating on silver film on a flat silicon wafer were made for study with X-ray reflectivity (XR) and atomic force microscopy (AFM). While TERS and SERS-based detection techniques require the rough metal films that result from dewetting, the silver films for X-ray photoelectron spectroscopy (XPS) and XR study were made thick enough to avoid dewetting, since smooth, planar films were needed for those techniques. The preparation conditions for these flat samples were the same as outlined for the tips above.

Diamond-like carbon (DLC) coatings were also investigated as a possible protective coating for plasmonics. DLC films were fabricated on silver films on a silicon substrate as well as on silver metallized probes. The fabrication of the metallized tips and silicon substrates is described above. The DLC films were fabricated with the assistance of Rich Fowler (Timken Co.) and Edward Evans (The University of Akron) using plasma enhanced chemical vapor deposition (PE-CVD) using an argon plasma and acetylene (C_2H_2) gas. The PE-CVD chamber was pumped

to a vacuum of 1.3 x 10^{-5} Torr and then backfilled with argon and held at a pressure of 5 mTorr. A sample bias of 650 V was applied. Etching of the surface was performed with 650 V bias for 60 s with a 40 standard cubic cenimenters per minute (sccm) flow rate of argon. This etching step was performed to heat the sample before deposition in an attempt to improve the adhesion between the silver layer and the DLC film[5]. (Early samples made without this etching step were not mechanically stable.) A pulse of 1.6 µs at 250 kHz was used. The flow of an argon and acetylene (C_2H_2) gas mixture in the deposition chamber during deposition was held at a total flow rate of 80 sccm. The exact gas flow rate for each of the mixture components during deposition are listed in Table 1 along with the DLC deposition time.

Table 1. Gas flow rates and deposition times for the DLC coating films.

Run Number	Argon Flow Rate (sccm)	C_2H_2 Flow Rate (sccm)	Deposition Time (s)
1	16	64	10
2	32	48	15
3	40	40	20
4	48	32	25
5	64	16	25
6	0	80	10

Instrumentation for Surface Enhanced Raman Scattering (SERS) and Tip Enhanced Raman Spectroscopy (TERS)

The instrument for TERS used in this work includes a Horiba Jobin Yvon Labram HR-800 Raman spectrometer optically coupled with a Quesant (QScope 250) atomic force microscope using a long-working distance Mitutoyo (APO SL50) objective (50X, 0.42 NA). A detailed description of the instrument is presented elsewhere[6, 7]. To measure the optical properties of the tips we used a trapezoidal quartz prism under the AFM head and a white light beam that illuminates the top surface of the prism under the angle of the total internal reflection. It creates an evanescent field above the prism surface that excites emission from the apex of a tip brought in contact with that surface. The complete set-up and procedure to measure the optical properties are presented in our previous work[3]. Optical resonance spectra were measured for both metallized tips and protected metallized tips. Detailed descriptions of the experimental setups for TERS measurements and measurements of the tips' optical properties have been presented elsewhere[6, 7].

Goal 1: Characterizing morphology and structure of as-deposited coating:

Goal 1a: Characterizing morphology and structure of as-deposited coating in fresh films

Composite samples of alumina coating on silver film on a silicon wafer substrate were made for study with X-ray photoelectron spectroscopy (XPS) and AFM. While TERS and SERS-based detection techniques require the rough metal films that result from dewetting, the silver

films for XPS study were made thick enough to avoid dewetting, since smooth, planar films were needed for this technique. The XPS spectrum of a fresh alumina coated silver film is compared with that from a fresh silver reference film in Fig. 1. (The increase in the background of the alumina protected silver film from 400 to 700 eV is due to fact that this system is a bilayer. The alumina layer is less conductive than the metal layer and some of the electrons that should be present in the silver peak are therefore trapped in the background.) Analysis of the spectrum indicates the concentration of aluminum is 8 at % and that of oxygen is 15 at %. When the oxygen percentage is corrected by subtracting the amount of oxygen adsorbed onto the surface of the silver film, a ratio of Al:O of 2:3 was found, confirming the anticipated oxide stoichiometry.

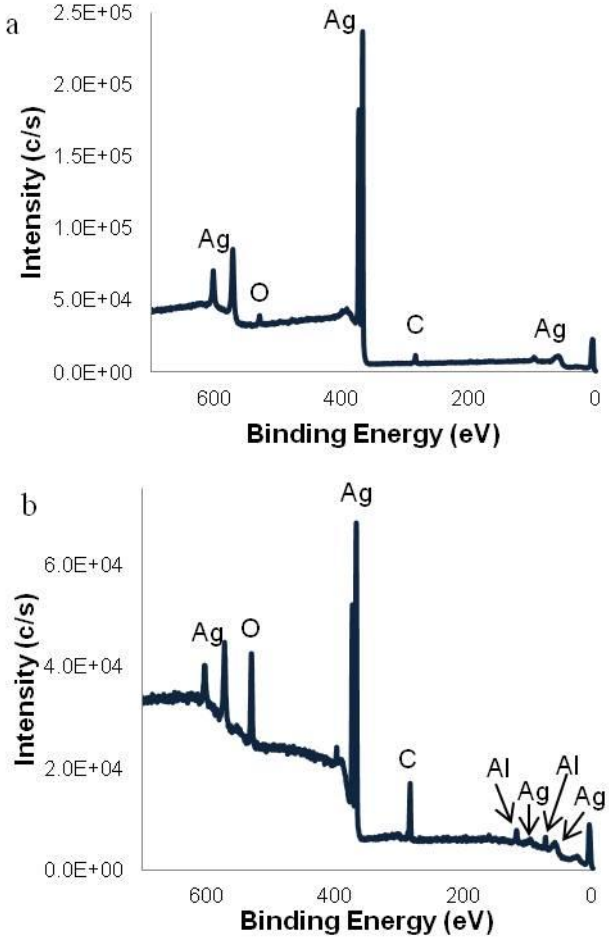

Figure 1. XPS spectrum from a fresh a) silver film on a flat silicon wafer and b) an alumina protected silver film on a flat silicon wafer. When the differing sensitivities of XPS for the various elements are accounted for, the peak areas for the Al and O peaks correspond to a stoichiometry of 2:3.

A further confirmation of the nature of the coating can be made by analysis of the exact binding energy of the aluminum peak. Aluminum in the form of an oxide has a 2p peak that appears at 75 eV and a 2s peak that appears at 117.9 eV. Metallic aluminum has a peak that appears at 73 eV instead of 75 eV [8, 9]. A magnified view of the aluminum peaks from the XPS spectrum in Fig. 1b is presented in Fig. 2. The peaks from the aluminum species present on the Al_2O_3 protected silver film appear at 75.2 eV and 117.9 eV, confirming that the protective

coating is an oxide.

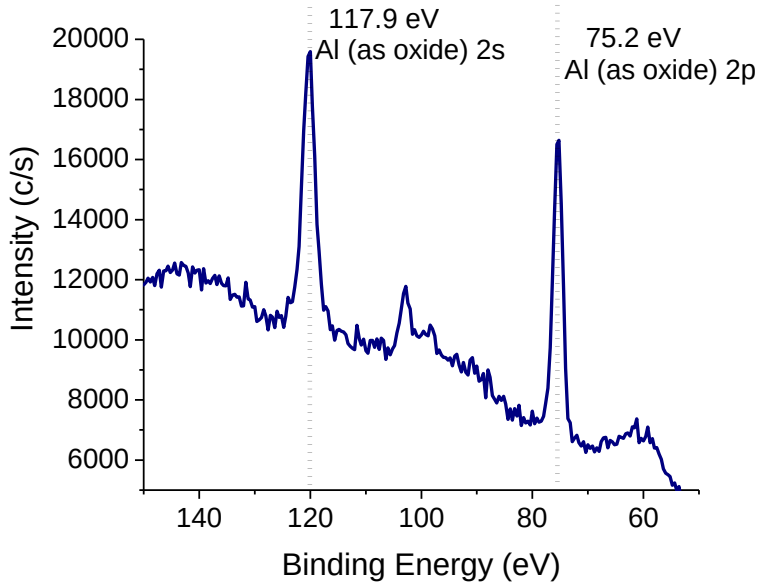

Figure 2. XPS spectrum highlighting the aluminum peaks from an Al_2O_3 protected silver film spectrum shown in Fig. 1b. The peaks at 75.2 eV from the aluminum oxide 2p signal and at 117.9 eV from the aluminum oxide 2s signal confirm that the protective coating is aluminum oxide.

The root-mean-square (RMS) surface roughnesses of the films on flat substrates were defined locally by AFM. The metal surface was imaged with and without deposition of the protective coating and tracked as a function of time over the course of a month. The local roughnesses of the film without a protective coating and of the film with a protective coating are shown in Fig. 3 as a function of time. The roughness data for each data point were obtained from three 5μm x 5 μm scans on the film surface. The local roughness did not change significantly over a month for either the pure silver or protected silver film. The pure silver films have an average RMS roughness of 2.0 (± 0.2) nm while the protected silver films have an average RMS roughness of 1.6 (± 0.3) nm. Replicate measurements on two additional films of the same type showed the same trends. We conjecture that the protected films are slightly smoother because deposition of the additional layer has a small smoothing effect. However, this smoothing effect has not been observed to significantly decrease the enhancement observed from these films[10].

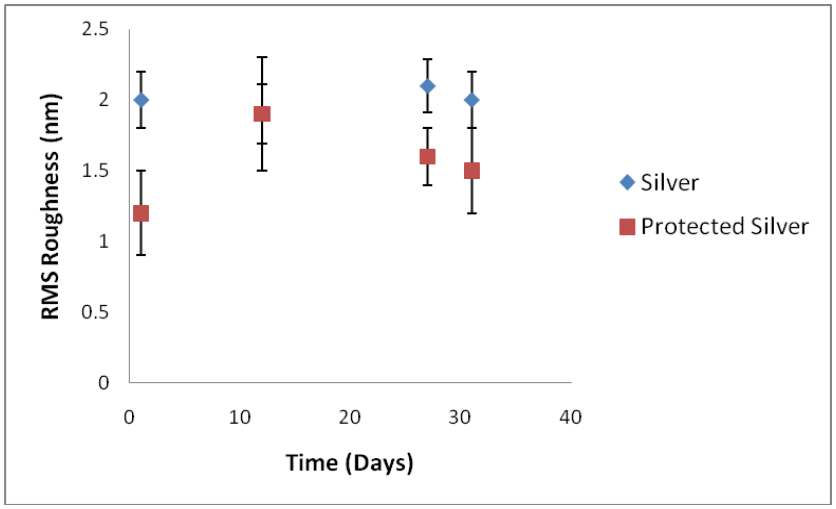

Figure 3. RMS roughness of a pure silver film (diamonds) and an alumina protected silver film (squares) as a function of time. No significant change in the local surface roughness was observed over a month.

To obtain global information about the films, x-ray reflectivity (XR) was performed. The reflectivity curve for a 20 nm silver film on a silicon wafer is shown along with the reflectivity curve for a 2.5 nm Al_2O_3 protected silver film in Fig. 4. From the raw data, it is obvious that the metal film is rough and that this roughness persists to a considerable extent after the protective layer has been added. The Kiessig fringes die off for the metal film much faster than for the protected metal film indicating that the unprotected silver film is rougher than the protected silver film, consistent with the observations from AFM.

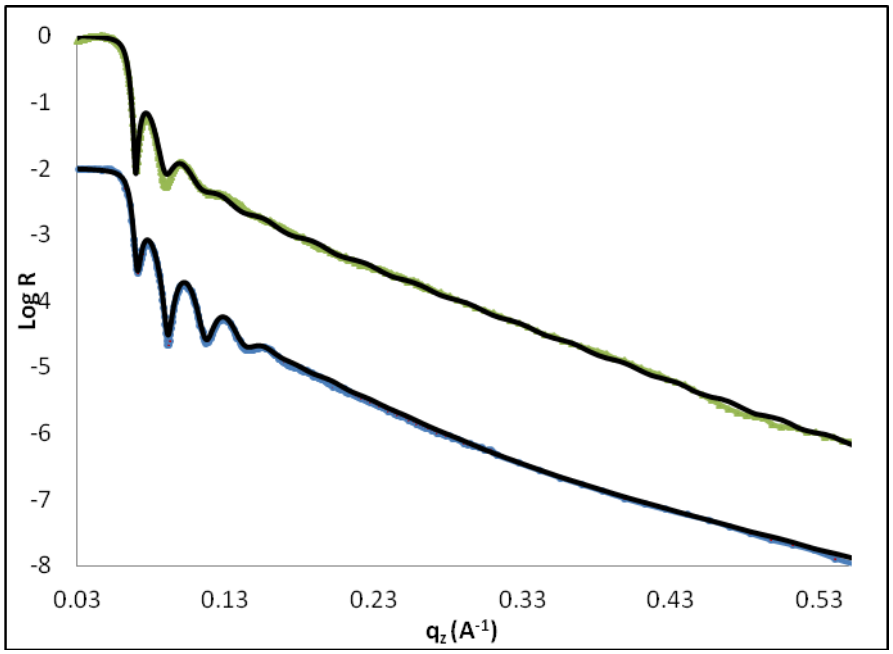

Figure 4. Experimental reflectivity and best fit (black line) for a silver film (green symbols) and an alumina protected silver film (blue symbols). The data for the protected silver film have been shifted down by two orders of magnitude for clarity.

The scattering length density (SLD) profiles for the two films are shown in Figure 5 and differ markedly. A high electron density region is observed at the interface between the silver and the native silicon oxide layer from the silicon substrate. This region, which most likely is a result of a small amount of contamination in the vapor deposition chamber, is not exactly the same thickness and does not have the exact same electron density in the two samples. The silver film shows a flat plateau around 7.42 x 10^{-5} Å^2 that corresponds to silver. The calculated SLD for pure silver is calculated to be 7.75 x 10^{-5} Å^2. The observed SLD is lower than expected due to the gaps between the silver metal being filled with air and lowered the average SLD. This is also consistent with several other groups that found that thin silver films have a lower SLD than calculated[11, 12]. The SLD for the silver film drops near the air/metal interface. A very broad interface is observed due to the film roughness at the air interface. In contrast, the SLD profile for the alumina protected silver film never reaches a plateau corresponding to the SLD of pure silver. This might be explained by postulating that two regions of contamination are observed, one layer of contamination that corresponds to each set of electrodes that the metals are deposited from. A 27 Å thick layer is observed that has a SLD of 2.2 x 10^{-5} Å^2 which corresponds well with the calculated SLD of the Al_2O_3 layer which is 2.27 x 10^{-5} Å^2. This layer near the air surface reduces the overall roughness of the film and smoothes the air/metal interface, consistent with the local smoothing that was observed via AFM.

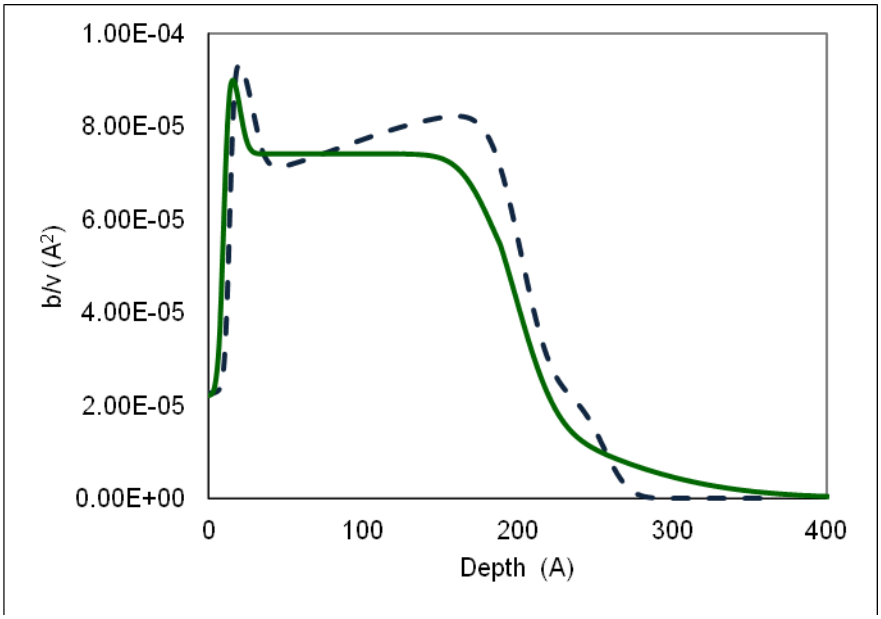

Figure 5. The SLD profiles for a silver film (solid green) and an alumina protected silver film (dashed blue). Zero on the depth scale corresponds to the interface between the silicon substrate and its oxide layer.

The surface roughnesses of the flat films were quantified by AFM (locally) and XR (globally). The surface roughness from XR measurements was found to be 27 Å for the unprotected silver film and 13 Å for the alumina protected silver film. From local AFM measurements, the silver film had a root mean square roughness of 20 (± 2) Å, while the alumina protected film had a roughness of 16 (± 3) Å.

An off-specular longitudinal scan was used to quantify the degree of conformality with which the alumina protective coating covers the metal structure. This experiment was performed with a sample consisting of 30 nm of aluminum, 50 nm of silver, and 2.5 nm of Al_2O_3. The longitudinal scan was performed with an offset of 0.05° in two theta. The data from the specular scan and the longitudinal scan are shown in Figure 6. The first peak for each scan is nearly in phase; however, the additional peaks are slightly out of phase. The degree to which the peaks are out of phase increases as q_z increases. This indicates that the three layers are not completely conformal. This is consistent with TEM images that show that the protective coating does not follow the underlying metal layer exactly, but closely.

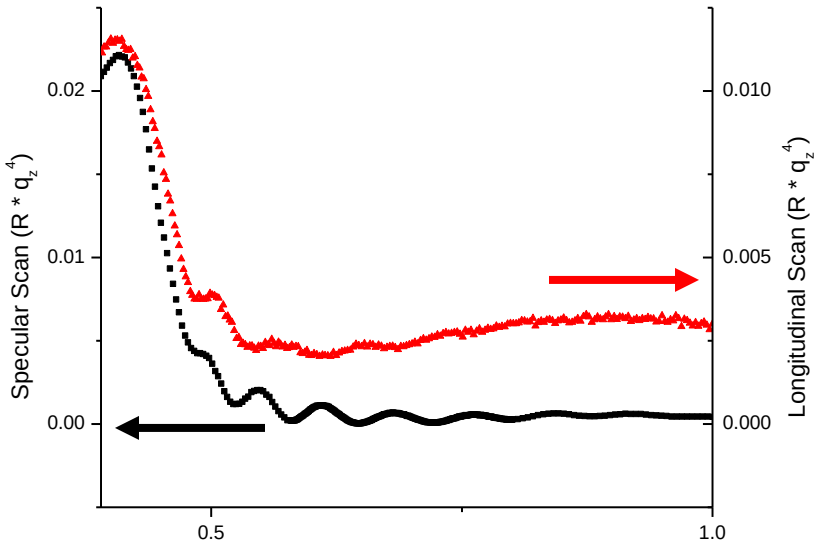

Figure 6. Comparison of a specular scan (black squares) with a longitudinal scan (red triangles) with two theta offset by 0.05° from a sample consisting of 30 nm aluminum, 50 nm of silver, and 2.5 nm of Al_2O_3.

Goal 1b : Characterizing morphology and structure of as-deposited coating in aged films:

XPS data were collected for silver films after three months (Fig. 7) and ten months (Fig. 9) of aging. The aged silver films contained an excessive amount (9-10 at %) of sulfur and chlorine contamination on the surface of the film. This contamination is indicative of degradation of the plasmonic structure that is detrimental to the enhancing capabilities of the silver film. To confirm the chemical composition of the contamination, the Auger peaks from the XPS spectrum were analyzed (Fig. 8). The kinetic energy of the Auger electron is related to the difference between the energy of the initial electronic transition and the ionization energy for the shell it was ejected from and therefore provides information about the binding between atoms. For the three month aged silver film Auger peaks appear at 1129.1 eV and 1134.3 eV. The energy of the Al K_α incident X-rays was 1486.7 eV. Therefore the Auger peaks are shifted 357.6 eV and 352.4 eV from the incident energy. This corresponds to metallic silver and silver (I) sulfide, respectively[8].

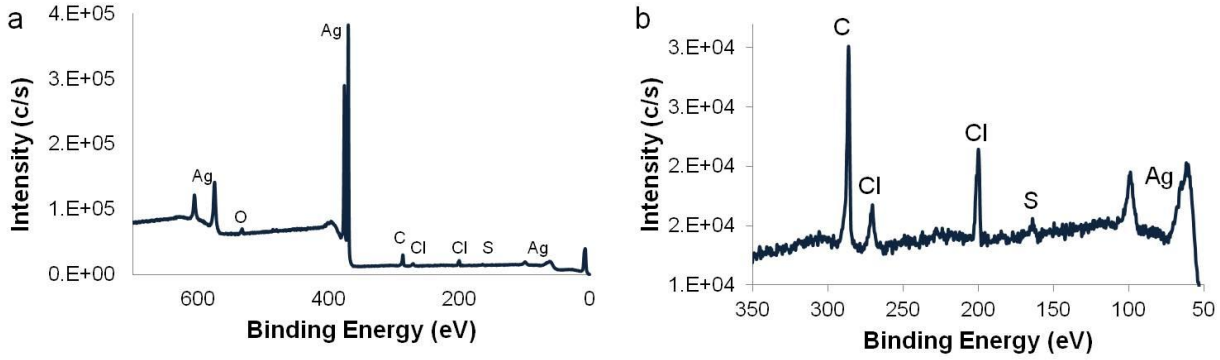

Figure 7. XPS spectrum of a silver film on a flat silicon wafer that was aged in a desiccator for three months shown a) full scale and b) magnified view of spectrum a) from 50 – 350 eV for clarity. Sulfur and chlorine contamination account for 9 at % of the film surface.

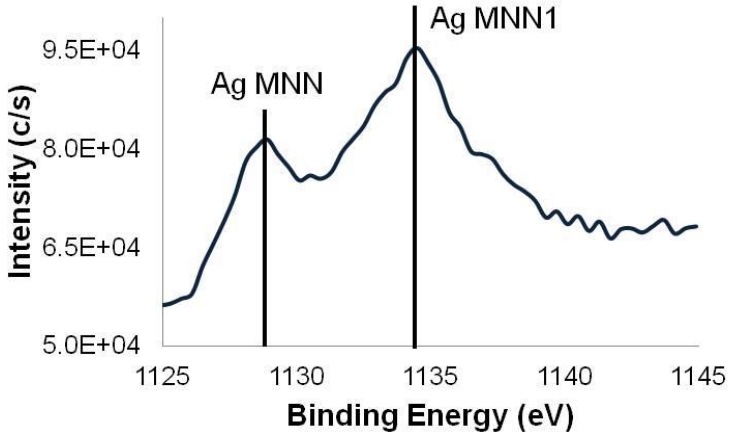

Figure 8. XPS spectrum of a 3 month aged silver film on a silicon wafer. This spectrum shows the Auger peak, which is consistent with metallic silver and silver sulfide, but not with silver oxide.

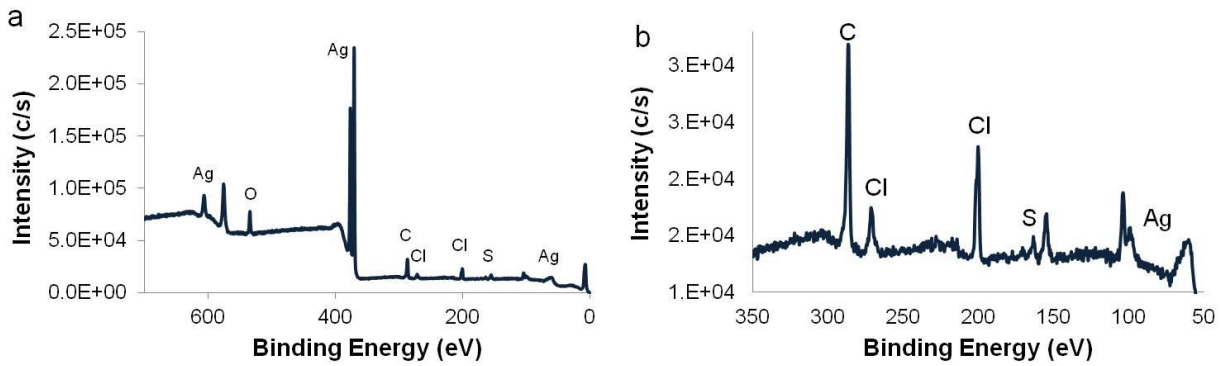

Figure 9. XPS spectrum from a ten month aged silver film on a silicon wafer displayed with a) full binding energy scan and b) magnified view of spectrum a) from 50 – 350 eV for clarity. Sulfur and chlorine contamination account for 10 at % of the film surface.

XPS data were also collected for both alumina protected and SiO_x protected silver films. The protective coating was 2.5 nm thick in both cases. The data for the SiO_x protected silver film that was aged for three months in a desiccator are shown in Fig. 10. The SiO_x coating did decrease the amount of sulfur and chlorine contamination observed as compared to the unprotected film. However, there is still ~1 at % of contamination observed. The data for the alumina protected silver film that was aged for three months in a desiccator are shown in Fig. 11. The alumina protective coating reduced the amount of sulfur contamination indicative of degradation to < 0.5 at % and reduced the amount of chlorine contamination to a barely detectable level even after three months of aging. This significantly increases the storage lifetime of the silver plasmonic structures.

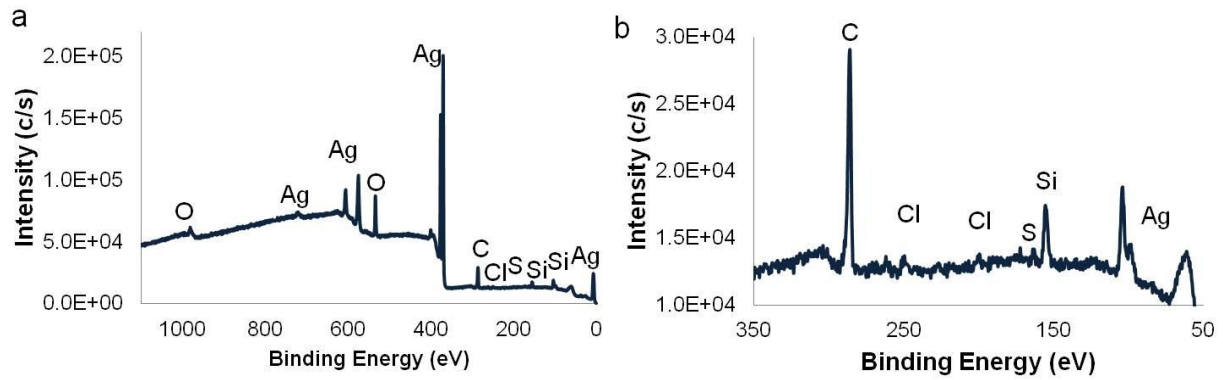

Figure 10. XPS spectrum from a SiO_x protected silver film on a silicon wafer that was aged for three months shown for a) full binding energy scan and b) magnified view of spectrum a) from 50 – 350 eV for clarity. Sulfur and chlorine contamination were detected, but in low quantities (~1% each).

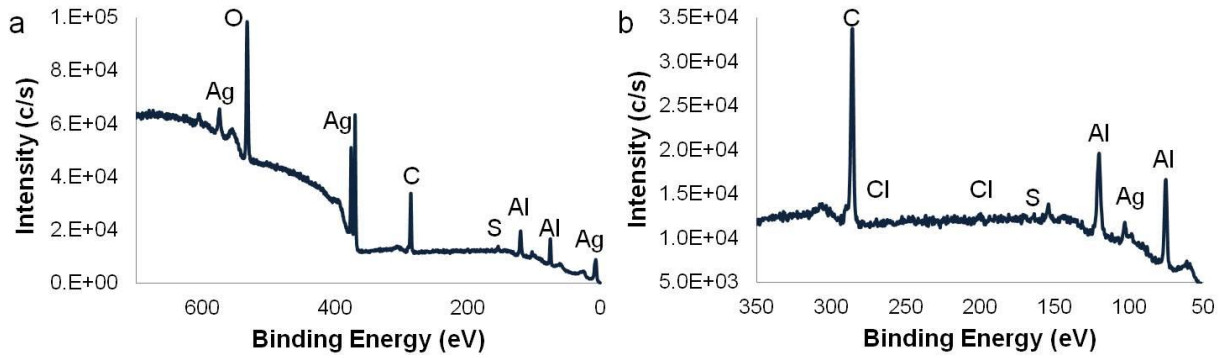

Figure 11. XPS spectrum of a three month aged Al_2O_3 protected silver film months shown for a) full binding energy scan and b) magnified view of spectrum a) from 50 – 350 eV for clarity. Chlorine and sulfur contamination are barely detectable, indicating that the alumina layer is protecting the underlying silver from chemical degradation.

Chemical changes to silver nanostructures has also been observed to cause significant morphological changes due to increased aggregation of individual nanoparticles[13, 14]. The film morphology of protected and unprotected silver films after three months of aging was therefore investigated. Analysis with AFM and scanning electron microscopy (SEM) of the morphologies of unprotected silver films after three months of storage in a dessicator revealed changes in the morphology of the plasmonic structure. SEM imaging of the silver film revealed the formation of depressions 50-100 nm in diameter. A representative image is presented in Fig. 12(a). AFM imaging of these depressed regions revealed that they were, on average, 8-10 nm deep. The increased height of the silver structures surrounding the depressed regions suggests that the silver from inside a depression accumulated around the edge. The aged silver film had an RMS surface roughness of 3.5 (± 0.4) nm compared to 2.0 (± 0.2) nm for a fresh silver film due to structure rearrangement. AFM and SEM analysis showed that, in contrast, the Al_2O_3 protected film did not undergo an observable morphology change with aging, as shown in Fig. 12(c,d). No depressions were observed and the morphology of the aged protected silver film was consistent with its "fresh" morphology. The roughness of the aged film, 1.7 (± 0.3) nm, was the same as that of the fresh protected film, 1.6 (± 0.3) nm. This indicates that the alumina protective coating acted as an impermeable barrier layer preventing chemical attack and rearrangement of the silver morphology, and therefore successfully extended the storage lifetime of the silver film to three months.

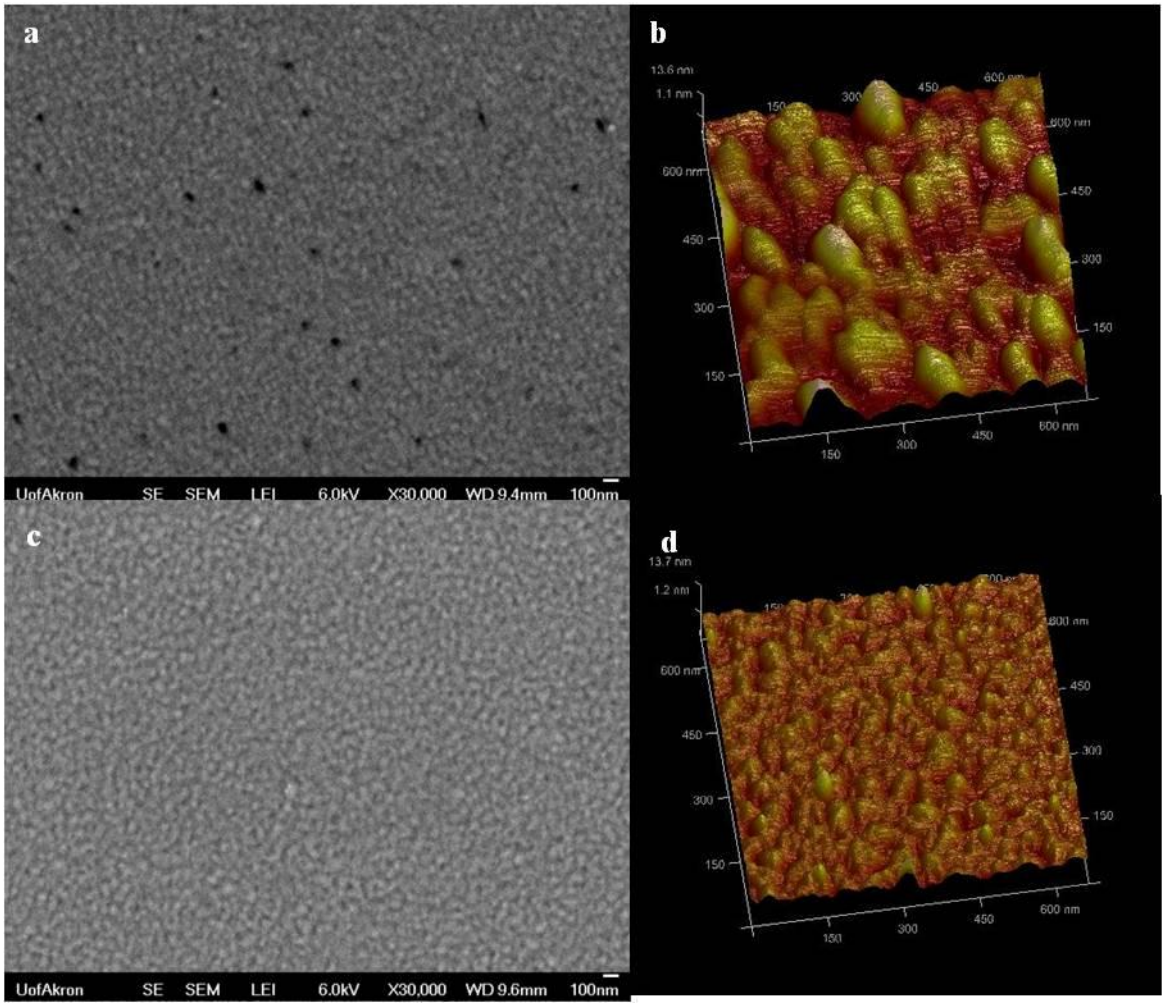

Figure 12. Images of the film morphologies after three months of aging in a desiccator: (a) SEM image of a silver film, (b) AFM 3-D image of a small region of a silver film showing morphology rearrangement (full z-range is 25 nm), (c) SEM image of an alumina protected silver film, and (d) AFM 3-D image of a small region of a protected silver film showing features of very similar heights (full z-range is 25 nm).

Goal 2: Quantification of changes in optical spectra with coating and over time:

Our team has demonstrated an unique capability to measure the optical response of an apex of a single tip[6] and this approach was used to determine the optical response in green (λ = 514.5 nm) light of both Ag-coated tips and tips carrying the protective coating. The same unique research instrument is used in two different configurations to perform apertureless scanning near-field optical microscopy (SNOM) imaging with a Raman signal and to measure the optical response. Changes in the entire optical spectrum were tracked as a function of time. This was done first for structures for which there was no degradation due to wear during scanning.

Batches of three metallized AFM probes and three alumina protected metallized AFM probes were tested. Data from one metallized probe are shown in Fig. 13 and from one of the protected

probes in Fig. 14. Spectra measured after a week of aging did not look like the spectra measured when the tips were "fresh". However, measurements pursued after the initial results were obtained clarified that even when a given tip was measured multiple times during the same lab session variations in the spectra could be seen. In some cases with multiple measurements a spectrum would first change and then change back to the original form. We conjecture that this may reflect a very high sensitivity to the precise part of the plasmonic structure that first contacts the surface when the tip is engaged with the prism. Therefore it needs to be recognized that these data are simply illustrative of the spectrum from a single probe. They may not accurately portray the "average" behavior of multiple probes of this type. The spectra collected for the different probes in one batch could show different numbers of peaks and even differences in peak position. This irregularity of behavior was observed for both metallized and protected probes. Further experiments with larger batches of tips are planned in hopes of being able to define a useful "average" behavior. We wish to underscore that we ***have*** achieved a comparatively high rate of success in obtaining enhancement with our tips. Almost all tips provide enhancement, with the degree of enhancement varying. However, it has become clear that the details of the optical spectrum are variable even among a group of enhancing tips.

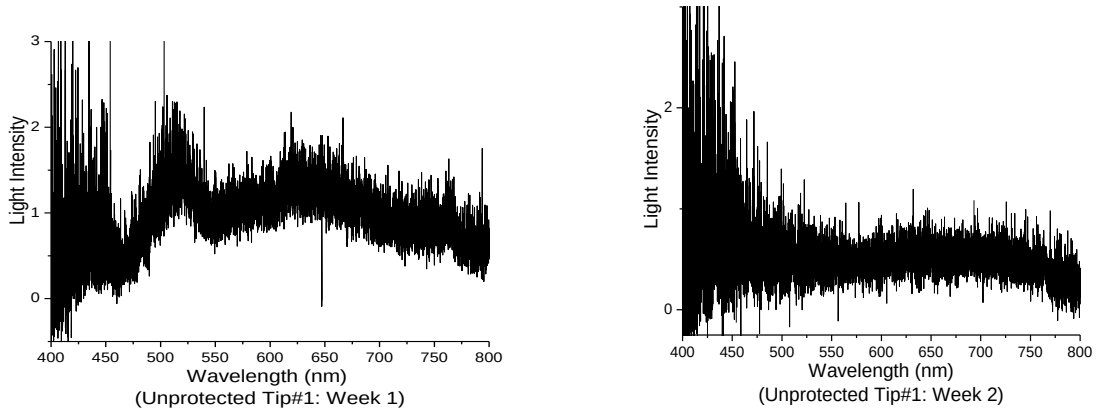

Figure 13. Optical spectra for a metallized AFM probe obtained on day 1 (left) and day 8 (right). The tip was stored in a desiccator between measurements. The optical spectrum was observed to change character after one week of aging.

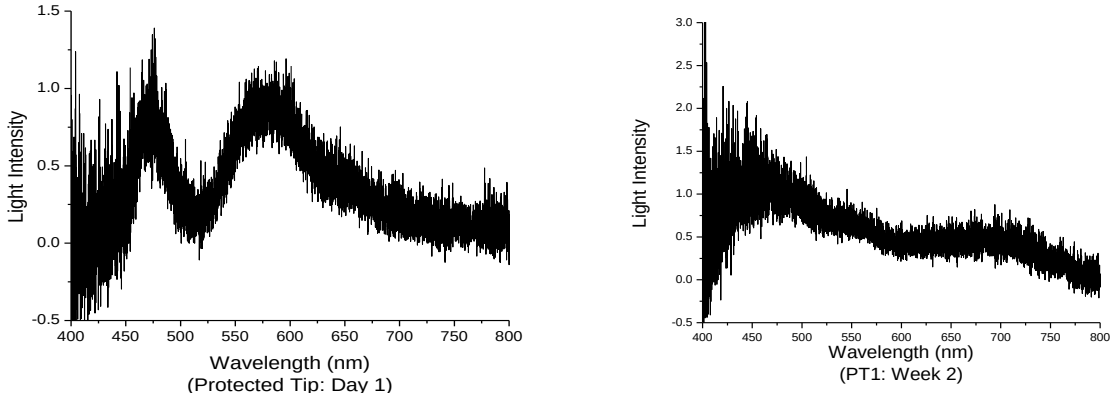

Figure 14. Optical spectra for a protected metallized AFM probe obtained on day 1 (left) and day 8 (right). The tip was stored in a desiccator between measurements. The optical spectrum was observed to change character after one week of aging.

Goal 3: Determine the effect of the protective coating on changes in plasmonic structures with heating:

The morphology of a metal film (protected and unprotected) on a planar (Si) substrate was monitored as a function of heating the sample with the laser beam. A silver film and an alumina protected silver film each on a flat Si substrate were subjected to heating by a 514 nm incident laser beam at various power levels for various lengths of time (Table 2). The two "exposed" films were imaged with AFM and their roughnesses compared to that of a silver film with no heat treatment. The incident power levels on the sample were varied from 1.5 mW to 0.32 mW. Due to the fact that it is difficult to observe heating damage in an area having the diameter of the laser beam (~1 μm), rows of spots exposed identically were created in the pattern shown in Fig. 15. Creation of this pattern of spots was facilitated by the use of a software driven, motorized XY stage. Each row of exposed spots had a width comparable to that of the laser beam and was 11 μm long. This ensured that the heated area could be accurately found relative to a marked starting point and imaged with AFM.

Table 2. Heating power and time for heat-treated silver and protected silver films.

Laser Power (mW)	Heating Time	Row Number
1.5	5 min, 1 min, 30 s	1, 2, 3
1.08	1 min, 30 s	4, 5
0.65	1 min, 30 s	6, 7
0.54	1 min, 30 s	8, 9
0.31	1 min, 30 s	10, 11

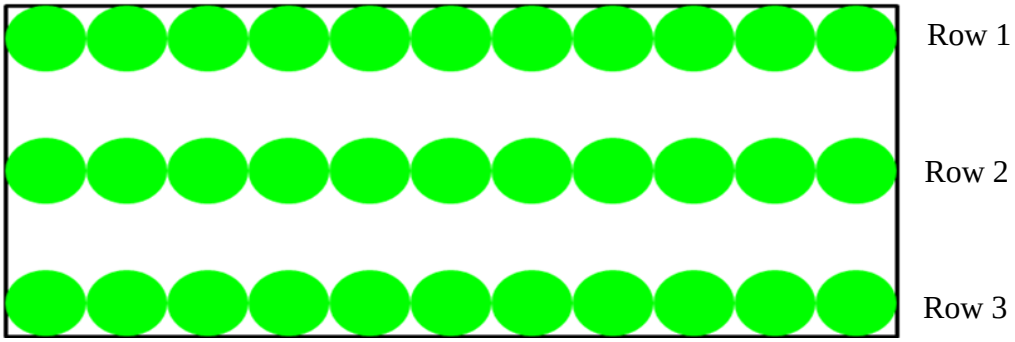

Figure 15. Schematic diagram of the rows of spots produced to test the effect of sample heating. Each spot in a given row was heated at the same laser power for the same period of time. Each spot has a diameter of 1 μm and each row is 11 μm long.

Selected images among those collected are shown in Fig. 16. Only the silver film heated at 1.5 mW for 5 min showed a noticeable morphology change. (This region is outlined by the red box in Fig. 16.) The remaining rows of exposed spots exhibited morphology that matched the morphology of the unheated silver film. The protected film showed no noticeable morphology changes for any of the laser powers or heating times investigated.

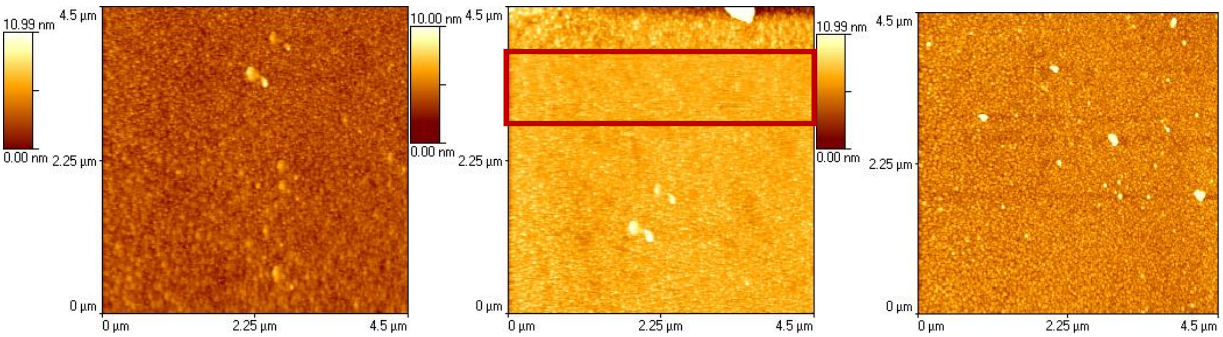

Figure 16. AFM images of an as-deposited silver film (left), a heat-treated silver film (center), and a heat-treated alumina protected silver film (right). Damage was only observed for the greatest exposure, 1.5 mW heating for 5 min, on the unprotected silver film. The damaged area is outlined in red in the center image. Other parts of the surface shown received less exposure. The roughness for the damaged region was 50% lower than the roughness for the undamaged region.

The change in morphology was characterized by measurements of local RMS surface roughness. The roughnesses for the unheated silver film and the heated alumina protected film shown in Fig. 16 were both 1.0 (± 0.2) nm. This is much higher than the 0.4 (± 0.1) nm observed for the deformed, heat-treated region on the silver film. A loss of roughness in a plasmonic structure has been associated with a loss of enhancement. For example, Zhang *et al.*[15] observed a loss in enhancement after a rough gold surface was heated with a ~ 1 mW incident beam for one minute.

The fact that no damage was observed in the film until 1.5 mW of power was applied indicates that the silver film applied to a flat silicon wafer is much more robust than a silver film applied to a square pyramidal AFM probe. Silver structures on AFM tips degraded upon application of much lower laser powers (see Goal 4 below). Efforts were made to ensure that the roughness of the samples on the Si substrate was comparable to the roughness observed on a tip. This results in similar contrasts (see Eq. 2 below) from both the wafers and the tips. The robustness of the silver film on the Si substrate can therefore be attributed to the increased ability to dissipate heat through the flat substrate compared to the heat dissipation through the AFM tip.

Goal 4: Definition of effect of coating on tip wear during imaging.

SEM and transmission electron microscopy (TEM) (using a special stage we have designed) was used to monitor the changes in the morphology of unprotected and protected tips with wear during analysis of standard samples. For reference, images of a metallized tip and a protected metallized tip that have not been used (i.e. no laser illumination or sample contact) are shown in Fig. 17. The protective alumina coating on the tip in Fig. 17b is ~3 nm thick.

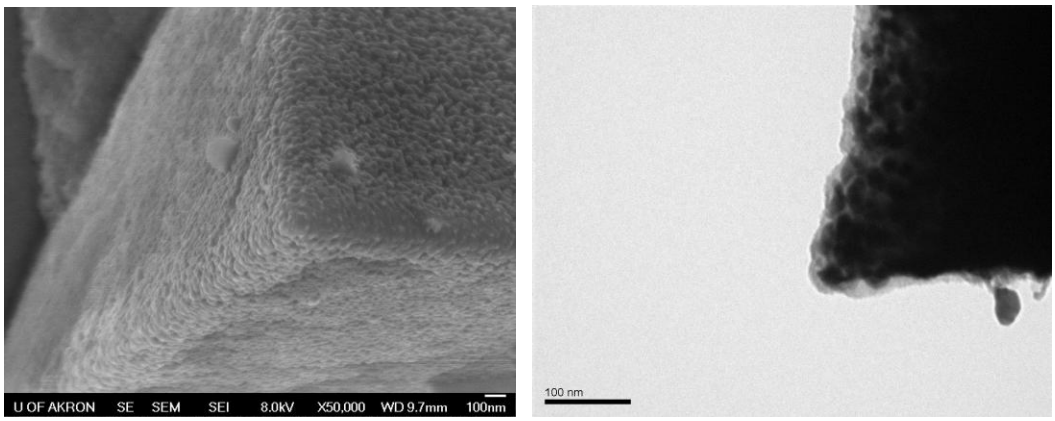

Figure 17. SEM image of a metallized AFM probe (left) and TEM image of an alumina protected metallized AFM probe (right) with no imaging induced wear.

Images of tips after a single approach/ withdraw cycle to collect the Raman spectrum from a polymer are shown in Fig. 18. The tips were exposed to the laser beam continuously for 30 min while data were being acquired. The laser power was 0.4 mW for all tips. From the images, it is obvious that plasmonic structures on the two unprotected tips have degraded while the alumina protected tip is still intact. On the tip in Fig. 18a the critical roughness characteristic of an effective plasmonic structure has been smoothed away by heating of the structure. The tip in Fig. 18b has undergone mechanical degradation and portions of the plasmonic structure near the apex have been completely removed. The protected tip in Fig. 18c shows no evidence of thermal or mechanical damage to the plasmonic structure.

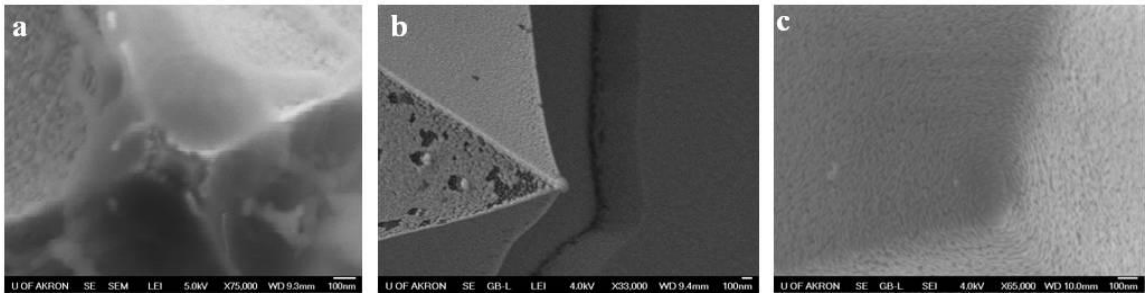

Figure 18. a,b) SEM images of metallized AFM probes and c) an alumina protected AFM probe after some use. After use, the unprotected tips show signs of smoothing of the plasmonic structure by a) thermal degradation and b) loss of portions of the structure by mechanical degradation. There is no evidence of degradation of the protected tip after the same amount of use.

Morphology changes in the plasmonic structure after the tips were used for *imaging* were investigated next. Metallized tips as well as alumina protected metallized tips were used to image a standard silicon grating (NT-MDT grid TGZ01). (These measurements were performed without an incident laser beam to separate the thermal and mechanical degradation mechanisms.) This silicon grating (Vickers Hardness 1260 MPa[16]) was harder than the silver plasmonic structure (Vickers Hardness 59 MPa[17]) and scanning it was expected to cause visible damage to

the tip. The silicon grid consisted of patterned stripes with a rectangular cross section, a 3.0 µm pitch, and a 25.5 nm step height (Fig. 19). For uniformity between tips, the same setpoint was used for each approach and the scans were performed with a constant scan rate of 1 Hz. The scans were performed in contact mode with the tips scanning perpendicular to the stripes with a 5 µm x 5 µm scan size. TEM images of metallized tips after zero, three, and six scans of the silicon grid are shown in Fig. 20. The images shown below are from three different tips, showing that the data are reproducible. The metallized tips increase in diameter from 46 (± 5) nm for the unused tip to 65 (± 7) nm after six scans. (The tip diameters were calculated using a radius of curvature macro in ImageJ (NIH, Version 1.42q).) A significant smoothing of the metallic structure covering the tip surface was also observed on several of the tips after image collection and can be seen in the tip in Fig. 20c. The loss of roughness in the plasmonic layer covering the tip reduces the tip's ability to enhance the Raman signal[15] making it an ineffective TERS probe.

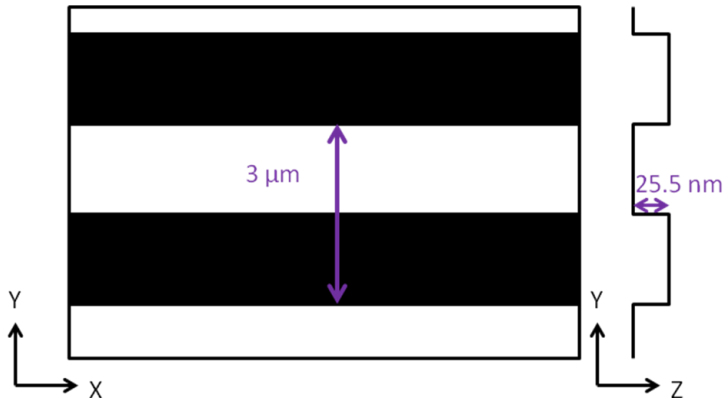

Figure 19. Schematic diagram of the TGZ01 standard silicon grid. A bird's eye view of the stripes in the x/y plane as well as a cross section in the y/z plane are presented. The grid has a pitch of 3 µm and a step height of 25.5 nm. The tips were scanned across the grid in the y direction.

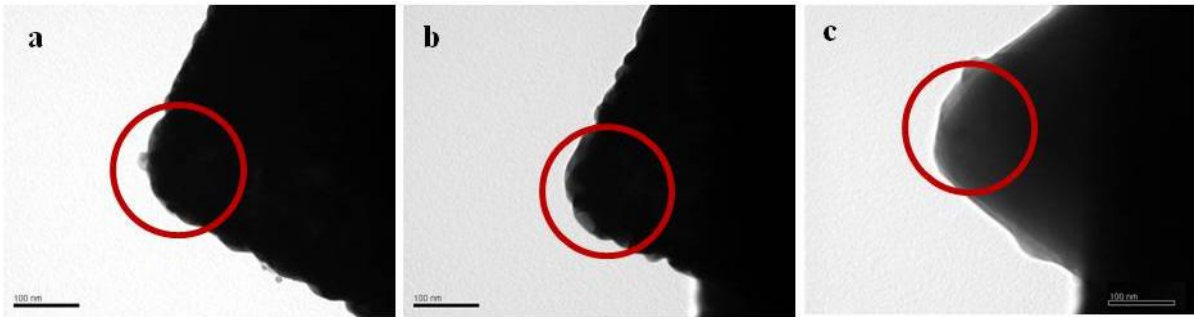

Figure 20. TEM images of three different *unprotected* metallized tips after a) zero scans, b) three scans, and c) six scans on a standard silicon grid. An increase in tip diameter from a) 45 (±5) nm to c) 65 (± 7) nm and a smoothing of the tip surface were observed after 6 scans. The tip apex is circled in each image. The scale bar is 100 nm in all images.

The increase in tip diameter was evidenced indirectly in the AFM images as a steady loss of resolution while imaging. Representative AFM images are presented in 3-D in Fig. 21 along

with line cuts from similar x positions. (The portion of the surface imaged was not exactly the same in each image due to thermal drift during continuous image collection.) The first image (Fig. 21a) collected showed crisp edges on the stripes and a smooth, level top for each stripe. The sixth image (Fig. 21b) showed rounded edges between the strips and significantly rougher tops for each stripe, indicating that the tip is producing artifacts during image collection. Artifacts are also observed in the image of the substrate surface between the stripes. We conjecture that some of these artifacts are due to the loss of optimal tuning of the feedback control parameters during continuous imaging. Once imaging was started, the feedback controls were not changed to ensure consistency among the different tips. This did not allow for "optimal" imaging conditions for the scans coming later in the series are resulted in less precise tip tracking of the sample surface over time. Some of the artifacts may also be due to pieces of the plasmonic structure breaking off of the tip and being deposited onto the surface of the grid. Representative AFM images collected with a protected metallized tip are presented in 3-D in Fig. 22 along with line cuts from similar x positions. Only a small change in resolution is observed and large artifacts are not present in the image.

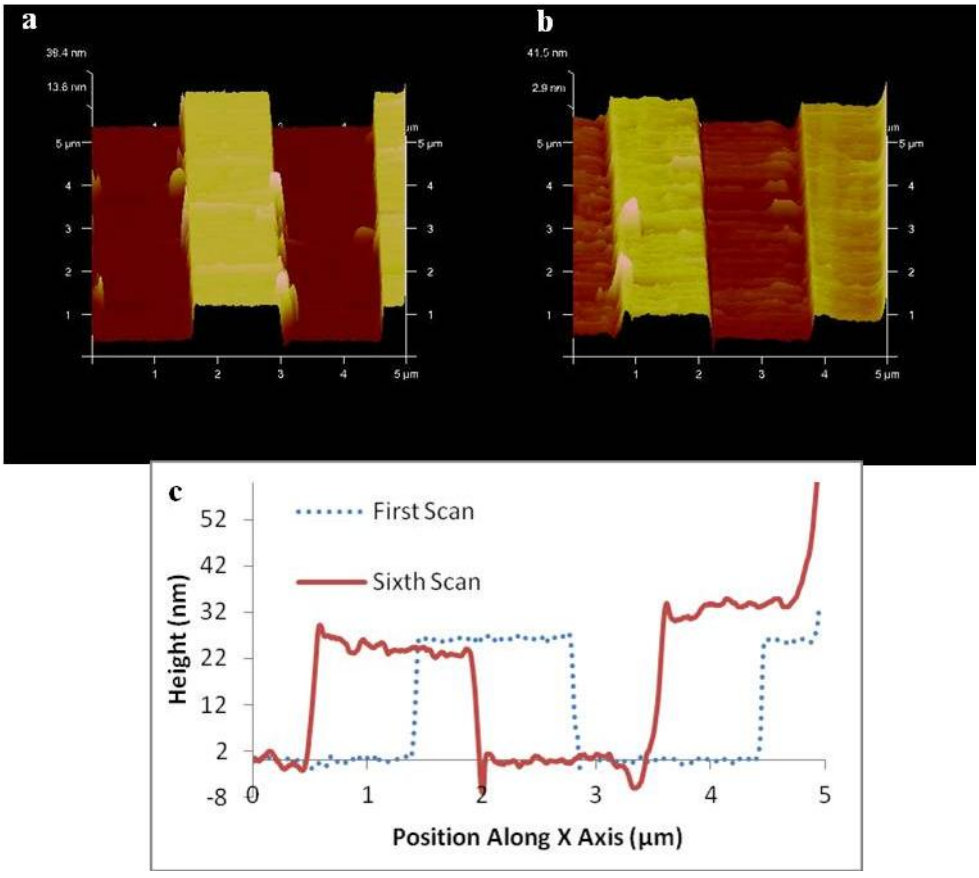

Figure 21. AFM 5 µm x 5 µm images showing the change in imaging resolution between (a) the first image scanned and (b) the sixth image scanned using an unprotected metallized tip. Full scale on the z-axis is 40 nm. (c) Representative line cuts.

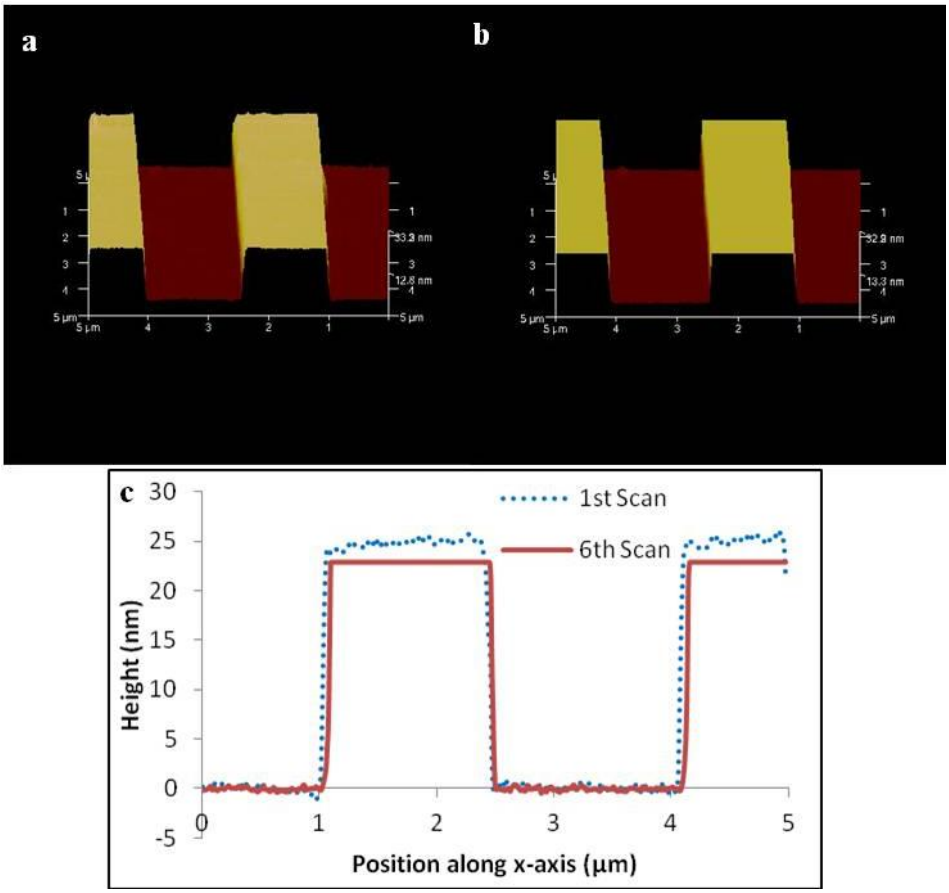

Figure 22. AFM 5 µm x 5 µm images showing the change in imaging resolution between (a) the first image scanned and (b) the sixth image scanned using a protected metallized tip. Full scale on the z-axis is 40 nm. (c) Representative line cuts. Only a small change in resolution is observed.

Representative TEM images of the protected silver metallized tips after collection of 0, 3, and 6 images are shown in Fig. 23. The aluminum oxide coating is observed as a bright region surrounding the tip and is most prominent in Fig. 23c due to the darker background in that case. No significant damage was observed on the protected tips, even after the maximum scanning performed. The tip diameter changed little, remaining in the neighborhood of 55 (± 3) nm with no appreciable change in roughness.

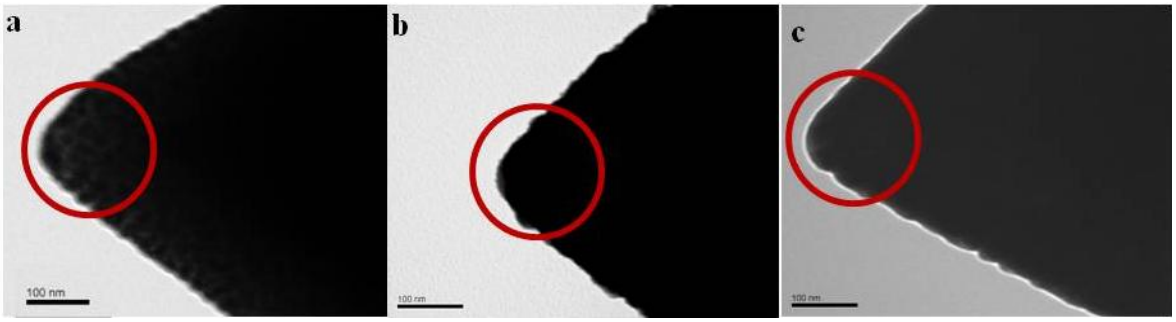

Figure 23. TEM images of three *protected* tips after (a) zero scans, (b) three scans, and (c) six scans on a standard silicon grid. No significant damage, increase in tip diameter, or loss of surface roughness was observed even after six scans. The tip apex is circled in each image. The scale bar is 100 nm in all cases.

Specific details of the type of damage that occurred on the tips during imaging were obtained using SEM images. The tips selected for imaging were those that appeared in TEM images to have been damaged the least. The view from straight above the apex allowed for a very clear comparison between the metallized and protected metallized tips. Examples of this comparison are shown in Fig. 24. The unprotected metallized tips exhibited extensive damage. In one case (Fig. 24a), the apex of the tip was substantially blunted and the silver plasmonic structure had been substantially removed from the faces and edges of the tip. In another case, the plasmonic structure was still present on the faces and edges of the tip; however, the tip apex had been detrimentally blunted and had a diameter of 225 (± 16) nm after imaging (Fig. 24b). Silver had also been removed up to a distance of 350 (± 70) nm from the tip apex. The large uncertainty is given because the damaged region is not symmetric about the center of the apex. The protected metallized tips (Fig. 24c,d) did not exhibit any substantial scan induced damage. The plasmonic structures were still present at and around the tip apexes and the tip diameters had not increased significantly compared to the initial tip diameter.

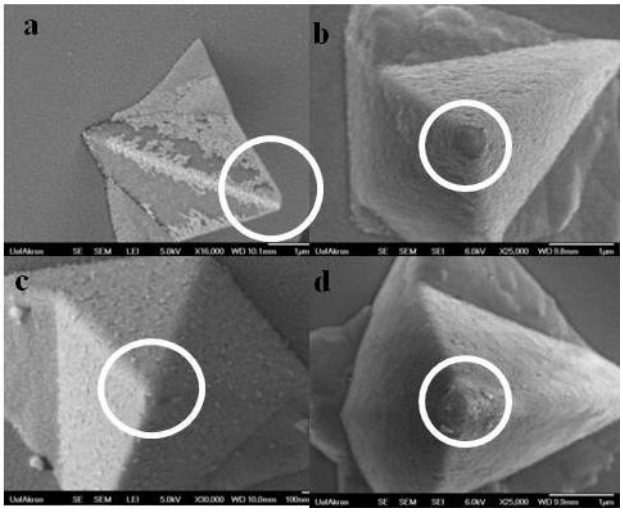

Figure 24. SEM images of (a,b) two unprotected silver metallized tips and (c,d) two protected metallized tips after six scans on a standard silicon grid. In all cases, the apex is circled. The magnifications vary slightly from image to image.

The improvement of the metallized probe performance with an aluminum oxide coating can be explained in the following way. The aluminum oxide provides a harder scanning surface than does the silver. The oxide (Vickers hardness of 2600 MPa[16]) is not easily damaged by either the approach to or scanning of the hard patterned silicon substrate. In addition to increased hardness, good adhesion between the oxide and the metal is also required for the aluminum oxide to stay intact during scanning. The aluminum oxide is initially deposited as aluminum. Therefore, the initial interface between the plasmonic structure and the overlayer was a metal/metal (Ag/Al) interface rather than a metal/oxide (Ag/Al_2O_3) interface. We conjecture that this leads to a stronger interface than one would be able to achieve if the aluminum oxide were directly deposited onto the silver[18]. In any case, the adhesion between silver and the protective coating achieved is sufficient for the protective layer to stay attached to the underlying metal even under mechanical stress. Internal stress leading to cracks and localized fracture is sometimes a concern for thin ceramic and metal films[19-21]. However, we did not observe cracks, localized fracture, or loss of any large pieces of the protective coating.

Goal 5: Extend TERS to aqueous environments:

This goal was to "demonstrate how such coatings can improve plasmonic structure robustness in aqueous environments." Protective coatings were deposited on metal films on flat substrates in exactly the same manner as that used for the deposition on plasmonic structures on tips. AFM images of the metal film without protection and with a protective coating were analyzed to provide direct, laterally resolved information on the local surface roughness of the coating and its relationship to the roughness of the underlying metal structure. This is essential information because SERS and TERS-based techniques are built around local properties.

Aluminum oxide and silicon oxide coatings

The studies with flat and rough films have been performed for both SiO_x and Al_2O_3 protective coatings, images of which are shown in Fig. 25. The silver film was 50 nm thick. The

protective coatings of alumina or SiO_x were 2.5 nm thick on top of a 50 nm silver film. The silver film had an RMS roughness of 2.0 (± 0.2) nm, while the alumina protected film had a roughness of 1.6 (± 0.3) nm and the SiO_x protected film had a roughness of 1.5 (± 0.3) nm.

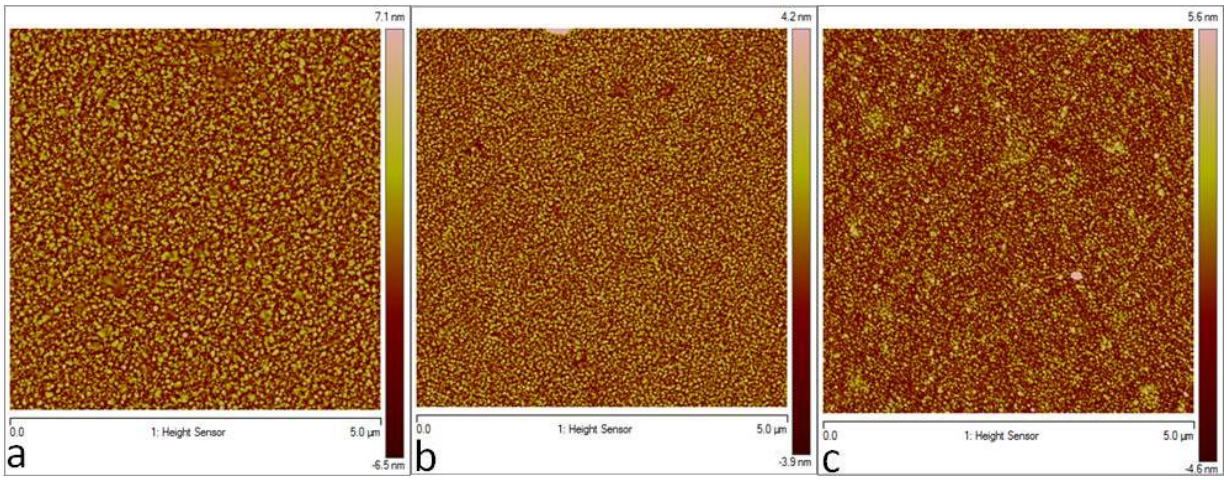

Figure 25. Tapping mode images showing the morphologies of an unsoaked: a) silver film, b) alumina protected silver film, c) SiO_x protected silver film. Full scale in the z-direction is 10 nm in all cases.

The morphologies of various plasmonic structures, with and without protective layers, were also imaged after exposure to aqueous environments for a specific amount of time. The aqueous environments chosen were ultrapure water, a 5 wt% sodium chloride solution, and Dulbecco's Modified Eagle Medium, which is a phosphate buffer solution commonly used for cell growth. These specific conditions were chosen to simulate the scanning environments that the plasmonic structures will need to withstand to enable the *in-situ* study of corrosion as well as high-resolution mapping of biological entities. The morphologies of silver films after two hours of an aqueous soak are shown in Fig. 26a-c. The same aqueous soak was performed on alumina protected and SiO_x protected silver films. Images of the alumina protected films after soaking are shown in Fig. 26d-f, and of the SiO_x protected films in Fig. 26g-i. The morphology of the alumina protected films did not undergo any observable change when exposed to ultrapure water; however pit formation as well as corrosion products are observable in the more corrosive soak environments. The SiO_x protected silver films exhibited a peak and valley morphology in all soak conditions that is indicative of the start of pit formation. The difference in height from the bottom of the valley to the top of the peak increases with soak solution type in the following order: ultrapure water, phosphate buffer solution, sodium chloride solution. The SiO_x coating provided the most protection from ultrapure water and the least effective protection from sodium chloride solutions. However, in all cases the SiO_x provided less protection than Al_2O_3.

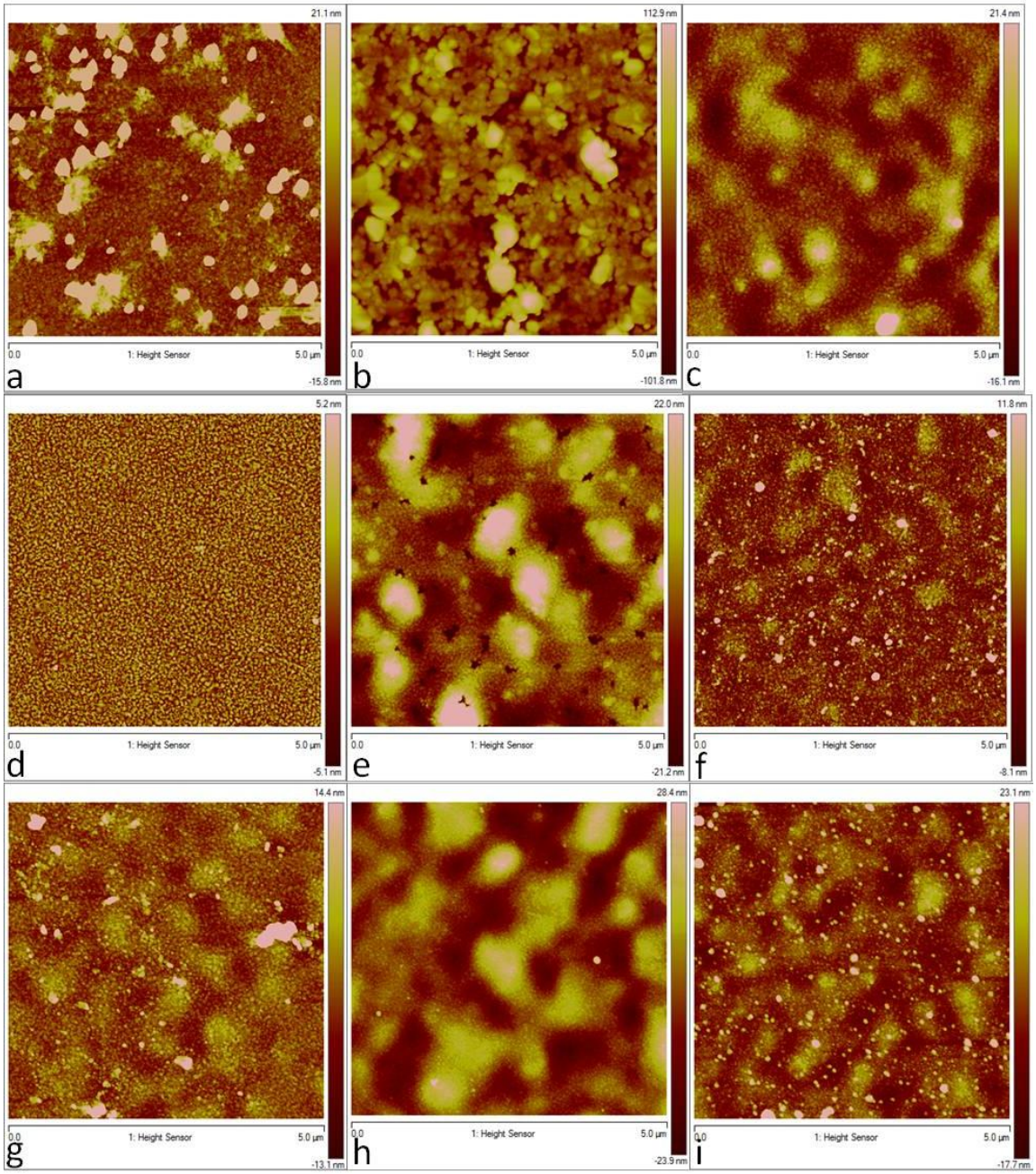

Figure 26. Tapping mode AFM images showing the morphology of metal films after a 2 h exposure to an aqueous solution. (a-c) Silver films after exposure to ultrapure water, a 5 % sodium chloride solution, and a phosphate buffer solution, respectively. (d-f) Aluminum oxide protected silver films after exposure to ultrapure water, a 5 % sodium chloride solution, and a phosphate buffer solution, respectively. (g-i) SiO_x protected silver film after exposure to ultrapure water, a 5 % sodium chloride solution, and a phosphate buffer solution, respectively. The z-scale in each image varies and was set so that the prominent features of each image were apparent.

Extensive delamination of the silver films, both unprotected and protected, from the substrate are observed for samples exposed to either the sodium chloride solution or the phosphate buffer solution. To address the delamination of the films under various soak conditions, a layer of chromium (Cr) was added between the substrate and silver layer. This additional layer was intended to act as an adhesion layer, increasing the bond strength between the native silicon oxide and the metal. A schematic diagram of the sample is shown in Fig. 27.

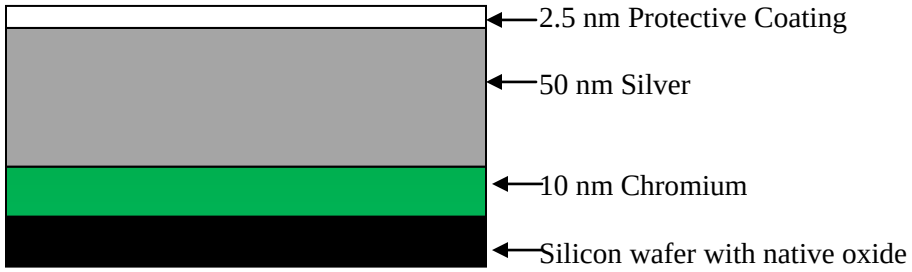

Figure 27. Schematic diagram of sample containing chromium adhesive layer.

The morphologies of an unprotected silver film and protected silver films, all atop Cr adhesion layers, before exposure to an aqueous soak are shown in Fig. 28. The morphologies of these same films after a two hour soak in various solutions as described above are shown in Fig. 29.

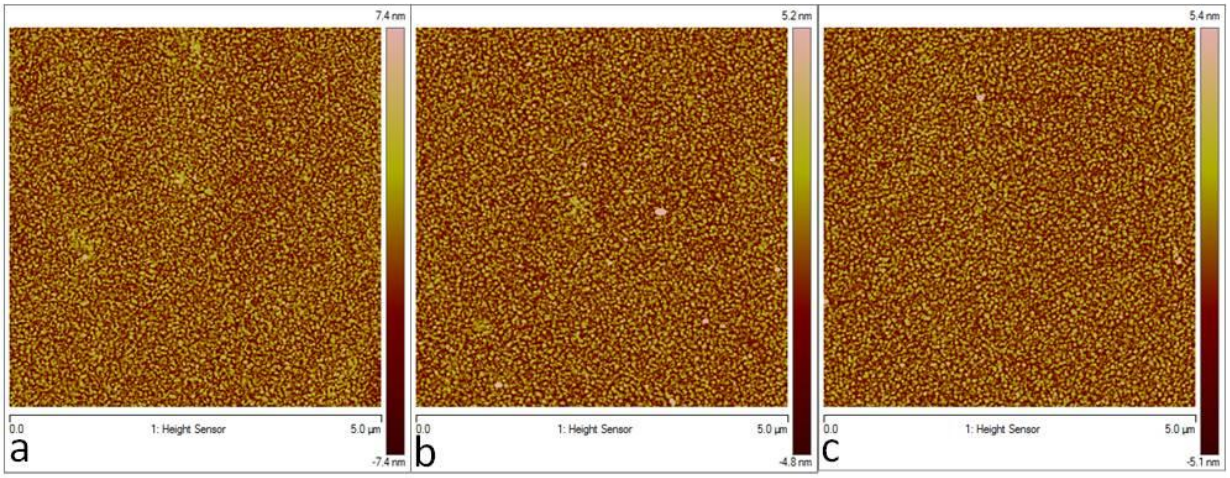

Figure 28. Tapping modes images showing the morphologies of three unsoaked films made using 10 nm thick Cr adhesive layers: a) unprotected 50 nm silver film, b) alumina protected silver film, and c) SiO_x protected silver film. Full scale in the z-direction is 10 nm in all cases.

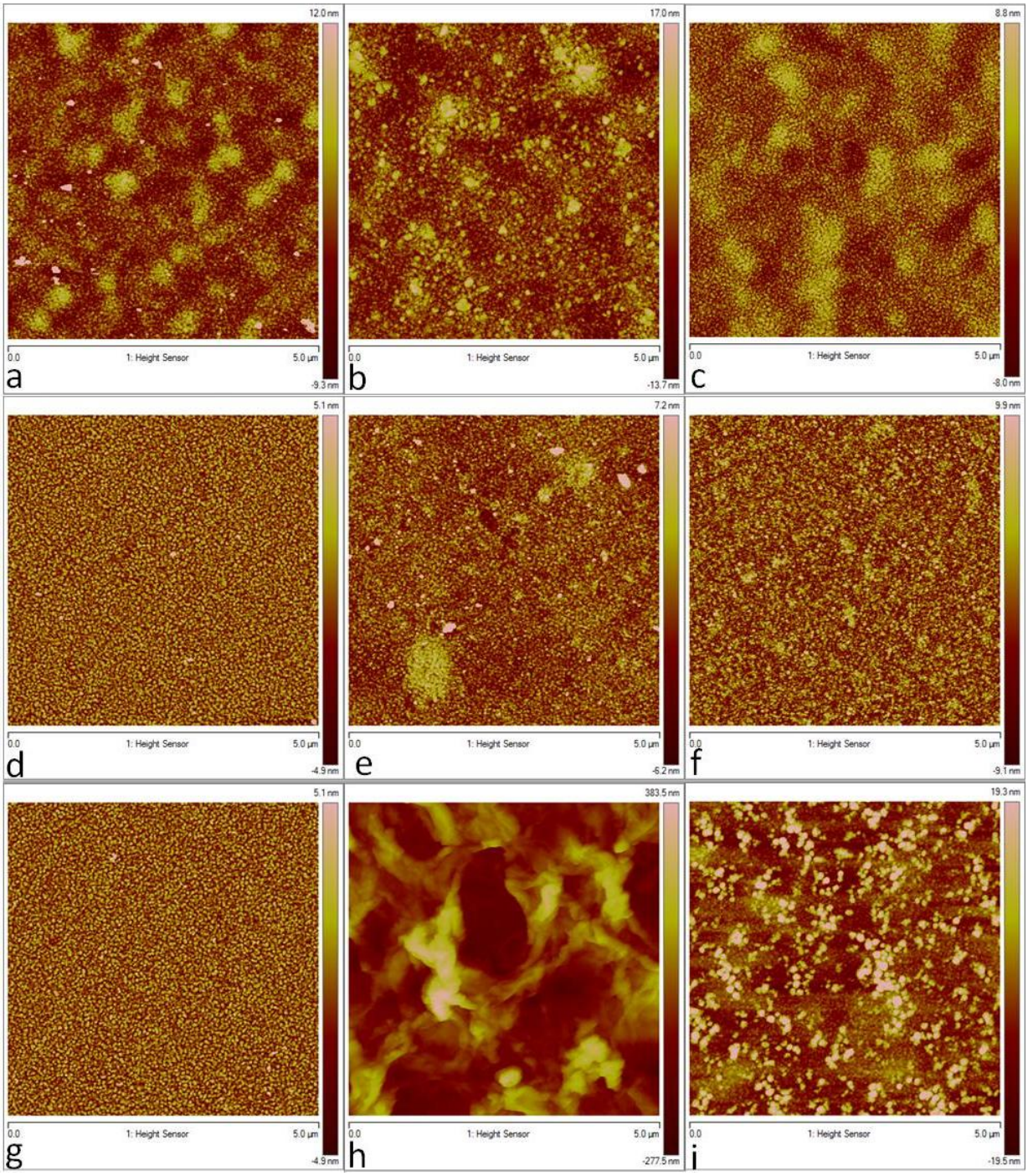

Figure 29. Tapping mode AFM images showing the morphology of metal films with a Cr adhesive layer after a 2 h exposure to an aqueous solution. (a-c) Silver films after exposure to ultrapure water, a 5 % sodium chloride solution, and a phosphate buffer solution, respectively. (d-f) Aluminum oxide protected silver films after exposure to ultrapure water, a 5 % sodium chloride solution, and a phosphate buffer solution, respectively. (g-i) SiO_x protected silver film after exposure to ultrapure water, a 5 % sodium chloride solution, and a phosphate buffer solution, respectively. The z-scale in each image varies and was set so that the prominent features of each image were apparent.

The morphology of the silver film has changed after all three soak conditions. The height of the surface now varies substantially across each image. We conjecture that the low points may correspond to pits. If so, the start of pit formation is observable in the case of all three soak conditions. The sodium chloride soak also results in the formation of a corrosion product observable on top of the pits. No significant delamination was observed for any of the soak conditions for the samples containing a Cr underlayer. The alumina coating preserved the morphology of the film when exposed to ultrapure water. The morphologies of the alumina protected films exposed to sodium chloride and phosphate buffer (Fig. 29e,f) solution soaks were also significantly improved compared to those of the film analogs without a chromium adhesive layer (Fig. 26e,f). No significant delamination was observed on any of the alumina protected silver films with the chromium adhesion layer.

The SiO_x protective layer preserved the film morphology when exposed to ultrapure water soak conditions. The SiO_x did not provide protection against sodium chloride or phosphate buffer solution soaks, as was evident by significant morphology changes (Fig. 29h,i). The sodium chloride solution damaged the metal film enough to cause a color change from reflective silver to a dull gray observable by the naked eye. The phosphate buffer solution caused a change in the morphology of the protected film that nearly matches that of the unprotected silver film. The protected film also showed evidence of a corrosion product resulting in the large features observable on top of a smaller scale underlying morphology.

A summary of the RMS surface roughnesses is presented in Table 3. The alumina protected silver film with a chromium adhesion layer exhibited the most consistent surface roughness after soaking for all of the soak conditions investigated. This is consistent with the AFM images showing the smallest amount of change in the film morphology for this sample set, indicating that the alumina is an effective protective coating that may help to extend the TERS technique to aqueous environments.

Table 3. RMS surface roughness (nm) of 50 nm thick silver films after two hour aqueous soak.[a,b]

	No Soak	DI water soak	5% NaCl solution soak	Phosphate Buffer solution soak
Ag	2.0 (± 0.2)	32 (± 3)	35 (± 4)	17 (± 2)
Ag/ Alumina	1.6 (± 0.3)	1.6 (± 0.2)	8.2 (± 0.5)	11 (± 1)
Ag/ SiO_x	1.5 (± 0.3)	3.8 (± 0.4)	8.4 (± 0.5)	6 (± 2)
Cr/ Ag	2.2 (± 0.4)	3.9 (± 0.4)	4.2 (± 0.3)	2.6 (± 0.3)
Cr/ Ag / Alumina	1.5 (± 0.3)	1.5 (± 0.2)	2.9 (± 0.3)	2.3 (± 0.3)
Cr / Ag / SiO_x	1.6 (± 0.2)	1.5 (± 0.3)	94.6 (± 10)	8 (± 1)

[a] The protective coating is 2.5 nm thick when present.
[b] The layers are labeled (left to right) starting with the film closest to the silicon substrate.

Although the Cr adhesive layer improved adhesion between the silver layer and the silicon substrate preventing delamination, it still may not be a realistic solution for TERS measurements. Additional layers in the plasmonic structure may shift the plasmon resonance, leading to lower enhancements at the wavelength used in the experiment. Since the optical properties measured with tips have large variability depending on the exact orientation of the probe with the substrate used in the measurement, the optical properties with the Cr adhesive layer were measured from a flat glass substrate. The optical properties of a silver film with a Cr adhesive layer are compared to that of a pure silver film in Fig. 30. The resonance frequency for the silver film with an

underlying Cr adhesive layer has red-shifted 10 nm from that of the silver film without an adhesive layer. This shift in resonance frequency will lower the enhancement at the incident wavelength of 514 nm used in our TERS measurements.

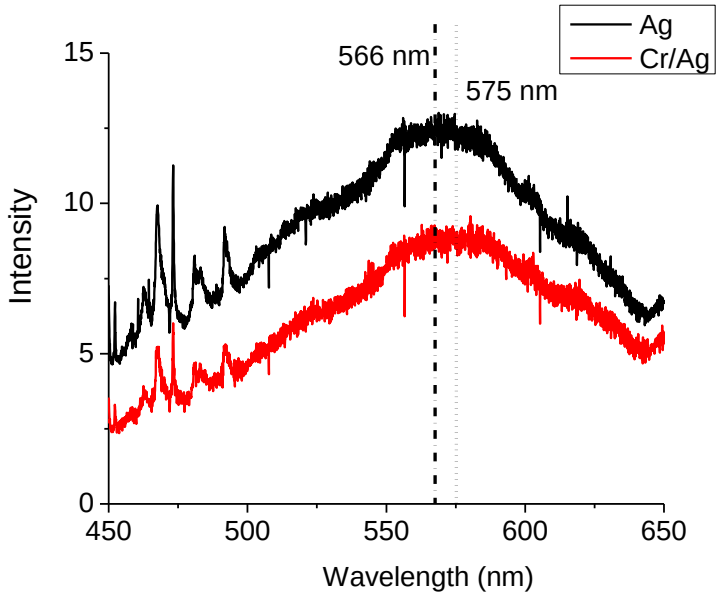

Figure 30. Optical spectra of a silver film (black) and a silver film with a Cr adhesive layer between the metal and the silicon substrate (red). The resonance frequency of the film with a Cr adhesive layer has red-shifted 10 nm from that of the metal film without an adhesive layer. This shift in resonance frequency will lower the enhancement at the incident wavelength of 514 nm used in our TERS measurements.

Diamond-like Carbon Coatings

There is another large family of coatings made from carbon that hold great promise for protecting plasmonic structures from degradation. Diamond-like carbon (DLC) coatings firmly adhere to silicon and metal substrates, are smooth and compact, and are ideal self-lubricating and protective layers because of their antifriction and wear-resistance characteristics[22-24]. These coatings were therefore investigated, specifically in aqueous environments, with the objective of circumventing the limitations observed with aluminum oxide coatings.

AFM images of the DLC coatings on flat silicon wafers are presented in Fig. 31 and of the DLC coatings on silver films in Fig. 32. (Several images are presented corresponding to the different fabrication parameters. The flow rates of acetylene and argon gases were modified to control the composition of the gas surrounding the sample during deposition.) The DLC films on flat silicon substrates were expected to be flat and pinhole free. However, AFM images of the DLC coatings on silicon substrates revealed that the DLC films contained pinholes ranging from 0.5 to 4 nm deep. The films also were not perfectly flat. Slight variations in film thickness were observed as relatively higher and lower regions in the topography maps.

The DLC coatings on silver films do not appear to conformally follow the underlying silver morphology. The coated films have large features present on top of the characteristic silver morphology (see Fig. 25a for pure silver film morphology). The RMS roughnesses of the silver films, summarized in Table 4, increased after the deposition of the DLC coating. This increase

in roughness could be due to the etching procedure at the beginning of the deposition damaging the silver surface. It could also be due to a non-uniform DLC coating on top of the silver.

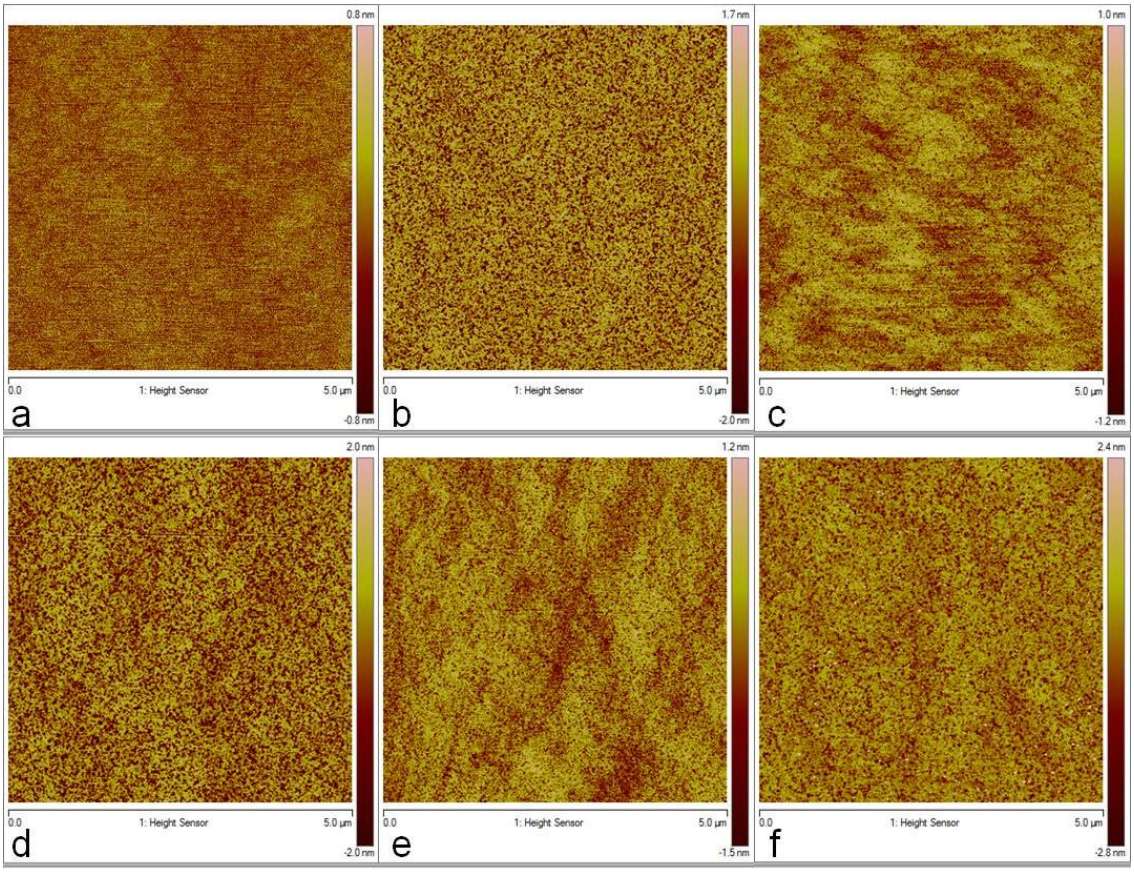

Figure 31. AFM images of DLC films on a flat silicon substrate prepared with different ratios of flow rates, Ar / C_2H_2, during the deposition. The gas flow rates were: a) 0 / 80, b) 16 / 64, c) 32 / 48, d) 40 / 40, e) 48 / 32, and f) 64 / 16 sccm Ar / sccm C_2H_2, respectively. Full height in the z-direction is 2 – 4 nm depending on the image.

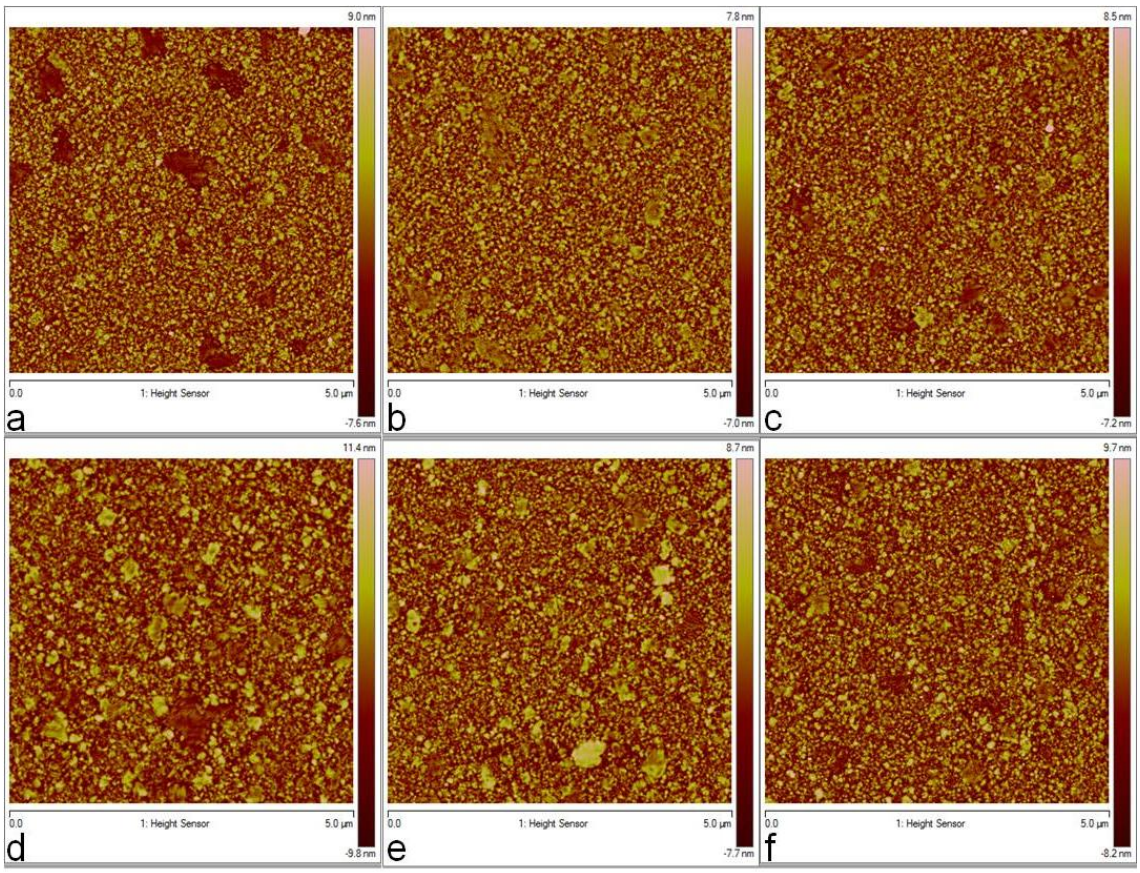

Figure 32. AFM images of DLC protected silver films prepared with different gas flow ratios of Ar / C_2H_2 during the deposition. The gas flow rates were: a) 0 / 80, b) 16 / 64, c) 32 / 48, d) 40 / 40, e) 48 / 32, and f) 64 / 16 sccm Ar / sccm C_2H_2, respectively. Full height in the z-direction is ~ 15 nm.

Table 4. Surface roughnesses of films containing DLC coatings in air[a]

Ar (sccm)	C_2H_2 (sccm)	Thickness from TEM (nm)	RMS roughness on top of a silver film (nm)	RMS Roughness of coating on a flat silicon substrate (nm)
0	80	3.6	2.5 (± .3)	0.23 (± 0.1)
16	64	3.6	2.3 (± .2)	0.74 (± 0.1)
32	48	8.6	2.5 (± .3)	0.31 (± 0.1)
40	40	7.1	2.9 (± .3)	0.75 (± 0.1)
48	32	8.8	2.4 (± .2)	0.38 (± 0.1)
64	16	8.2	2.5 (± .3)	0.67 (± 0.1)

[a]For reference, a pure silver film has an RMS roughness of 2.0 (± 0.2) nm and a silicon wafer has a RMS roughness of 0.08 (± 0.02) nm.

In contrast to the non-conformal, pinhole containing films that were prepared on flat substrates, the DLC coatings applied to metallized probes appeared significantly better. Representative TEM and SEM images of a DLC protected silver metallized probe are shown in Fig. 33. The DLC coating appears to nearly conformally follow the underlying silver morphology on the tip. The morphology of the silver coatings underneath DLC films differed slightly on a local scale from that of silver layers without the DLC covering, most likely as a result of the argon etching performed before deposition of the DLC film. This change in morphology can be observed in Fig. 33b as gradients in electron density near the silver/ DLC film interface. Such a gradient across the interface is not observed in Al_2O_3 protected films. No pinholes were observed in the DLC coatings on a metallized probe. We speculate that the addition of the silver interlayer between the silicon nitride probe and the DLC coating helped to dissipate any residual stresses resulting from film formation[25]. The relief of this stress through the silver layer prevented pinhole formation in the DLC film on probes.

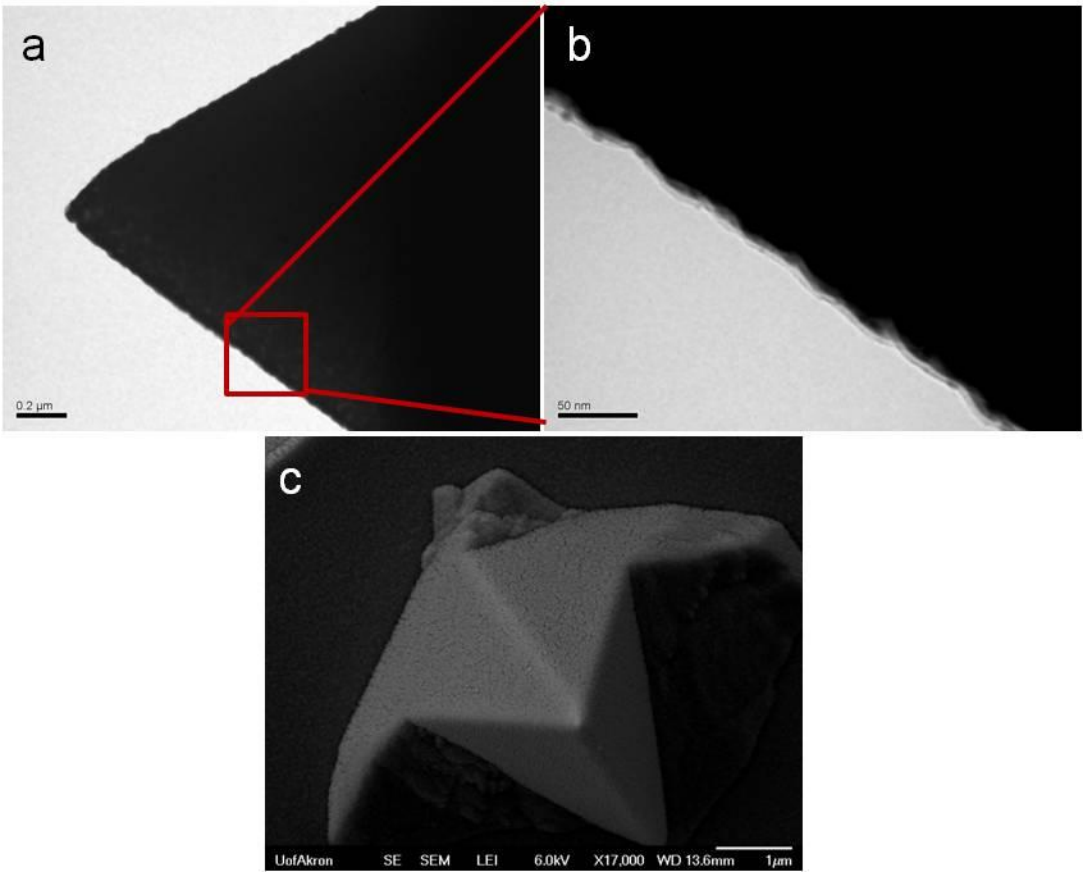

Figure 33. Representative TEM images of a DLC coated silver metallized probe at a a) low magnification and b) higher magnification. c) SEM image taken looking directly down the tip apex of a DLC coated silver metallized probe. The DLC coating appears to conformally follow the underlying silver morphology without the formation of pinholes.

The stability of the DLC coated silver films when exposed to aqueous environments was investigated next. These tests were performed on DLC coated silver films on flat substrates. After a 20 min exposure to the sodium chloride solution, total delamination of the DLC protected

films was observed. (This delamination occurred faster for the DLC protected films than for the alumina or SiO_x protected films.) No AFM data were collected for these samples because the metal film was no longer attached to the silicon substrate. AFM images of representative DLC coated silver films after exposure to water and PBS are shown in Fig. 34. An increase in aggregation was observed that led to an increase in RMS surface roughness. The roughness increased from 2.9 (± .3) nm for an unsoaked film to 4.9 (± 1) nm and 5.6 (± 0.5) nm for the films exposed to ultrapure water and PBS, respectively. These increases in aggregation indicated that the DLC coating was unable to prevent morphological changes upon exposure to aqueous environments, and is therefore an ineffective protective coating for extending TERS to aqueous environments.

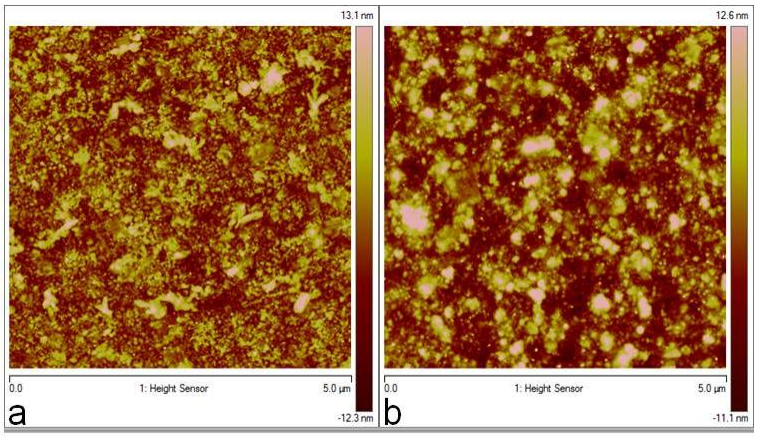

Figure 34. AFM images of a DLC coating on a silver film prepared with gas flow rates of 40 sccm Ar / 40 sccm C_2H_2 after a 2 h soak in a) ultrapure water, and b) phosphate buffer solution. An increase in aggregation is observed after exposure to aqueous environments.

Goal 6: Define how addition of a coating changes (if at all) the spatial distribution of enhancement in plasmonic structures

Subgoal 6a: Gain understanding of the geometry of hot spot in plasmonic structures

Several groups[26-29] have reported detection of a few molecules or a single molecule after incubating a colloidal solution of silver particles with a very low concentration of dye molecules, such that the average concentration is one dye molecule adsorbed per particle. Detection of one or a few molecules with TERS has also been reported[30-33]. Spectra acquired from these SERS and TERS samples were characterized by two unusual features. First, the spectra appeared intermittently. Secondly, the spectral position of at least one peak fluctuated and the relative intensities of various peaks fluctuated with time. Such behavior has been termed "blinking". The reported duration of blinking was on the order of minutes. Similar intensity fluctuations have been observed in fluorescence spectroscopy[34] and attributed to single molecule detection.

Work has been done to identify the structures that provide the very large enhancement needed to make high resolution imaging and extremely sensitive detection practical. There is ample evidence in the literature[28, 29, 35-38] that clusters of particles, rather than individual particles,

provide extremely high enhancements. Nevertheless, we have analyzed whether either faceted particles or high aspect ratio particles can form highly enhancing plasmonic structures.

Collections of particles including nanorods have been synthesized according to a well-known seed-mediated procedure[39], which has recently been significantly improved by Wu *et al.*[40]. An aqueous solution containing $2.5x10^{-4}$ M $HAuCl_4$ was stabilized by trisodium citrate solution of low concentration. The seeds were prepared by fast reduction of this solution by $NaBH_4$ in ice-cold trisodium citrate. To increase the aspect ratio of the particles, a growth solution was made by dissolving a large amount (0.01 mol) of CTAB surfactant in 100 mL of $2.5x10^{-4}$ M $HAuCl_4$ aqueous solution. In two flasks, labeled "A" and "B", 25 μL of 0.1 M ascorbic acid was added to 4.5 mL of growth solution. In flask "C", 250 μL of 0.1 M ascorbic acid and 200 μL of nitric acid were added to 45 mL of growth solution. Next, 400 μL of the gold seed solution was added to the solution in flask A and stirred slightly for 3 s. Then 400 μL of the solution in flask A was added to flask B and stirred for 3 s. Finally, 4 mL of the solution in flask B was transferred to flask C and stirred for 3 s. Flask C was left undisturbed for 12 h for the reaction to go to completion. The solutions were characterized by means of TEM and optical absorption.

A typical assortment of particles from such a purified solution is shown in Fig. 35 along with spectra demonstrating the enhancement achieved using a polymer blend poly(3,4-ethylenedioxythiophene)/poly(styrenesulfonate) (PEDOT/PSS) (Baytron® P from H.C. Starck) as a standard. The particles formed include fairly well-defined rods with a narrow distribution in diameter (~20 nm) and hundreds of nanometers in length, which therefore have aspect ratios above 20. In addition to rods, the solution contained a number of smaller particles of various shapes. According to TEM data from different batches of rods, the diameters of ~90% of the rods are very close to 20 nm. The size distribution is Gaussian.

According to literature reports, the transverse plasmon band of such a rod is expected to be observed around 530 nm[41]. With increasing aspect ratio, the transverse resonance shows a small shift to shorter wavelengths[42]. Our optical absorption measurements from a solution of particles show a peak at 530 nm (Fig. 36). The peak at 630 nm corresponds to absorption of small particles that have more spherical shapes. The shoulder of a broader peak above 800 nm corresponds to the longitudinal band of the long rods. Simulations have shown that the scattering spectra red-shift slightly when two gold rods are interacting[43, 44]. Experimental results show similar trends[43, 44]. The simulation studies have also revealed minor red shifting of the band with decrease in rod separation. These three factors together would result in the position of the transverse band in the range of 520-560 nm. This corresponds to the left shoulder of the optical absorption peak for the particles deposited on a glass slide with a thin polystyrene coating (to simulate the substrate for SERS). The peak for dry particles is centered at ~610 nm and therefore corresponds mainly to aggregates of small particles.

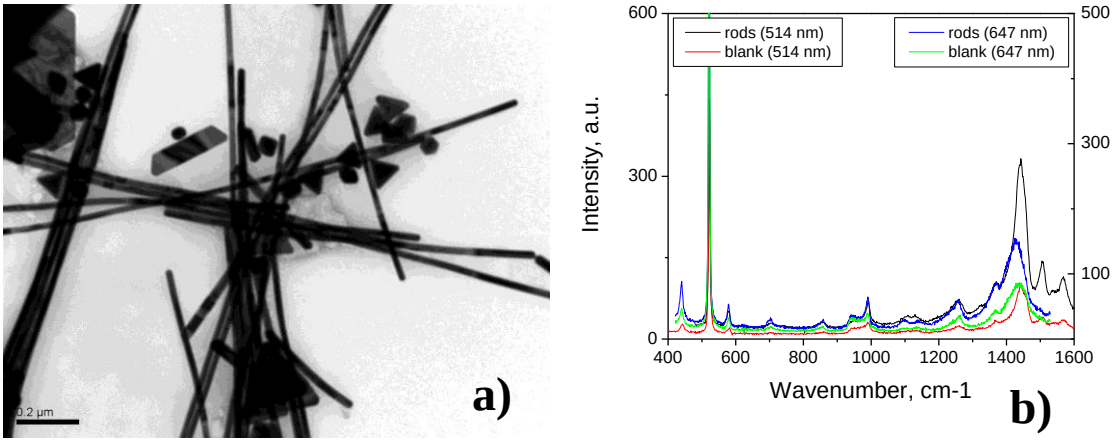

Figure 35. a) TEM image of gold particles obtained using the protocol described and b) comparison of the enhancements in the Raman spectrum from a sample of PEDOT/PSS in the presence of these particles with green (λ = 514.5 nm) and red (λ=647 nm) illumination. Enhancement is observed for both excitation wavelengths, 514.5 nm and 647 nm, although it is weaker in the latter case.

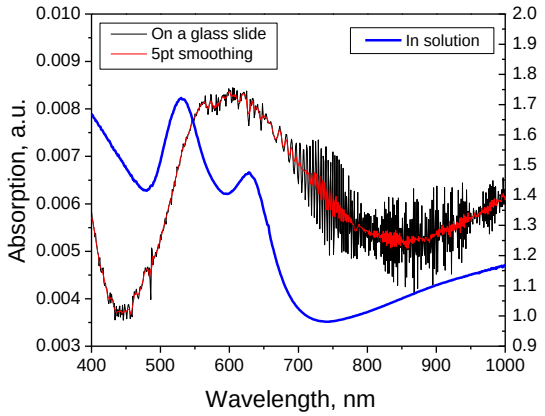

Figure 36. Optical absorption spectra of a particle solution (blue curve) and particles deposited on a glass slide with a polystyrene layer (black curve).

Sets of spectra for a sample of PEDOT/PSS, drop coated with the particle collections containing a predominance of nanorods are shown in Fig. 37. These spectra show a complex behavior, including blinking. This phenomenon is generally regarded as a signature of extreme enhancement. Large intensity fluctuations with some peaks completely disappearing and reappearing were observed as data were collected as a function of time. Some peak positions were also observed to fluctuate by tens of cm^{-1}. Broad backgrounds attributable to amorphous carbon were also generally seen to develop in the Raman spectra over time (but are not seen in the selected spectra shown here). This background is thought to result from polymer decomposition that occurs at the locally high sample temperatures induced by extreme

enhancement. This general behavior has been observed multiple times, but the spectra shown here show the largest enhancement seen so far for such samples.

Individual spectra correspond to a 1 s acquisition time with 0.5 s delay to the next acquisition. It is interesting to note that blinking appears intermittently. Strong blinking was observed during the first 40 s of illumination (Fig. 37a), and then no blinking was observed for the next 40 s, then intense blinking reappeared for 30 s (Fig. 37b), and then no blinking was observed for the next 70 s, and after that another set of blinking was observed for 15 s (Fig. 37c). Peak intensity and position fluctuations are clearly visible in all cases. The spectra generally do not look exactly like those of PEDOT or PSS, but positions of many peaks are characteristic of standard SERS spectra of these two molecules. The individual peaks have been assigned as follows[45]: PEDOT: oxyethylene ring deformation (800, 970 cm^{-1}), C-O-C deformation (1125 cm^{-1}), C-C interring stretch (1200 cm^{-1}), C=C symmetric (1520 cm^{-1}) and C=C asymmetric stretching (1580 cm^{-1}); PSS: C-S stretch (820, 817 cm^{-1}), sulfonic acid residue (1170, 1200 cm^{-1}), C-C interring stretch (1540 cm^{-1}).

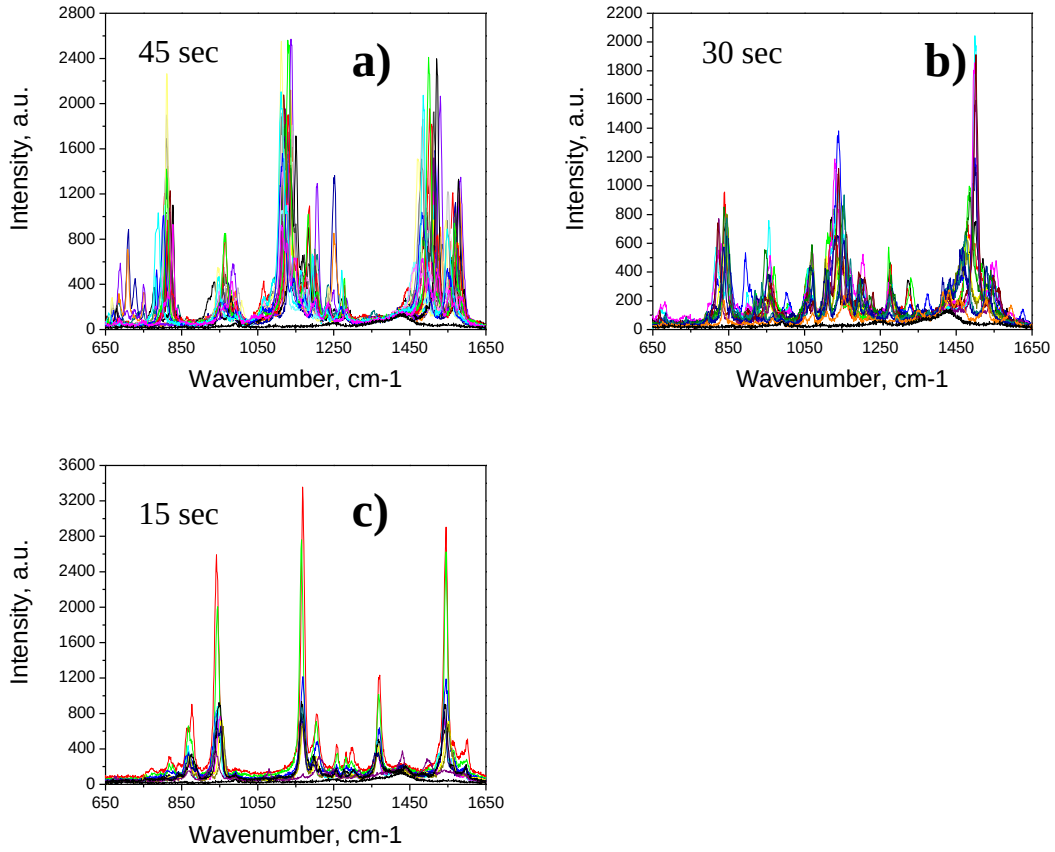

Figure 37. Three sequences of Raman blinking observed for a hot spot. Each spectrum corresponds to 1 s acquisition time with 0.5 s delay to the next acquisition. a) Spectra collected from the first 40 s of illumination. No blinking was observed for the next 40 seconds. b) Intense blinking that appeared for the next 30 s of the series. No blinking was observed for the next 70 seconds, and after that c) another set of blinking was observed for 15 seconds. The patterns in (a,b) contain several peaks assignable to PEDOT, while many peaks in (c) correspond to PSS.

Laterally resolved analysis of the Raman enhancement showed that blinking occurred only in a small percentage of the sample area. It seems that a particular arrangement of particles is necessary to form a hot spot and to produce blinking spectra. Such spots were located using the following approach. First, a fine razor scratch was made in the polymer film as a reference marker. The optical image of the illuminated area was recorded after each blinking spot was found (Fig. 38a). This picture was correlated to an optical image from an optical microscope with higher resolution and a better digital camera (Fig. 38b). Then this optical image was correlated to a low-magnification SEM image (Fig. 38c). When the area was identified, the close-up high magnification images of individual hot spots were recorded.

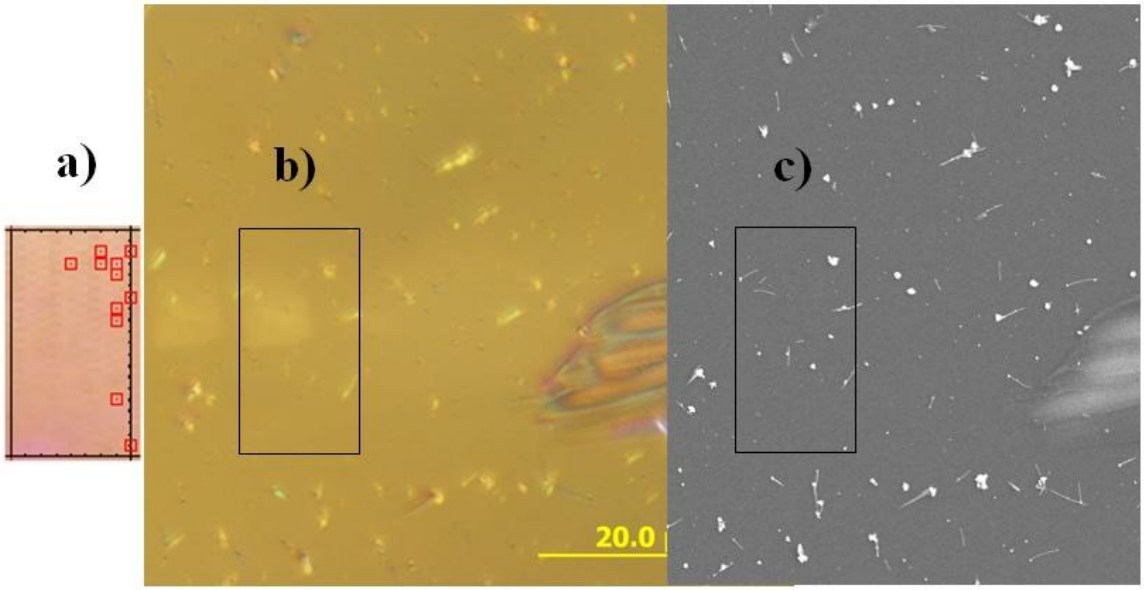

Figure 38. A representative set of images showing how the various images microscopy images were correlated: a) Raman microscope, b) SEM, and c) optical microscope images. Red squares represent areas were blinking was observed in Raman spectroscopy.

From SEM images, it was possible to identify the structures of some hot spots. Images of separate particles and aggregates that did not yield blinking spectra in Raman are presented in Fig. 39. Separate spheres, as well as single and parallel rods did not produce blinking. In fact, not even all clustered spherical particles produced blinking.

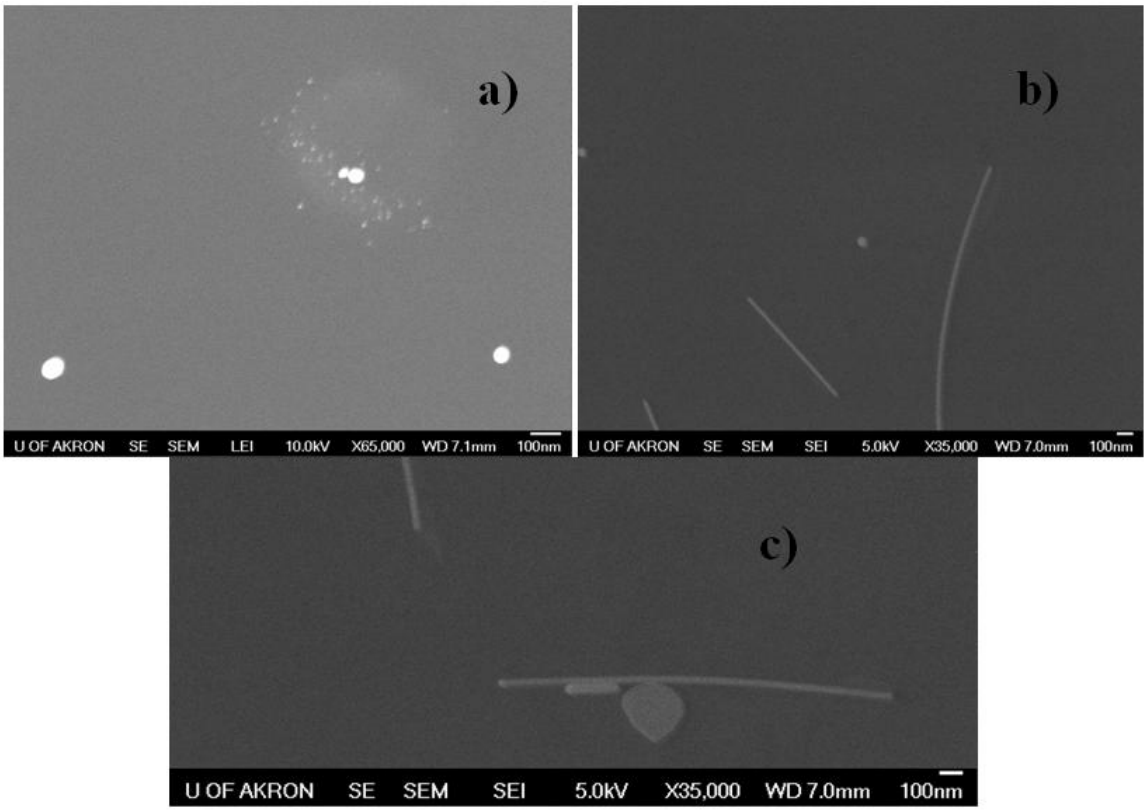

Figure 39. SEM images of a) single and adjacent spherical particles, b) separate rods, c) and interacting rods that did not produce blinking spectra. The polarization of the laser used in the data collection was from top to bottom of the images.

Blinking was observed in aggregates of small faceted particles of various shapes as illustrated in Fig. 40. Also, while individual spherical particles and rods were not observed in hot spots, their aggregates seem to produce them.

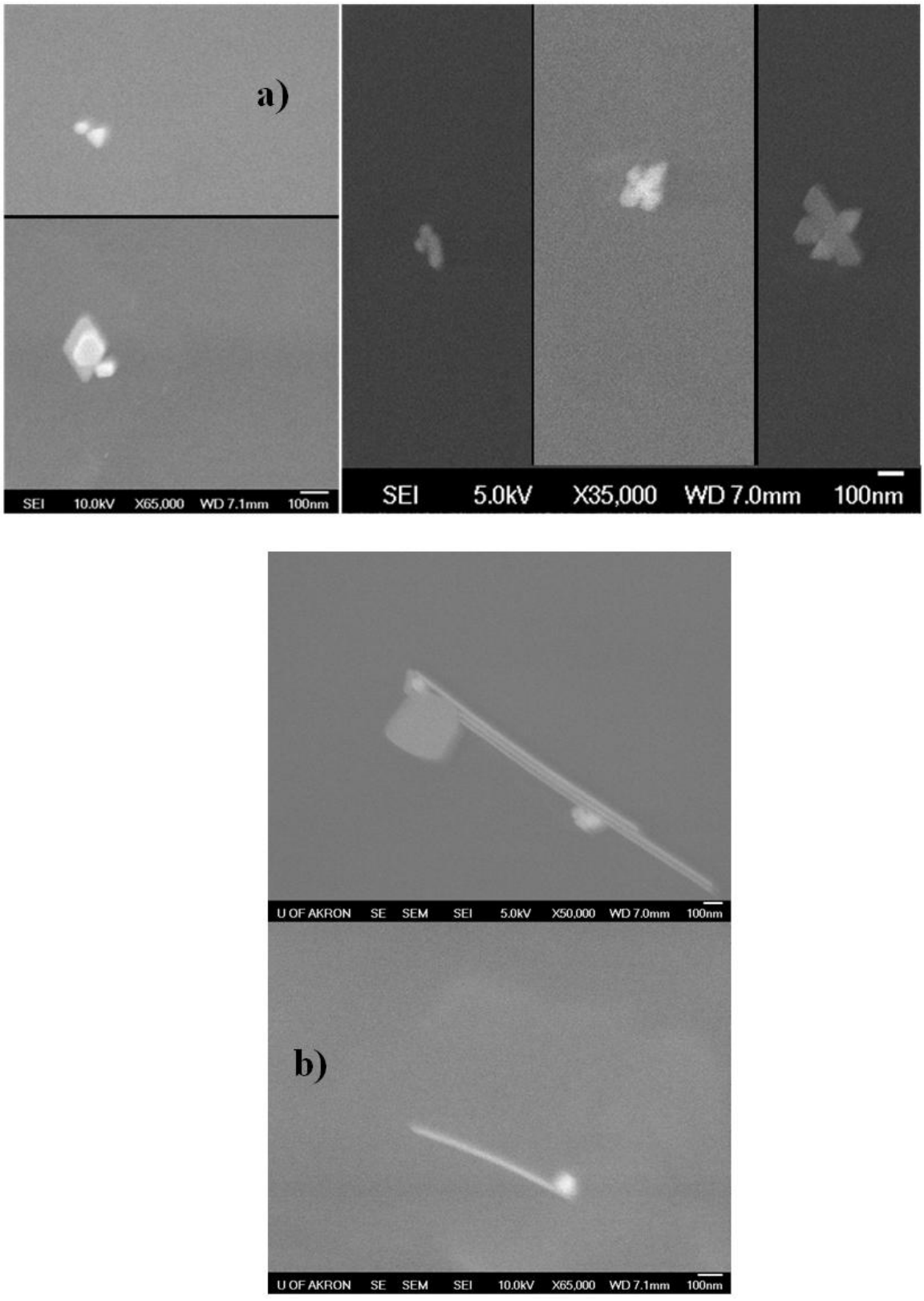

Figure 40. SEM images of aggregates producing blinking hot spots composed of a) multiple small faceted particles, and b) small particle(s) and a rod.

The analysis of various gold particles suggests that particle aggregates produce hot spots capable of extreme enhancement. The variations seen in the spectra measured from PEDOT/PSS samples suggest that portions of the polymer molecules are able to diffuse in and out of hot spots, but the involvement of adventitious hydrocarbon contaminant molecules cannot be excluded at this point. It appears that thermal decomposition of molecules or parts of molecules in the hot spots also may be induced in molecules resting in a hot spot for a long enough period of time.

Subgoal 6b: Define the role of "blinking" in the enhancement achieved with <u>coated</u> plasmonic structures[46].

Carefully controlled experiments with protected and unprotected TERS tips were performed to elucidate how coating a plasmonic structure may change the role of "blinking" in the enhancement. In the course of this study insight was gained into the mechanism by which the enhancement is achieved in the systems studied. In particular, it was shown that chemical enhancement cannot be the major mechanism of enhancement for these materials.

In these experiments, a 50 nm thick blend film of PEDOT/PSS was analyzed. In film form the blend has a T_g of about 65°C and is expected to soften so that the polymer molecules can diffuse when heated by the incident laser beam. Previous work[47] has shown that the temperature in the portion of the sample influenced by the plasmon enhanced field can be in excess of 100°C. Two hard samples, in which the diffusion of the constituents is extremely limited, even at 100°C, were also analyzed. The first hard sample was a cadmium sulfide (CdS) film prepared by plasma sputtering a 20 nm CdS film onto an aluminum mirror. CdS is a crystal with a melting temperature of 1750°C[48]. A silicon wafer (Umicore), a crystal with a melting temperature of 1414°C[48], cleaned in a 3:1 volume ratio mixture of boiling sulfuric acid:H_2O_2 for 5 minutes[49] was also analyzed. The laser power (λ = 514.2 nm) incident on the sample was held between 0.3 and 0.4 mW for all experiments.

Two successive batches, each with three silver metallized (non-protected) tips, were tested (for a total of 6 tips). Each tip was brought into contact with the surface of a PEDOT/PSS polymer blend. Data were acquired with 1 s acquisition time beginning at the time of the tip contacting the substrate (time = 0 s) and ending when the spectra no longer exhibited any fluctuations in peak intensities for a period of ~30 s. Selected spectra from a representative data set are shown in Fig. 41. After a 15-20 s induction period, strong changes in peak intensities as well as the appearance of new peaks were observed. This induction time varied from tip to tip. After a few "blinks" the spectrum might have a "normal" shape for several seconds before blinking again. This "switching" on and off of the blinking has been observed with SERS substrates as well[26-29] (see also our data above). There are two time scales associated with the blinking. The first time scale, which is on the order of seconds, is associated with fluctuations in relative peak intensities and peak positions (and may be limited by our acquisition time). The second time scale involved is the overall time during which blinking is observed. As the plasmonic structure degrades over time, the hot spot responsible for high enhancement may degrade or be eliminated by changes in the detailed shape of the rough plasmonic layer surface. Such changes lead to irreversible loss of blinking. In the case of unprotected tips, the duration of blinking was 8-21 min. After that time, not only had the blinking ceased, all useful enhancement was lost (i.e. the tip was no longer usable). Blinking was observed on 50% of the unprotected tips tested.

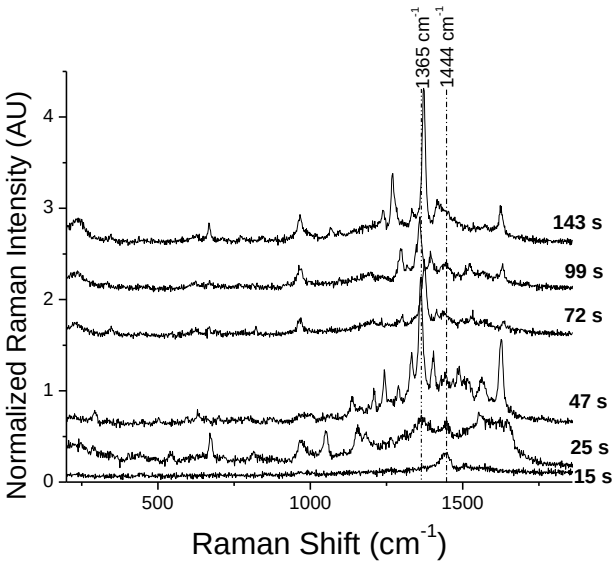

Figure 41. Selected Raman spectra of a PEDOT/PSS film obtained with an unprotected metallized tip. The time elapsed after contact with the sample surface is shown to the right of each spectrum. From initial contact (time = 0 s) until a time of ~15 s the spectra are all the same and are consistent with a typical SERS spectrum from the PEDOT/PSS blend[45]. However, the spectra at later times show strong fluctuations in intensity and positions of the Raman modes as well as with additional peaks not initially observable. All spectra have been offset for clarity.

Successive batches of three tips with protective coatings (6 tips total) were also used to collect spectra from the PEDOT/PSS film (Fig. 42). The acquisition procedure was the same as that used with the unprotected tips. The spectra measured during an induction period (15-25 s, varying from tip to tip) were consistent with those observed in the induction period for measurements with the unprotected tips. The general features of blinking observed with the protected tips were also the same as with the unprotected tips. That is, both intensities and positions of peaks fluctuated on a time scale of seconds. However, the time scale over which the blinking persisted was different. After the protected tips had been tested continuously for an hour blinking was still observed. The protected tips were then stored in ambient conditions and re-tested the next day. Spectra collected 24 hours later with the protected tips still exhibited blinking. A spectrum collected at a time of 106,800 s after initial contact is included in Fig. 42. **Thus, the protective coating extended the lifetime of the metallized probe from minutes to days.** The percentage of tips that exhibited blinking also increased with the protective coating: 50% for the unprotected tips vs. 80% for the protected tips.

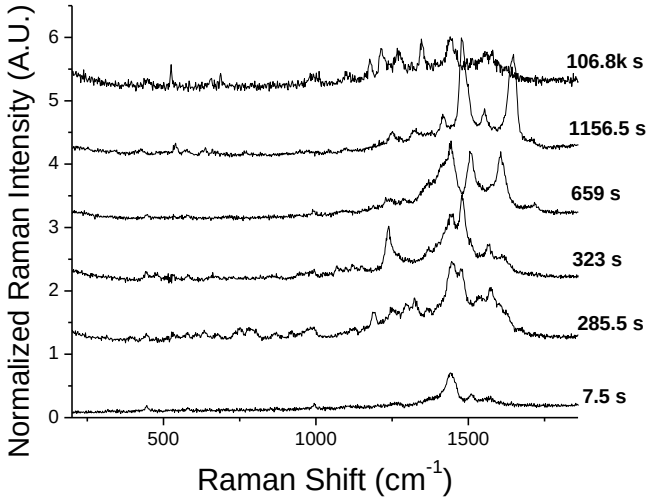

Figure 42. Selected spectra of a PEDOT/PSS film obtained with an alumina protected metallized tip. The time elapsed after the tip came into contact with the sample surface is shown to the right of each spectrum. The spectrum labeled 7.5 s is a typical SERS spectrum for PEDOT/PSS. The spectra have been offset for clarity.

The contrast[7] for each tip is given by:

$$Contrast = \frac{I_c - I_w}{I_w} = \frac{I_c}{I_w} - 1 \qquad [1]$$

where I_c is the integrated intensity of the Raman peak (peak area) when the tip is in contact with the sample and I_w is the integrated intensity when the tip is removed from the sample. To estimate the enhancement factor for the signal, the ratio of the volumes contributing to the far-field signal, V_{FF}, and to the near-field signal, V_{NF}, must be taken into account.

$$Enhancement\ Factor = Contrast\left(\frac{V_{FF}}{V_{NF}}\right) \qquad [2]$$

The enhancement factor varies remarkably with the peak and time at which the spectrum was acquired. For example, contrasts for the peak centered around 1370 cm^{-1} in Fig. 41 range from 3.3 to 9.2. If the diameter of the incident laser beam is one micron and the diameter of the tip is 40 nm, a value of ~ 1600 can be calculated for the ratio of the volume from which the far-field signal comes to the volume from which the near-field signal comes. Assuming the enhancement is coming from the entire volume affected by the enhanced field around the tip, this variation in values of contrast corresponds to variations in enhancement from 5 x 10^3 to 1 x 10^4. If one considers that the enhancement is only coming from a very small gap region or a hot spot (instead of the entire volume underneath the tip), one could easily calculate enhancement factors on the order of 10^7 or higher. In the absence of precise information on the enhancement volume involved we do not attempt to go farther in discussing the enhancements achieved.

To distinguish between two mechanisms proposed for blinking, data were also collected from two hard substrates in which the constituent molecules do not readily diffuse, a CdS thin film and a silicon wafer. Data acquired from a silicon wafer cleaned in the manner described above are shown in Fig. 43. For the first several seconds, only the silicon peak at 520 cm^{-1} is present in the spectra. After an induction period of ~15-20 s the spectra exhibit additional peaks that fluctuate in intensity. The form of the spectrum returns to that typical of pure silicon between periods of blinking (e.g. spectrum at 48 s, Fig. 43). This is analogous to the on and off behavior seen with the PEDOT/PSS sample. We note that the silicon peak does not exhibit *any* changes in peak position or intensity as a function of time. This is consistent with our expectation. At any given time the spectrum observed is dictated by the analyte present in a hot spot. Silicon atoms from a single crystal cannot diffuse in and out of the hot spot(s) on the tip at the temperature prevailing in the experiment and therefore the silicon peak should not exhibit any blinking. The additional peaks that are observed during blinking are in the 1250-1500 cm^{-1} range, indicating that organic molecules, most likely from the air or adsorbed onto the sample surface, are diffusing into and away from the hot spot(s) of the tip.

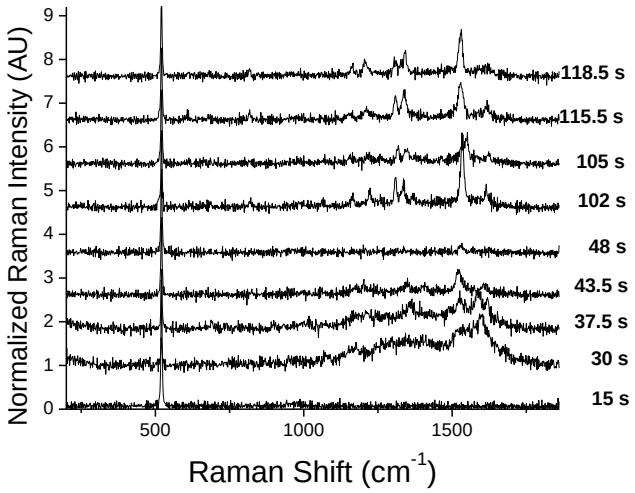

Figure 43. Selected Raman spectra of a silicon wafer obtained with an unprotected tip. The time elapsed after the tip is brought into contact with the sample surface is shown to the right of each spectrum. The spectrum labeled 15 s is typical of silicon. The spectra have been offset for clarity.

Spectra measured on a second hard, non-diffusing sample of CdS, are shown in Fig. 44. A typical CdS spectrum was observed for the first ~10 s, after which time spectral fluctuations were observed. No fluctuations were observed for the CdS peak at 305 cm^{-1}. This observation is consistent with the diffusion mechanism of blinking, because no CdS diffusion is expected. Again, the range of Raman shift over which fluctuations were observed, 1250-1600 cm^{-1}, is consistent with assignment of the fluctuating peaks to some organic contamination from the air or sample surface diffusing into the hot spot(s) of the tip.

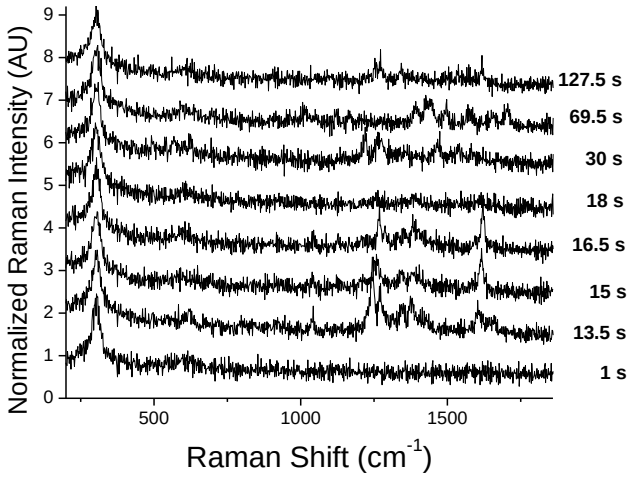

Figure 44. Selected Raman spectra of a CdS film obtained with an unprotected tip. The time elapsed after the tip is brought into contact with the sample surface is shown to the right of each spectrum. The spectrum labeled 1s is typical of CdS. The spectra have been offset for clarity.

The mechanism of blinking is not well understood. One of the proposed mechanisms is thermally activated diffusion[38, 50-55] of analyte molecules into and out of hot spots. The blinking signal would then be dominated by the molecules resting in the hot spots during any given spectral acquisition. Another proposed mechanism is the charge transfer or chemical mechanism[56-58]. This mechanism attributes spectral fluctuations to conformational changes the analyte molecule experiences as it binds to or detaches from the plasmonic structure that is providing the enhanced electric field. These conformational changes are induced by a sharing of electrons or holes between the metal and the analyte molecule. Although the mechanism of blinking is still a subject of debate, there is a consensus that any observation of blinking indicates high enhancement of the Raman signal. This is supported by theoretical calculations predicting that at least ~10^8 enhancement is necessary to observe blinking[59].

The results presented here lead to several general observations. First, an induction period is required before blinking is observed. This induction period probably corresponds to the time needed for the sample to heat sufficiently for the molecules to diffuse. The second observation is that the characteristic peaks for the hard samples, CdS and silicon, do not fluctuate in position or intensity during the entire measurement time. This is in striking contrast to the spectra from the soft polymer blend, which exhibit significant fluctuations in the characteristic polymer peaks (e.g. the peak at 1444 cm^{-1} from the symmetric C=C-O stretch and the peak at 1365 cm^{-1} from the C-C stretch, Fig. 41). The intensity of the C=C-O peak varies in time from being the highest intensity in the spectrum to being a relatively low intensity. The shapes of the peaks also change. The C-C peak position varies by ± 7 cm^{-1} and its intensity also varies widely. These spectral fluctuations are consistent with the diffusion mechanism for blinking. However, the question remains as to whether the peaks that are blinking in Fig. 41 can really be ascribed to the polymer or perhaps, result from airborne contaminants. To address that question one may compare the spectra in Figs. 41, 43, and 44. It is clear that the features seen in the range of organic modes are clearly different between Figs. 41 and 43 and between Figs. 41 and 44. Though one cannot exclude the possibility that the species causing the blinking in Figs. 43 and

44 are also partly responsible for the blinking in Fig. 41, the spectra in Fig. 41 are richer in features and look much more like the PEDOT SERS spectrum. Therefore we infer that in the case of the soft sample, polymer molecules or portions of polymer molecules are moving into and out of hot spots. Observation of the similarities of the blinking in the spectra in Figs. 41 and 42 acquired with unprotected and protected metallized tips leads to two other important conclusions. First, even when the protective coating is present, extreme enhancement persists. The coating does not destroy the optical properties of the plasmonic structure responsible for hot spots. As has been shown in an earlier paper[10], a thin alumina coating does not affect tip-induced enhancement in any significant way. The second conclusion is that neither the chemical enhancement or charge transfer mechanism, nor gross morphology changes of the plasmonic structure can be dominating factors in the blinking effect. The protective alumina coating has a thickness of 2-3 nm and should eliminate charge transfer. For this mechanism the distance between the analyte molecule and the plasmonic structure is crucial. The protective coating of alumina conformally follows the surface of the silver layer, preventing any of the analyte molecules from coming into direct contact with the plasmonic structure. Yet, the blinking effect remains as strong as in the case of unprotected tips. Furthermore, the alumina coating also protects the silver plasmonic structure from distortion by heating[10]. This excludes the possibility that the blinking observed is a direct result of gross morphology changes in the plasmonic structure. All these observations are consistent with the molecular diffusion mechanism being the major source of the blinking effect.

It is important to clarify what role drift may play in the observation of blinking. Tip drift is a slow change in the tip-sample position due to thermal effects, a known issue in AFM. In these experiments the drift was minimized by allowing the AFM to warm up for at least 40 minutes before any measurements were made. Even so, some tip drift does occur so that the tip is not in *exactly* the same position several minutes after contacting the sample. Although this drift may slightly affect the blinking, we do not believe that it is the strongest factor for several reasons. Firstly, TERS imaging performed by scanning over the PEDOT/PSS surface with a tip not exhibiting any blinking shows a uniform Raman signal across the entire scan. This indicates that even if a tip drifts a few nanometers from its original contact position, the same spectrum is anticipated due to the uniformity of the same evidenced by the TERS scanning. Secondly, blinking is a known phenomenon that occurs not only in TERS, but also in SERS[26-29]. In SERS experiments there is no tip present that can drift. Tip drift can therefore *not* be causing the blinking in those experiments. When the tip is introduced into the system, the drift may have some impact on the blinking but is not responsible for the observation itself. Thirdly, TERS data have been collected where the tip is exposed to the incident beam in air with no contact to a sample. When just in air, no Raman signal is observed. Breathing on the tip led to the observation of blinking for several seconds (Fig. 45). After several seconds, no Raman signal was observed. Blinking could be observed again by breathing on the tip again. The molecules present in the breath had to diffuse into the tip hot spot to produce any Raman signal. This supports a diffusion mechanism and is consistent with the assertion that tip drift does not significantly influence the results presented.

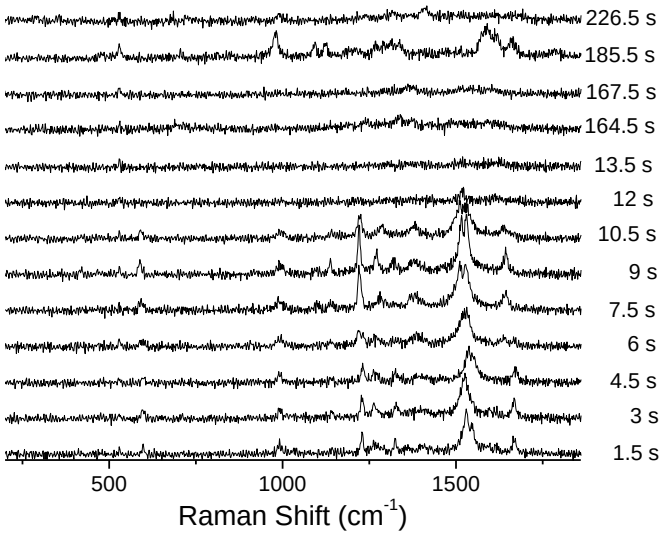

Figure 45. Selected Raman spectra collected from an unprotected metalized tip with the tip hanging in the air, not in contact with any sample. The time labeled on the right is the time elapsed after blowing on the tip. Strong blinking is observed for 12 s after which the spectra do not show any distinguishing peaks. The tip was breathed on again at time 183 s. Blinking was once again observed. This supports a diffusion mechanism because strong blinking is observed as molecules in the breath move into the tip hot spot.

In conclusion, we demonstrate that the lifetime of extreme enhancement by tips in TERS experiments evidenced by blinking can be increased from a few minutes to a few days by the addition of a protective alumina coating. The fact that blinking persists in the presence of the coating excludes charge transfer as the major mechanism of the blinking effect. All the observed results are consistent with molecular diffusion into and out of hot spots as the major mechanism of blinking. In particular, the existence of an induction period for all of the blinking phenomena and its appearance and disappearance during the observation time are well explained by molecular diffusion.

Subgoal 6c: Determine the detection limit obtainable with TERS blinking for polymeric samples

Recent work by Van Duyne *et al*.[60] has recently demonstrated the single molecule detection capabilities of TERS using a mixture of isotopically labeled resonant Rhodamine 6G dye molecules. Identification of individual isotopes was possible at different times after analysis of the blinking data collected from a submonolayer covering of these dye molecules on a hard substrate. In order to test the sensitivity of the probes in this work and to investigate potential usefulness of the blinking phenomena, measurements were performed on a thin polystyrene (PS) film. While PS is Raman active in bulk, it is not detectable as a thin film without long acquisition times due to its weak scattering signal. Unlike the PEDOT/PSS blend used above, PS is nonresonant at the wavelength used in the study. That means that the incident light is not

near the frequency of an electronic transition for PS. The detected signal from PS would therefore be weaker than that of PEDOT/PSS with all collection variables held equal.

The thin film studied was a blend of deuterated linear polystyrene (d-LPS) and hydrogenous linear polystyrene (h-LPS) containing 20 wt% h-LPS. Both the d-LPS and h-LPS had molecular weights that were nominally 2 kg/mol. The molecular characterization for these two polymers is shown in Table 5. The polymer blend was spun cast from a 1wt% solution in toluene onto a hydrofluoric acid etched silicon wafer. It was then annealed at 120°C for 12 h. The d-LPS was isotopically labeled so that it could be distinguished from the h-LPS in the Raman spectrum. The Raman spectra of bulk d-LPS and h-LPS samples have characteristic peaks[61] at 976 cm^{-1} and 1002 cm^{-1}, respectively. This difference in the peak positions of the selected vibrational band for the two isotopic species is larger than the frequency shifts caused by spectral wandering (± 5 cm^{-1}) observed during blinking and allows one to easily distinguish between the two isotopes. This is the first time that isotopic polymeric species have been distinguished using TERS. Blinking data (1s acquisition time) were collected from the surface of the film using alumina protected silver metallized probes.

Table 5. Molecular characterization of polymers used

Polymer	M_n[a] (g/mol)	PDI[a]	T_g[b] (°C)
h-LPS	2300	1.05	61
d-LPS	2000	1.03	60

[a] SEC coupled with light scattering (± 5%) in THF at 30°C.
[b] Determined by DSC: heating rate, 10°C/min; recording second run, ± 1°C.

Representative blinking spectra from the surface of the d-LPS/h-LPS blend film are shown in Fig. 46. When no probe was present, no signal could be detected from the surface of the blend film. When the tip was brought into contact with the surface, blinking was observed. During different spectral acquisitions, spectra distinctly featuring d-LPS, both isotopes, or only h-LPS were observed (Figs. 46a,b,c respectively***). This is the first demonstration of the detection of distinct isotopic polymeric species with TERS using a nonresonant analyte.***

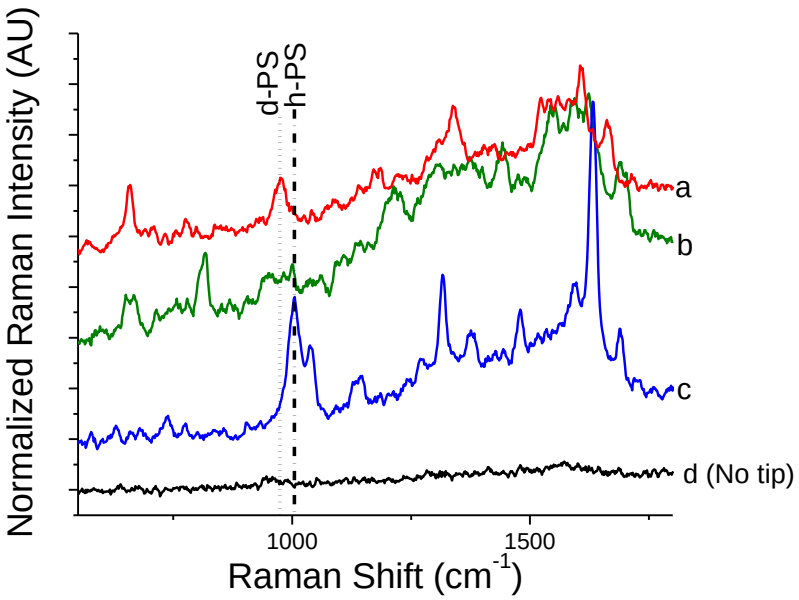

Figure 46. Representative blinking spectra acquired from the surface of a d-LPS/h-LPS blend film containing 20 wt% h-LPS. The spectra have been offset in the vertical direction for clarity. Each spectrum was collected with a 1 s acquisition time. In different spectra, a) only d-LPS, b) both d-LPS and h-LPS isotopes, or c) only h-LPS were detected. d) No analyte could be detected when the tip was not present.

This experiment adds further support to the contention that thermal diffusion is the mechanism behind blinking[46]. The individual isotopes cannot be detected until localized heating from the incident laser beam focused on the tip apex has taken place. This is consistent with the idea that the sample must first transition from a glassy to a melt state underneath for blinking to occur. Molecular diffusion in glasses is extremely small. The d-LPS/h-LPS blend has a T_g of 60°C, which is above room temperature, but as we have shown in earlier work[47], the strong electric field enhancement beneath the tip can readily cause heating of 40°C or more above ambient. We remark that the mechanism for molecular mobility proposed in Van Dyne's work[60] with small molecule (dye) analytes is not active there. There it was argued that blinking was observed from a small molecule (dye) analyte merely due to the fact that a meniscus of water forms between the tip and underlying surface and the analyte can move about readily in the water. Here a water layer, even if present, would do little to make the molecules move (since PS is hydrophobic and not soluble in water).

Subgoal 6d: Determine if TERS blinking data can be quantified to determine the surface composition of polymer blends

In addition to detecting individual isotopes, it would be of interest to quantify the surface composition of blend films using TERS. This would be of particular interest for looking at the surface composition of blends that have undergone surface segregation. To that end, a series of

single point (not scanning) blinking experiments used for isotope detection have been performed on blends of varying composition. Initially, two isotopically labeled 2k LPS blend samples were analyzed. One blend contained 80 wt % of the d-LPS species, while the other contained 20 wt % of the d-LPS species. Both polymer films were spun cast onto aluminum mirrors and annealed for 6 h at 120°C under high vacuum. The polymers used were the same as characterized above in Table 5. For all single point blinking experiments the spectral acquisition time was set to 1 s and blinking data were collected for several minutes at a single location. Data were collected from three individual locations on each sample. In each data set, the spectra containing characteristic peaks of either d-LPS or h-LPS were identified. The peak areas for each species in the spectra were then used to calculate the relative surface composition. A summary of the data is shown in Table 6. In the case of the blend containing 80 wt % d-LPS, an average of 76 (± 4)% of the observed polystyrene peaks were from the deuterated species, while in the blend containing 20 wt % d-LPS, an average of 50 (± 7)% of the observed polystyrene peaks were found to be from the deuterated species. From this we see that blend composition is related to the peak area of the characteristic peaks for each species observed during TERS blinking. However, there is not a one-to-one correlation between peak area and surface composition. A calibration curve is necessary to measure surface composition.

Table 6. Summary of collected data for TERS from LPS blend films.

	# of Spectra	h-LPS	d-LPS	Total LPS	% d-LPS
80/20 wt % d-LPS/h-LPS	785	25	80	105	76 (± 4)
20/80 wt % d-LPS/h-LPS	1164	102	101	203	50 (± 7)

In attempts to begin building a calibration curve, pure d-LPS and pure h-LPS samples were spun cast onto aluminum mirrors and annealed at the same conditions used for the previous blend samples. The calibration curves are shown in Fig. 47. The film compositions are plotted as a function of % d-LPS contained in the film with the ordinate values being the peak area of d-LPS observed relative to the total peak area of all polystyrene (d-LPS + h-LPS) observed. These preliminary results indicate that TERS blinking is extremely sensitive to contamination, as evident by the apparent 40% d-LPS composition even when the sample was pure h-LPS. Our preliminary explanation for this observation would postulate the consistent presence of a contamimant that has a peak appearing at a location overlapping with that of the benzene breathing mode for dPS. In the future, a more detailed analysis of the spectra involving more than one characteristic peak per analyte molecule of interest may help to minimize this problem. These results, however, do demonstrate that TERS blinking is an effective means of detecting and identifying the presence of small amounts of material on the surface of a sample, even if the analyte is non-Raman resonant. More work is needed to precisely quantify the concentration of unknown material present using TERS blinking.

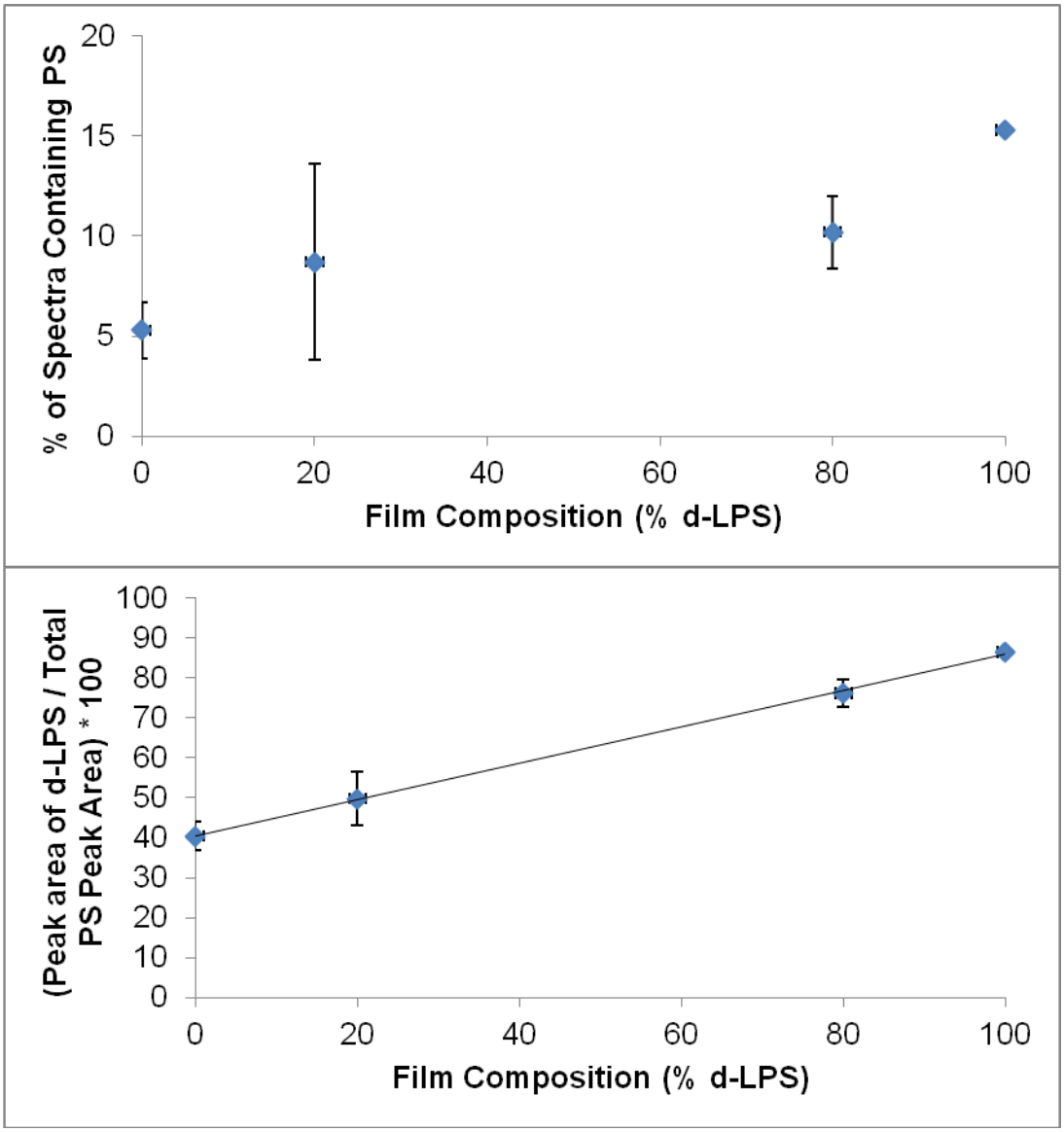

Figure 47. (top) Frequency of blinking observed as a function of film composition as measured by % of total acquired spectra containing the benzene breathing mode peak for either hPS or dPS. (bottom) Potential calibration curve for TERS blinking surface composition determination, plotted as ratio of peak area apparently due to dPS to peak area for all PS.

There are currently only a few techniques capable of the quantitative analysis of blend composition in the top few nanometers of a film, particularly when the components being distinguished differ only subtly. Static Time-of-Flight Secondary-Ion Mass Spectrometry (STOF-SIMS) is directly sensitive to the first molecular layer, but quantitative measurements require complex calibration.[62] Neutron reflectometry is a very high resolution technique for probing the composition depth profile[63-65] if a component can be isotopically labeled. However, it is an indirect technique and cannot be performed at the home laboratory. Matrix-Assisted Laser Desorption/Ionization Time-of-Flight Mass Spectrometry (MALDI-TOF MS) can provide

a direct measurement of chemical composition that discriminates among chains with distinct molecular architecture (if these also differ in *m/z* value),[66, 67] without the need for isotopic labeling. However, polymer analytes are typically dissolved and mixed with matrix for this technique.[68] This is not a realistic way to probe surface composition specifically, which can be altered by the addition of solvent. To extend MALDI-TOF MS to the analysis of the surface specifically, it is necessary to limit the probing depth by modifying the sample preparation method while avoiding any change of the surface composition during sample preparation or measurement. Here we develop an innovative new technique that we term Surface Layer MALDI-TOF MS (SL-MALDI-TOF MS) to unambiguously identify the species preferred at the surface of a novel blend of cyclic polystyrene with linear polystyrene and quantify its composition[2]. After the surface composition is quantified, the blend samples will be suitable for use as additional standards for a more detailed study to determine if TERS blinking can be quantified to determine surface composition.

Proving the probing depth of SL-MALDI-TOF MS

In conventional bulk MALDI-TOF MS, a cationic reagent, silver trifluoroacetate (Ag(TFA)), is carried in a matrix of trans-2-[3-(4-tert-butylphenyl)-2-methyl-2-propenylidene] malononitrile (DCTB). This matrix is mixed with analyte in solvent to increase the sensitivity. During the analysis, a laser beam breaks the cationic reagent up, resulting in the Ag^+ ionizing the polymer analyte. The matrix and analyte are dissolved in solvent and then placed in contact with a conductive substrate for analysis. However, placing solvent on a film sample could change the surface composition. Therefore, in these surface measurements, dry matrix powder was ground up with a vortexer and manually spread on the surface of a polymer film prepared on a metallized silicon substrate. (The conductive metal layer dissipates charges created by the MALDI ionization process[69].) The contact between the matrix/salt and the polymer is *key* to this new approach.

Before SL-MALDI-TOF MS could be demonstrated, it was first imperative to determine the probing depth of this new technique. Monolayers were used as model systems. A monolayer of poly(methyl methacrylate) (PMMA) was deposited on top of a 100 nm thick layer of PS using the Langmuir-Schaefer technique. This PS layer will be denoted as "PS4k" to distinguish it from the polymers used later in the "standard" blends. The molecular characterizations of the PMMA and the PS4k are shown in Table 7. The thickness of the PMMA layer was determined using an AFM image, shown in Fig. 48, at a defect near the film edge. Line cuts through the AFM image show that the PMMA layer is 1-2 nm thick, consistent with the radius of gyration (R_g) of the PMMA. This bilayer sample was fabricated on top of a silicon substrate metallized with 50 nm of gold to ensure charge dissipation during the MALDI ionization process.

Table 7. Characterization of the polymers used to construct the model bilayer film.

Polymer	M_n[a] (g/mol)	PDI[a]
PS4k	4100	1.03
PMMA	2800	1.09

[a] SEC coupled with light scattering (± 5%) in THF at 30°C.

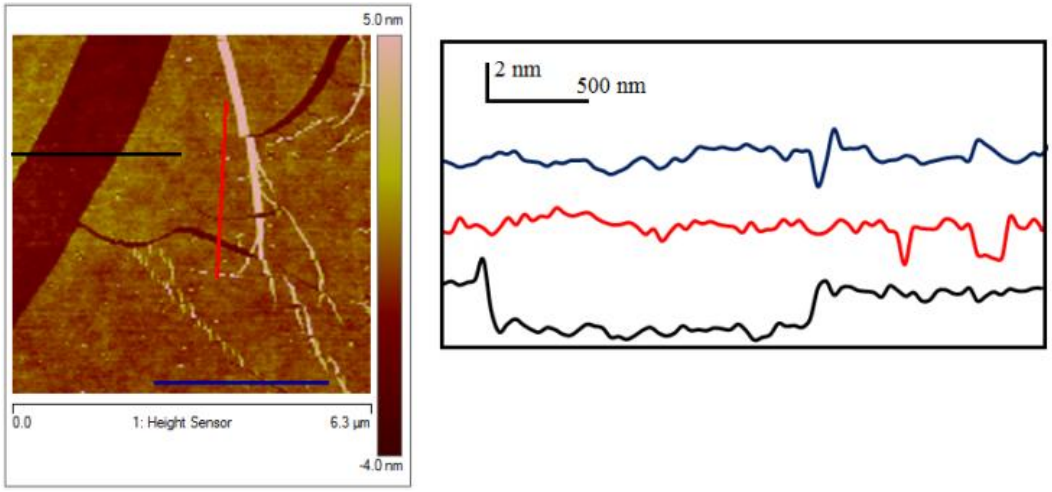

Figure 48. Tapping mode AFM topography image near a defect in the PMMA layer on top of the PS4k film (left) along with corresponding line cuts through the image (right). The line cuts show that the PMMA film is 1 R_g (1-2 nm) thick.

The SL-MALDI-TOF MS spectrum from the bilayer PMMA/ PS4k surface is shown along with those from the bulk reference films of PS4k and PMMA in Fig. 49. The reference PMMA has a number average molecular weight (M_n) of 2,800 g/mol, whereas the PS4k has a M_n of 4,400 g/mol as determined by MALDI-TOF MS. The distributions of the two polymers overlap, allowing for a comparison between the two species. The distribution of PMMA from the bilayer film measured using SL-MALDI-TOF MS appears shifted to lower *m/z* relative to the spectrum for the bulk PMMA reference sample measured using conventional MALDI-TOF MS. The DCTB/ Ag(TFA) system selected ionizes the PMMA less efficiently than it does the PS. (Sodium based salts are more efficient for oxygen containing systems such as PMMA.) A less efficient ionization results in a shift of the distribution to lower *m/z* due to preferential ionization of shorter PMMA chains[70,71].

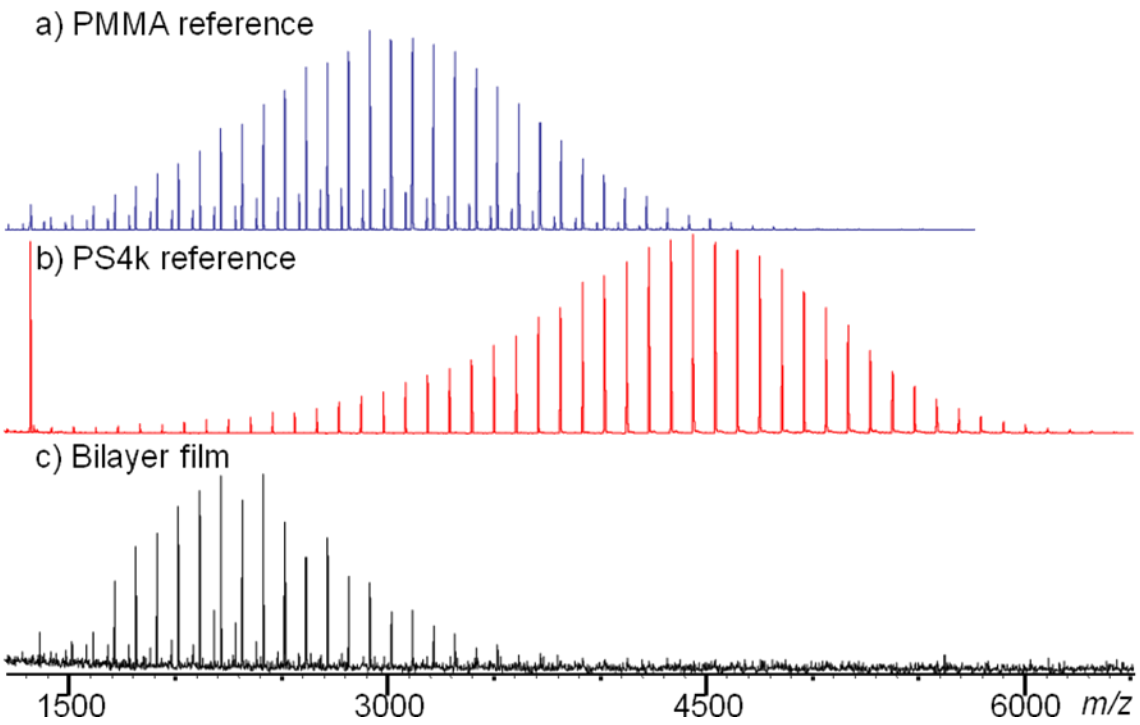

Figure 49. Bulk MALDI-TOF spectra for a) pure PMMA, and b) pure PS4k. c) SL-MALDI-TOF spectrum from the surface of the PMMA/ PS4k bilayer film.

The SL-MALDI-TOF MS spectrum from the bilayer film has a single distribution of species, with a mass difference between fragments of 100 Da, consistent with sampling of the PMMA. This is shown clearly in the enlarged view of the fragmentation patterns shown in Fig. 50. No PS signal was detected, even in the region where PS should have given strong peaks. This region is enlarged in Fig. 51. The only signal observed originated from the top PMMA layer which was only a monolayer thick (1-2 nm), confirming that the probing depth of SL-MALDI-TOF MS is about R_g with these chains.

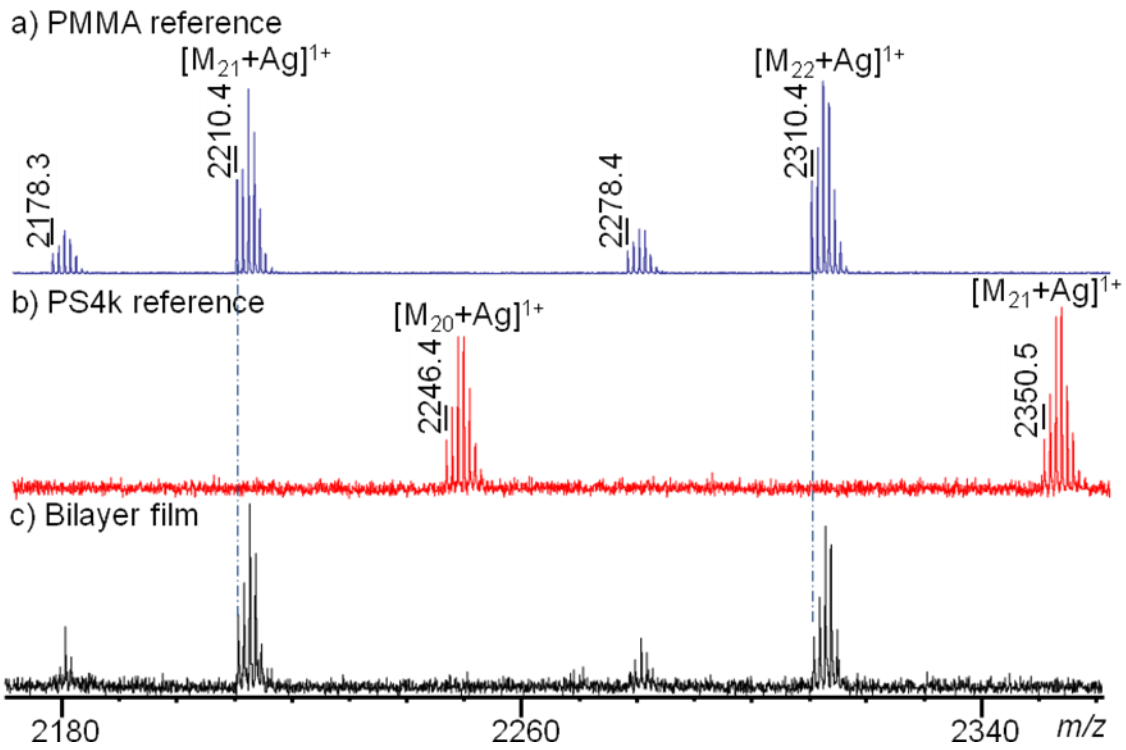

Figure 50. Enlargement of the 4270-4450 portion of the spectrum of Figure 6.2 for a) bulk MALDI-TOF spectra for pure PMMA, b) bulk MALDI-TOF spectrum for pure PS4k, and c) SL-MALDI-TOF spectrum from the surface of the PMMA/ PS4k bilayer film. No PS4k was detected.

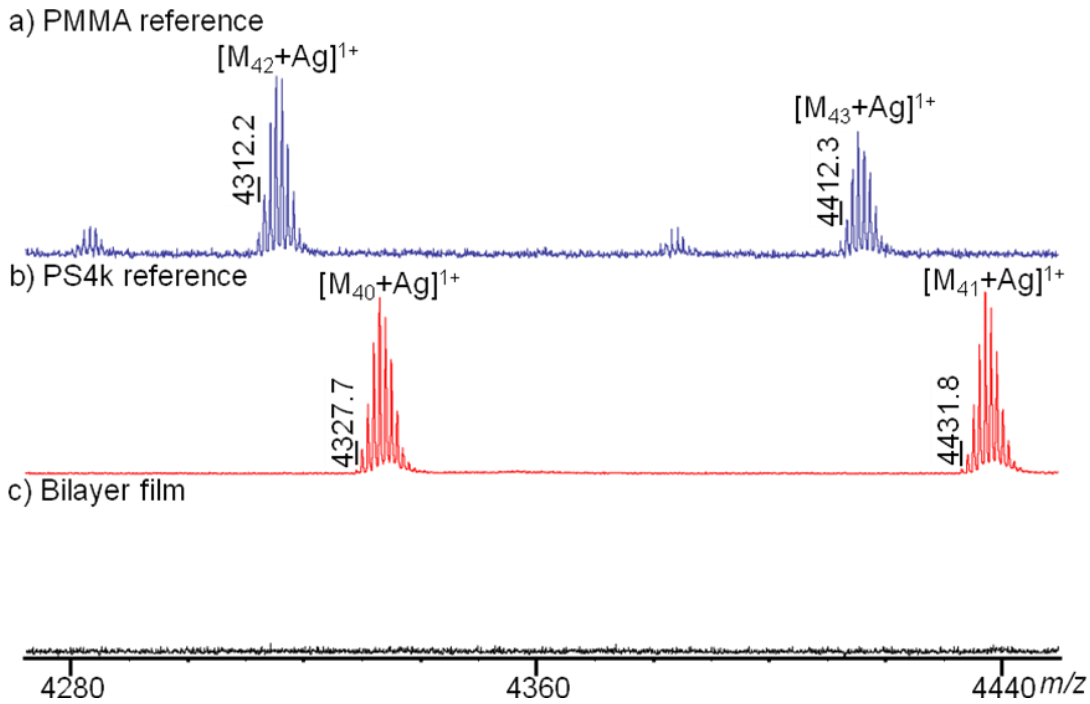

Figure 51. Enlargement of the *m/z* 4270-4450 portion of the spectrum for a) bulk MALDI-TOF spectra for pure PMMA, b) bulk MALDI-TOF spectrum for pure PS4k, and c) SL-MALDI-TOF spectrum from the surface of the PMMA/ PS4k bilayer film. No peaks are observed for the bilayer sample in this region. PS4k peaks would be the strongest in this region if any PS4k were being detected.

To test the possibility that the PS4k in the bilayer film might not have been detected due to some sort of interference from the PMMA layer or from PMMA suppressing the PS4k signal, an additional bilayer sample was analyzed. This bilayer sample was created using the Langmuir-Schaefer technique to transfer a *partial* monolayer of PMMA onto the surface of a 100 nm thick PS4k film. The partial monolayer was created by following the same experimental procedure for the full monolayer, but increasing the area to which the monolayer was compressed to create a buckled film. A representative AFM image of the surface of this sample, shown in Fig. 52, shows that the sample contained stripes of PMMA on top of the PS4k layer. The SL-MALDI-TOF spectrum from a region of this sample that did not contain any PMMA is shown in Fig. 53c. Only the PS4k was detected in such regions. If another spot on the sample that did contain PMMA stripes was chosen, the data were consistent with the SL-MALDI spectrum of PMMA shown in Fig. 49c. The fact that PMMA or PS4k was detected at different spots depending on what material was at the surface suggests that there was no interference with or suppression of the spectrum due to proximity of the two types of layers alone. Simply, the top molecular layer in the beam path was detected at any given location of the laser beam.

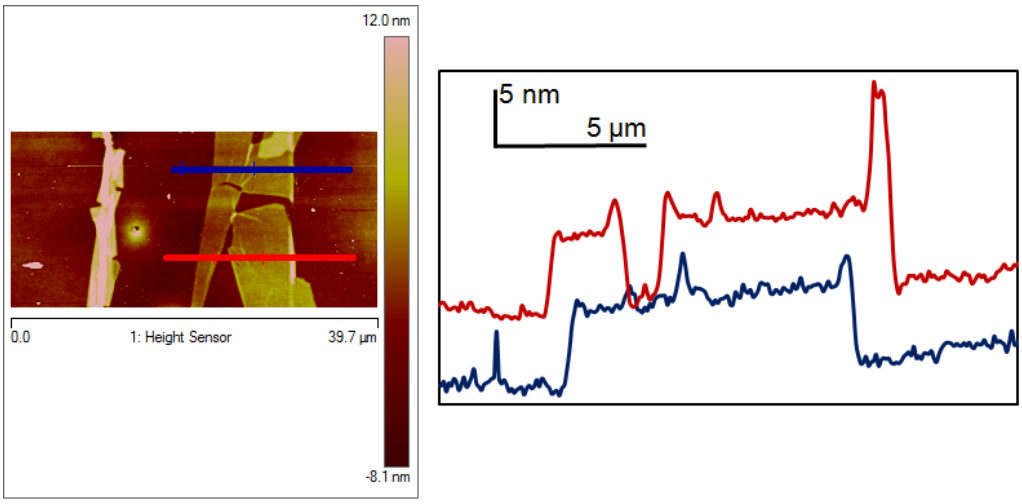

Figure 52. Tapping mode AFM topography image near a stripe of PMMA layer atop the PS film (left) along with corresponding line cuts through the image (right). The line cuts show that the PMMA film is not a continuous monolayer.

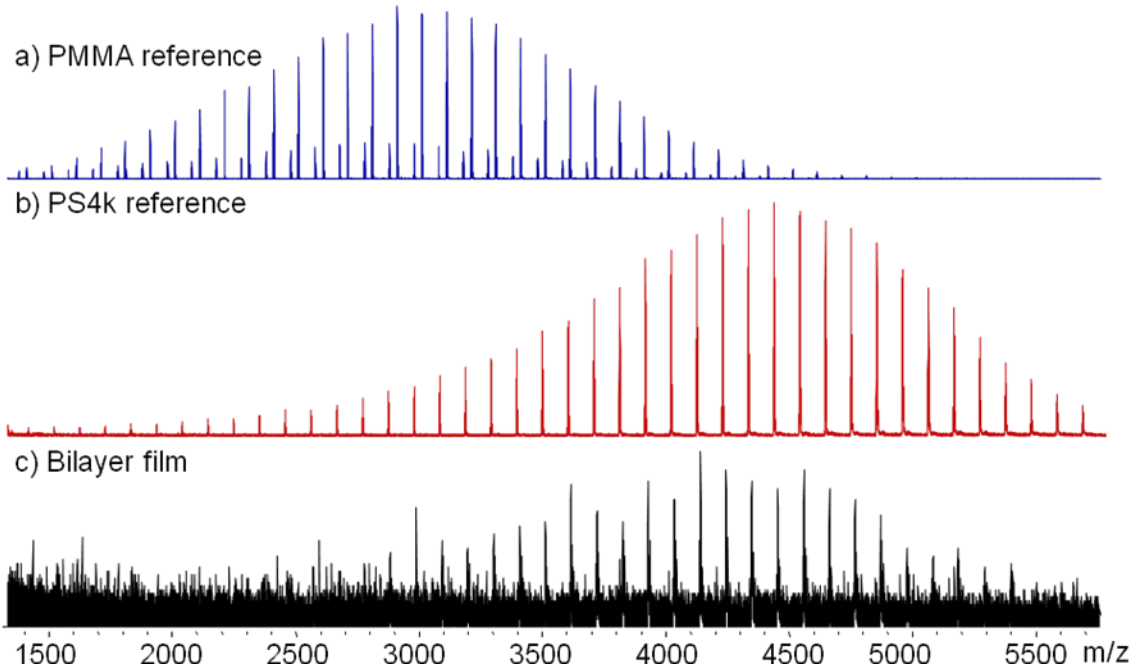

Figure 53. Bulk MALDI-TOF spectra for a) pure PMMA b) and pure PS4k. c) SL-MALDI-TOF spectrum from a spot on the surface of the PMMA/ PS4k bilayer film where no PMMA stripes fall within the laser spot. For this spot, only species from the PS4k layer were detected. When a spot was chosen in which a PMMA stripe was present, the data observed were consistent with the SL-MALDI spectrum of PMMA presented earlier in Figure S10c, with no evidence of PS4k.

The confirmation of the actual probing depth of this new technique is significant because analysis of the sample with optical microscopy, images shown in Fig. 54, after the SL-MALDI-TOF MS measurement revealed large holes in the films. The images also show the dry matrix particles, which appear as dark raised regions against the yellow-orange surface of the sample.

The matrix particles do not uniformly cover the surface and vary in size from a few to tens of microns in diameter.

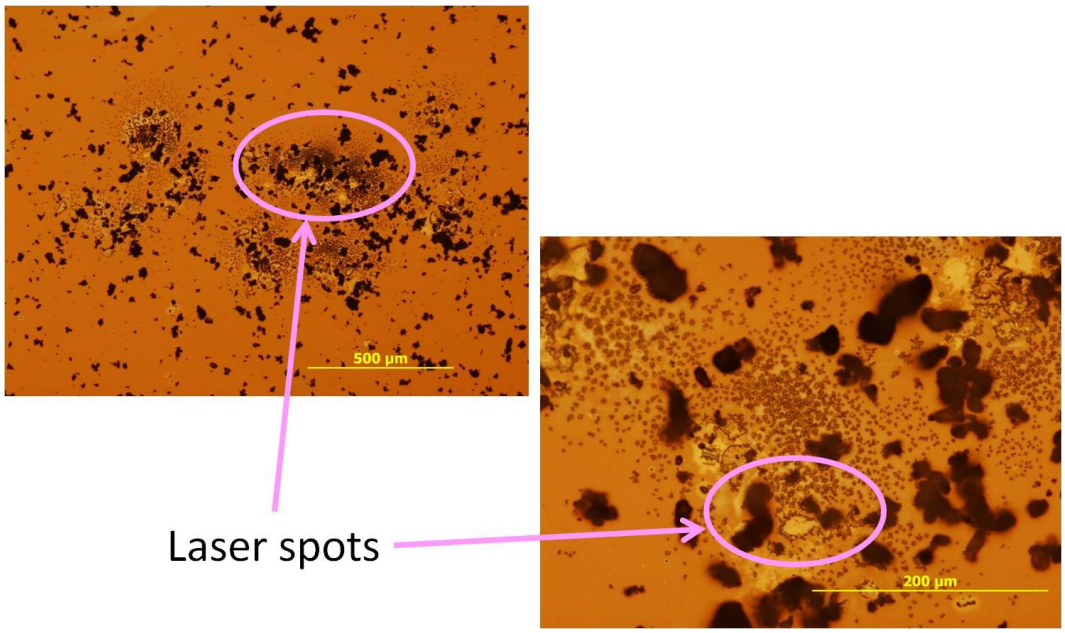

Figure 54. Optical microscopy images showing laser induced damage to the polymer sample. The laser spots at two different magnifications are marked with pink circles.

The optical microscopy images suggest that the laser burns a hole through the entire polymer film, ablating all of the polymeric material in the beam path. The AFM images, shown in Fig. 55, reveal that the morphology at the bottom of the laser spot is consistent with that of the underlying gold film. However, only the species in direct contact with the matrix and salt mixture at the surface of the film was detected in the SL-MALDI-TOF MS analysis.

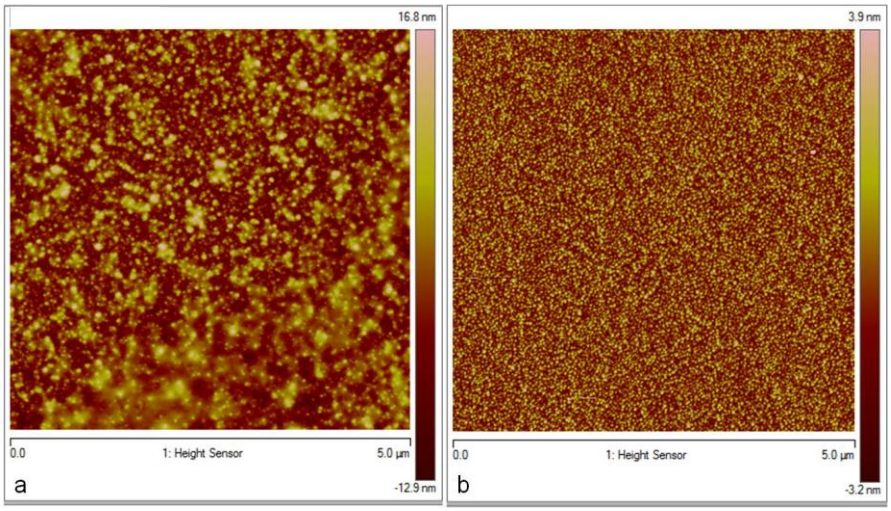

Figure 55. AFM images of a) the bottom of the laser hole and b) the morphology of a reference gold film before the addition of polymer. After SL-MALDI-TOF MS measurements, the morphology in the laser spot is consistent with the morphology of the gold film, indicating that both polymer layers have been removed.

Demonstration of SL-MALDI-TOF MS using two Polymer Blends

After the probing depth of SL-MALDI-TOF MS was demonstrated to be monomolecular, this technique was used to investigate the surface composition of two polymer blends that can later be used as standards for the TERS measurements. Molecular characterization data for the hydrogenous cyclic PS (h-CPS), hydrogenous linear PS (h-LPS), and deuterated linear PS (d-LPS) used are summarized in Table 8. The well-defined h-CPS2k was synthesized by Shih-Fan Wang[72]. Deuteration of the linear species provided contrast for study with STOM-SIMS as well as SL-MALDI-TOF MS.

Table 8. Characterization of the polymers used in blend films.

Polymer	M_n[a] (g/mol)	PDI[a]	T_g[b] (°C)
h-CPS	2700	1.03	87
h-LPS	2300	1.05	61
d-LPS	2000	1.03	60

[a]SEC coupled with light scattering (± 5%) in THF at 30°C.
[b]Determined by DSC: heating rate: 10°C/min, recording second run (± 1°C).

The conventional MALDI mass spectrum from a bulk sample of a h-CPS/d-LPS blend with 20 wt% h-CPS is shown in Fig. 56 along with the SL-MALDI spectrum from the surface of a thin film of the same blend after annealing for 12 h at 125°C. The relative intensity of the h-CPS spectrum is a factor of three smaller at the surface of the film than in the bulk. The surface concentration of d-LPS was quantified using a calibration curve, shown in Fig. 57, constructed using ratios of the peak area of d-LPS (*m/z* at 2407.4 Da) to the sum of peak areas for h-CPS (*m/z* at 2349.4 Da) and d-LPS for several standard bulk blends mixed with solvent and measured with conventional bulk MALDI. The d-LPS surface concentration of the linear/cyclic blend film was 88.3 (± 1.6) wt% before annealing. The time during which the chains are mobile while there is sufficient solvent in the film is less than one minute. It is notable that segregation occurs even before annealing. After annealing the film at 120°C for 12 h, the enrichment of linear chains at the surface is the same within the uncertainty, 89.3 (± 2.8) wt%. Contrary to self consistent field theory (SCFT) prediction[7], there is a strong *depletion* of the cyclic chains from the surface.

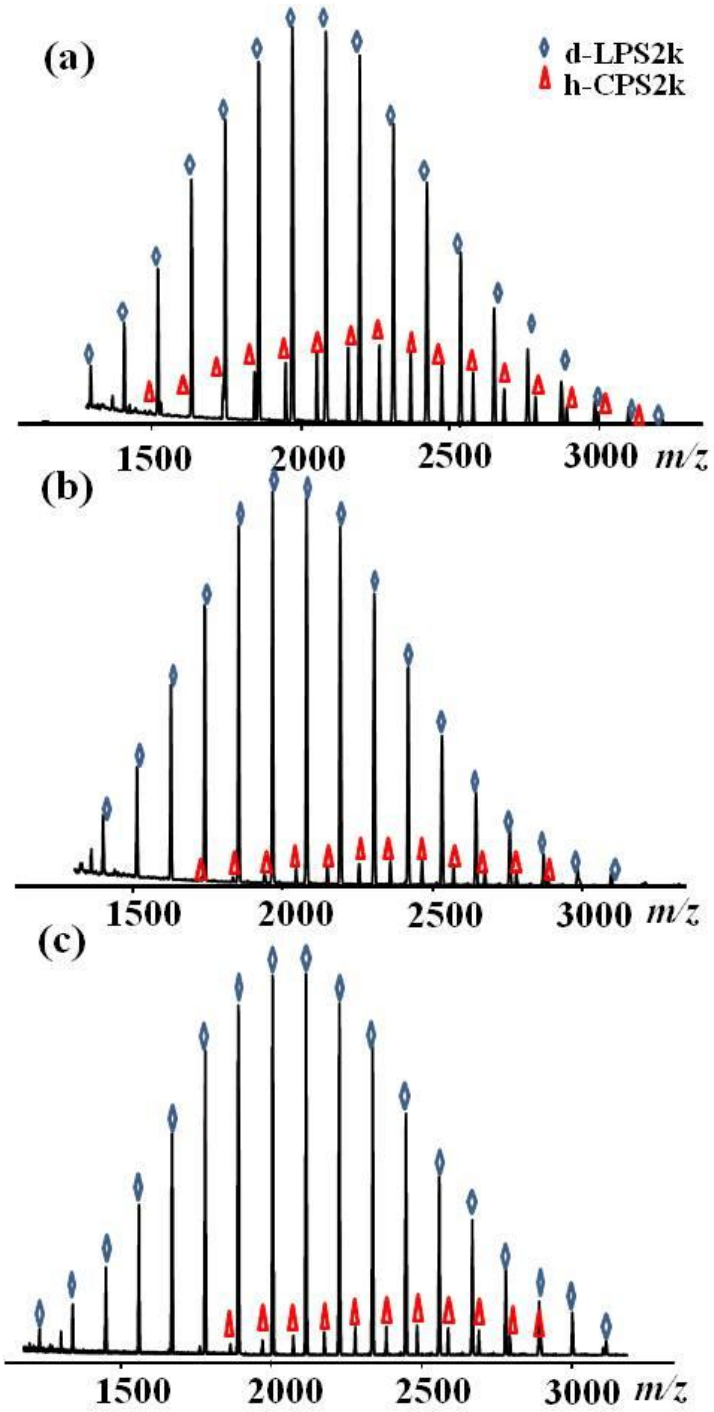

Figure 56. a) MALDI-TOF MS spectrum of a bulk sample of h-CPS/d-LPS blend with 20 wt% h-CPS, b) SL-MALDI spectra from the surface of a thin film of the same blend before annealing, and c) after annealing at 120°C for 12 h. The mass difference between pairs of peaks in the distribution for d-LPS is 112 Da and that for the distribution of h-LPS is 104 Da.

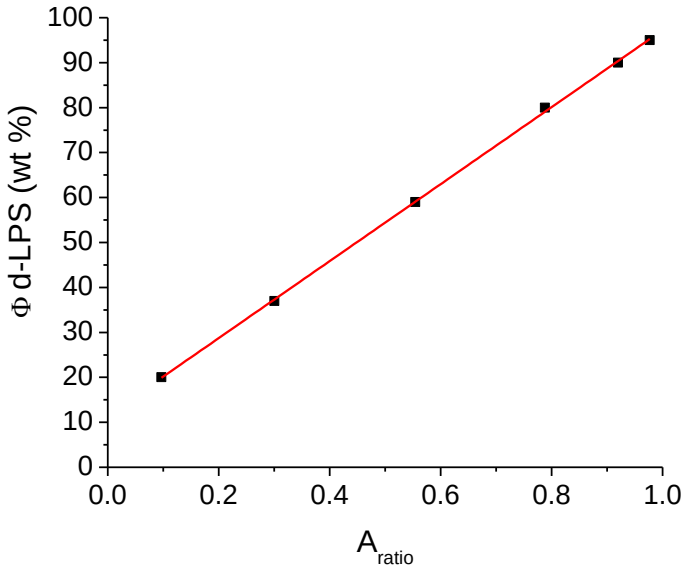

Figure 57. Calibration curve (line) for h-CPS2k/ d-LPS2k blend from bulk MALDI-TOF MS data (squares). The uncertainty is less than the size of the symbols.

In binary blends of hydrogenous and deuterated polystyrene, the deuterated species enriches the blend surface when the two polymers have similar chain lengths[73]. To ensure that the observed surface depletion of the cyclic species in this work was not due simply to an isotopic effect, a blend of h-LPS/d-LPS containing 20 wt% of h-LPS was also investigated. The SL-MALDI data are shown in Fig. 58. The composition of the blend was obtained using a calibration curve, shown in Fig. 59, constructed using the peak area of the d-LPS (*m/z* 2183.3 Da) to the total area of the d-LPS and h-LPS (*m/z* 2144.5 Da) peaks. The SL-MALDI data, summarized in Table 9, show that the surface composition of the linear/linear blend was 78.6 (± 2.5) wt% d-LPS before annealing and 78.8 (± 2.9) wt% d-LPS after annealing. This agrees well with the as prepared blend composition and indicates that surface segregation due to isotopic labeling alone is not measureable for such short chains.

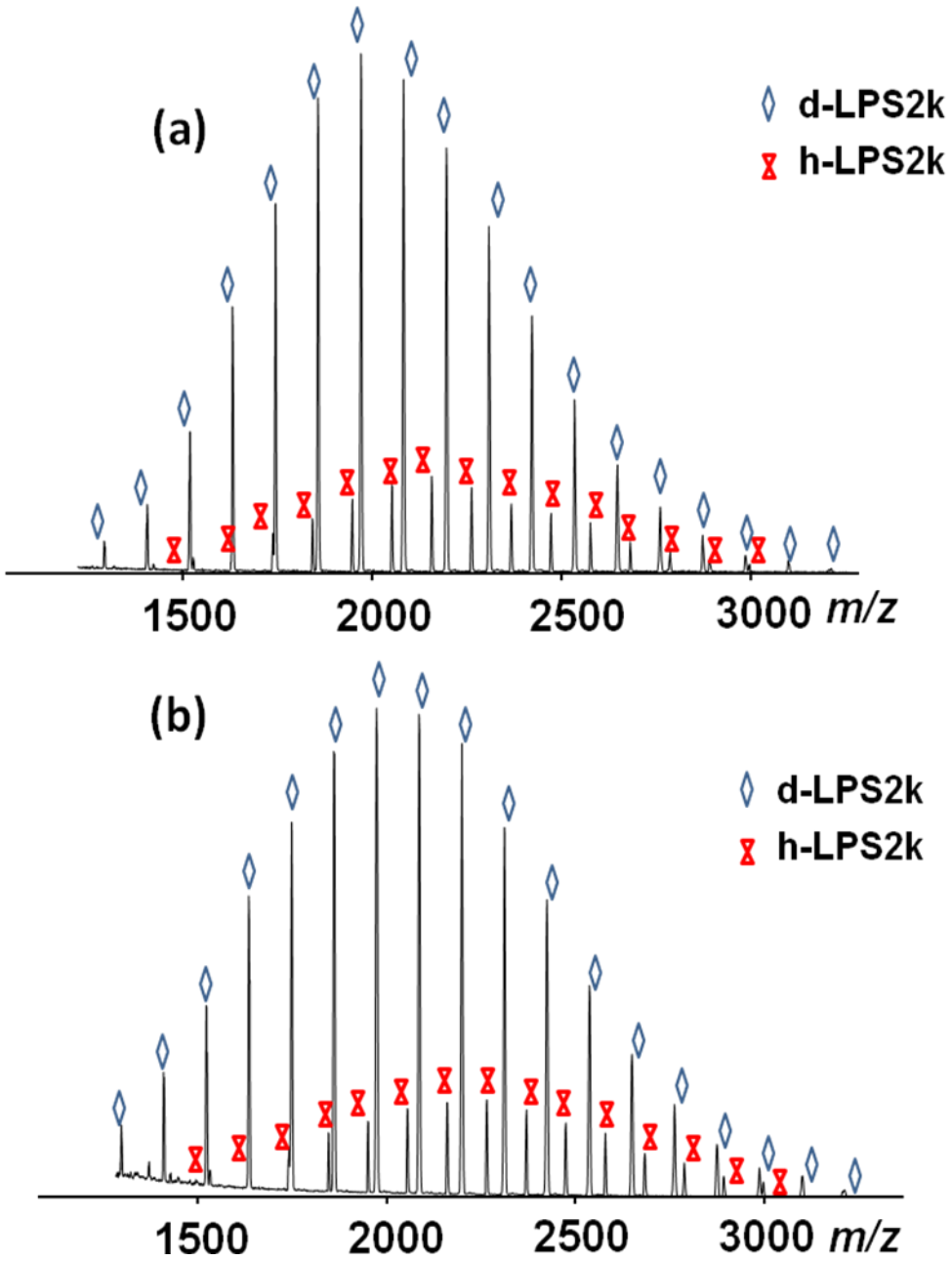

Figure 58. MALDI-TOF MS spectra of (a) bulk sample of h-LPS/d-LPS blend with 20 wt% h-LPS and (b) surface of a film of the same h-LPS/d-LPS blend after annealing at 120°C for 12. The mass difference between pairs of peaks in the distribution for d-LPS is 112 Da and that for the distribution of h-LPS2k is 104 Da.

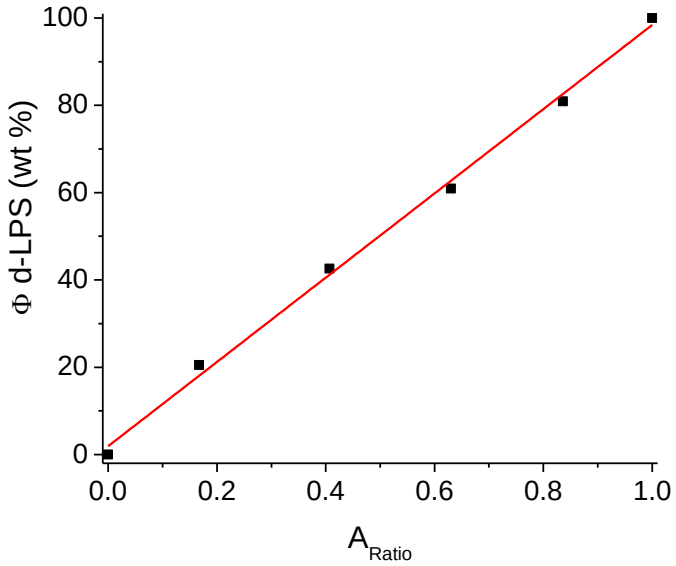

Figure 59. Calibration curve (line) for isotopic linear blend bulk MALDI-TOF MS data (squares). The uncertainty is less than the size of the symbols.

Table 9. Summary of surface composition in cyclic and linear blend films before and after annealing obtained with SL-MALDI-TOF MS.

Sample Type	Annealing	SL-MALDI-MS (wt% d-LPS)
h-LPS/d-LPS (20 wt% h-LPS)	No	78.6 (± 2.5)
	120°C, 12 h	78.8 (± 2.9)
h-CPS/d-LPS (20 wt% h-CPS)	No	88.3 (± 1.6)
	120°C, 12 h	89.3 (± 2.8)

Confirmation of SL-MALDI Results with STOF-SIMS

This interesting observation of the cyclic molecules being *depleted* from the surface was confirmed using STOF-SIMS. STOF-SIMS is a direct technique for determining the relative surface concentration of different species. However, calibration to obtain absolute concentrations is very challenging. Adding an internal standard, which is the most commonly employed method, can alter the surface segregation of the blend under investigation and therefore change the surface composition. We therefore only present ratios of signals rather than absolute concentrations. The fragmentation spectra for the h-LPS/d-LPS and h-CPS/d-LPS blends each containing 20 wt% of hydrogenous PS species were analyzed before and after annealing. The relative amount of deuterated to hydrogenous PS present at the surface of each blend can be calculated using the ratio of the peak areas of the detectable fragments from the d-LPS (*m/z* 95-98) to the peaks areas of the detectable fragments for the hydrogenous PS (*m/z* 91-92).

The linear/linear blend was first measured to determine the ratio value one might expect for the overall composition in the cyclic/ linear blend in the absence of surface enrichment.

Representative fragmentation spectra for the h-LPS/ d-LPS blend before and after annealing are shown in Fig. 60. Representative peak areas are shown in Table 10. The ratio of deuterated to hydrogenous species at the surface is 4.4 (± 0.6) before annealing and 4.2 (± 0.1) after annealing. Representative fragmentation spectra for the h-CPS/ d-LPS blend before and after annealing are shown in Fig. 61. The ratio of deuterated to hydrogenous species at the surface is 7.3 (± 0.4) before annealing and 9.8 (± 0.3) after annealing. These relative ratios for each blend before and after annealing are summarized along with the surface concentrations obtained from SL-MALDI measurements in Table 11.

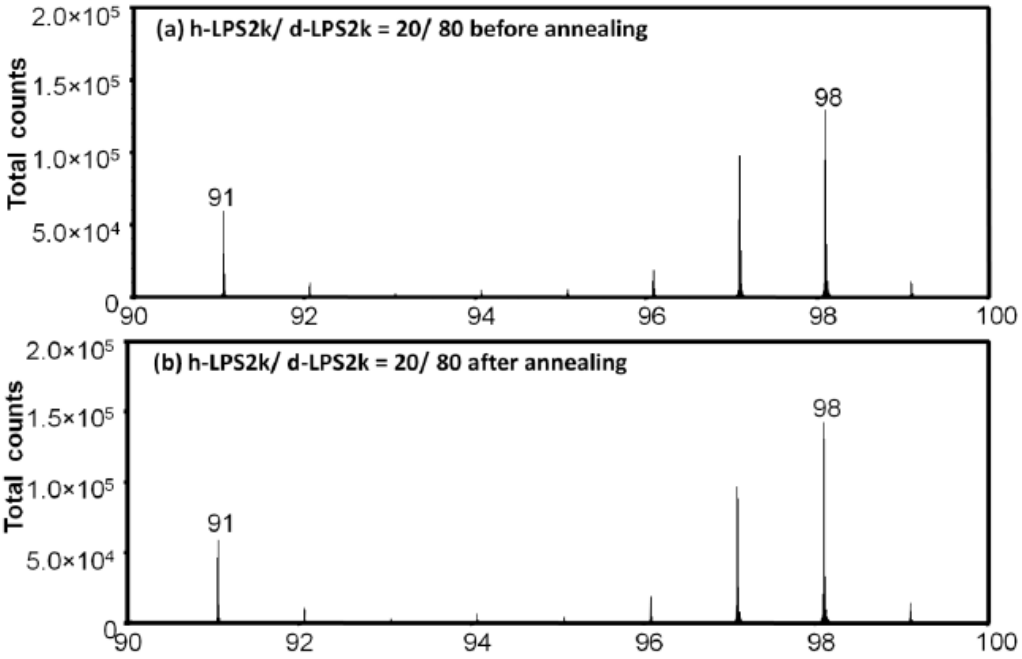

Figure 60. STOF-SIMS fragmentation spectra of a h-LPS/ d-LPS blend containing 80 wt% d-LPS2k a) before and b) after annealing for 12 h at 120°C.

Table 10. Areas of characteristic peaks of a h-LPS/ d-LPS blend film and a h-CPS/ d-LPS blend film before and after annealing using STOF-SIMS.[a]

Composition	Annealing	h-PS signal	d-PS signal	Ratio
h-LPS/ d-LPS	No	121000	582000	4.8 (± 0.1)
(20 wt% h-LPS)	120°C, 12 h	166000	688000	4.1 (± 0.1)
h-CPS/ d-LPS	No	29000	227000	7.8 (± 0.2)
(20 wt% h-CPS)	120°C, 12 h	77000	737000	9.6 (± 0.2)

[a]The data presented here are from a single sample. The ratios listed in the text and Table 11 are averages from multiple samples.

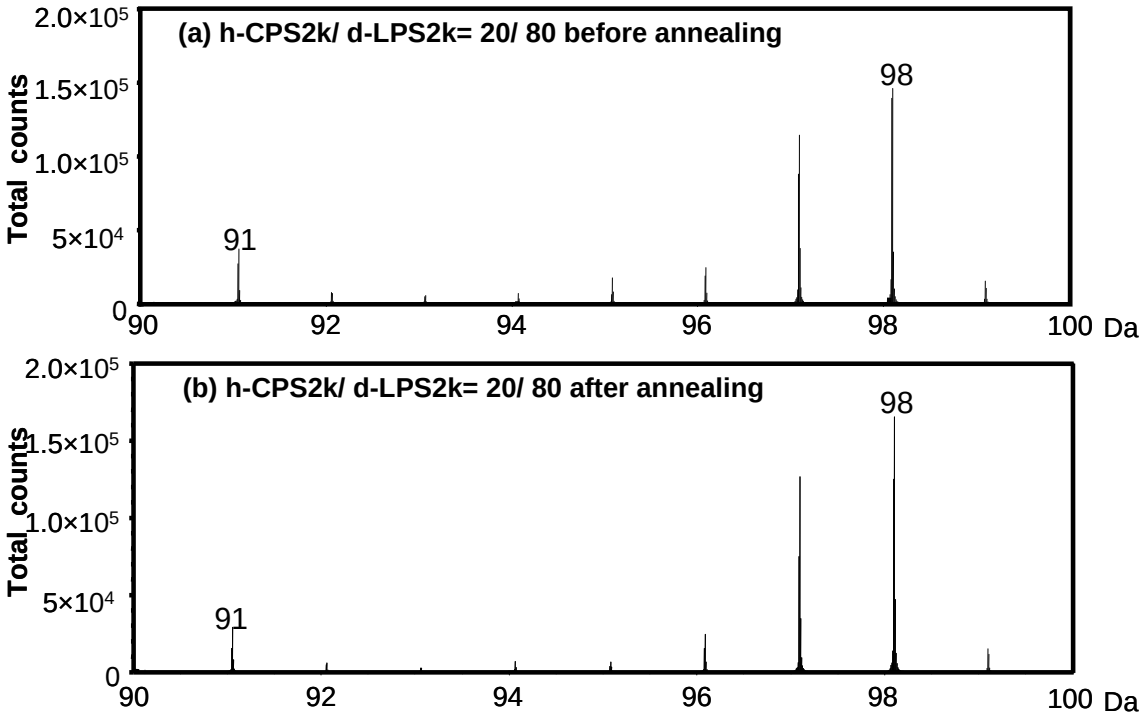

Figure 61. STOF-SIMS fragmentation spectrum of a h-CPS/d-LPS blend containing 80 wt% d-LPS a) before, and b) after annealing for 12 h at 120°C.

The trend observed with the STOF-SIMS data is the same as that observed with the SL-MALDI-TOF MS. It is clear from the SIMS data that when the ratio of deuterated linear to hydrogenous linear polymer at the surface is of the order of four, the d:h signal ratio is around four. Therefore, even if the SIMS ionization yields for cyclic and linear chains are somewhat different, the signal ratios of 7.3 and 9.8 suggest that the deuterated *linear* species is already enriched at the surface in the cyclic/linear blend after spin-casting and that this enrichment grows with annealing.

Table 11. Summary of surface composition in cyclic and linear blend films before and after annealing obtained with SL-MALDI-TOF MS.

Sample Type	Annealing	SL-MALDI-MS (wt% d-LPS)	STOF-SIMS Ratio d:h species
h-LPS/d-LPS	No	78.6 (± 2.5)	4.4 (± 0.6)
(20 wt% h-LPS)	120°C, 12 h	78.8 (± 2.9)	4.2 (± 0.1)
h-CPS/d-LPS	No	88.3 (± 1.6)	7.3 (± 0.4)
(20 wt% h-CPS)	120°C, 12 h	89.3 (± 2.8)	9.8 (± 0.3)

The discrepancy between the experimental results and the theoretical prediction for the linear/cyclic blend of low molecular weight species indicates that the SCFT does not capture some key features of the phenomena. One possible cause of the discrepancy could be the fact that short chains, particularly cyclic chains, do not exhibit Gaussian chain conformations as

assumed by SCFT. The chain packing would be very different in this case. Recently, the surface segregation in the blend of linear and low molecular weight cyclic chains has been investigated using the Wall-Polymer Reference Interaction Site Model (Wall-PRISM). PRISM theory accounts for packing effects in liquids. Wall-PRISM theory, introduced by Yethiraj,[74,75] is an extension of PRISM theory specifically designed to handle the packing behavior of polymers next to a wall. The wall can be modeled as more or less hard, with a soft wall representing an interface with a fluid such as air and a hard wall representing the interface with the substrate. When the surface segregation behavior of the cyclic/linear is modeled using Wall-PRISM theory[76], a surface *depletion* of cyclic chains is predicted. This indicates that the Wall-PRISM model more accurately captures the behavior of the cyclic/linear blend and is consistent with our experiment results.

Making the SL-MALDI Technique More Cost Effective

In the measurements discussed above, the conductive substrate used in preparing the sample for the SL-MALDI measurement was 50 nm of gold. This substrate was made by depositing a 10 nm layer of chromium onto a silicon wafer to act as an adhesive, and further depositing a 50 nm layer of gold on top of the chromium adhesive layer. While effective, these substrates are both expensive and time consuming to make. In particular, the especially high vacuum needed for deposition of chromium as well as the high cost of gold are both barriers to wider use of the technique. Ideally, replacing the gold conductive substrate with silver would expedite the substrate fabrication and decrease the per sample cost. In order to make the switch from gold to silver, it was first essential to demonstrate that changing the substrate does not affect the mass spectrometry results through a change in ionization efficiency or peak position.

To test the substrate effects, two identical blend samples were made, one on a gold conductive substrate and the other on a silver conductive substrate. The samples were spun from a 1% solution of 5 kg/mol d-LPS/h-LPS blend containing 80 wt % of the d-LPS species. The samples were annealed in a high vacuum oven for 6.5 hours at 105°C. The resulting SL-MALDI-TOF-MS spectra are compared in Fig. 62. The peak positions and the measured ratio between deuterated and hydrogenous material were found to agree within experimental error for the two substrates. This confirms that the silver substrate is a viable replacement for the gold substrate for SL-MALDI-TOF measurements.

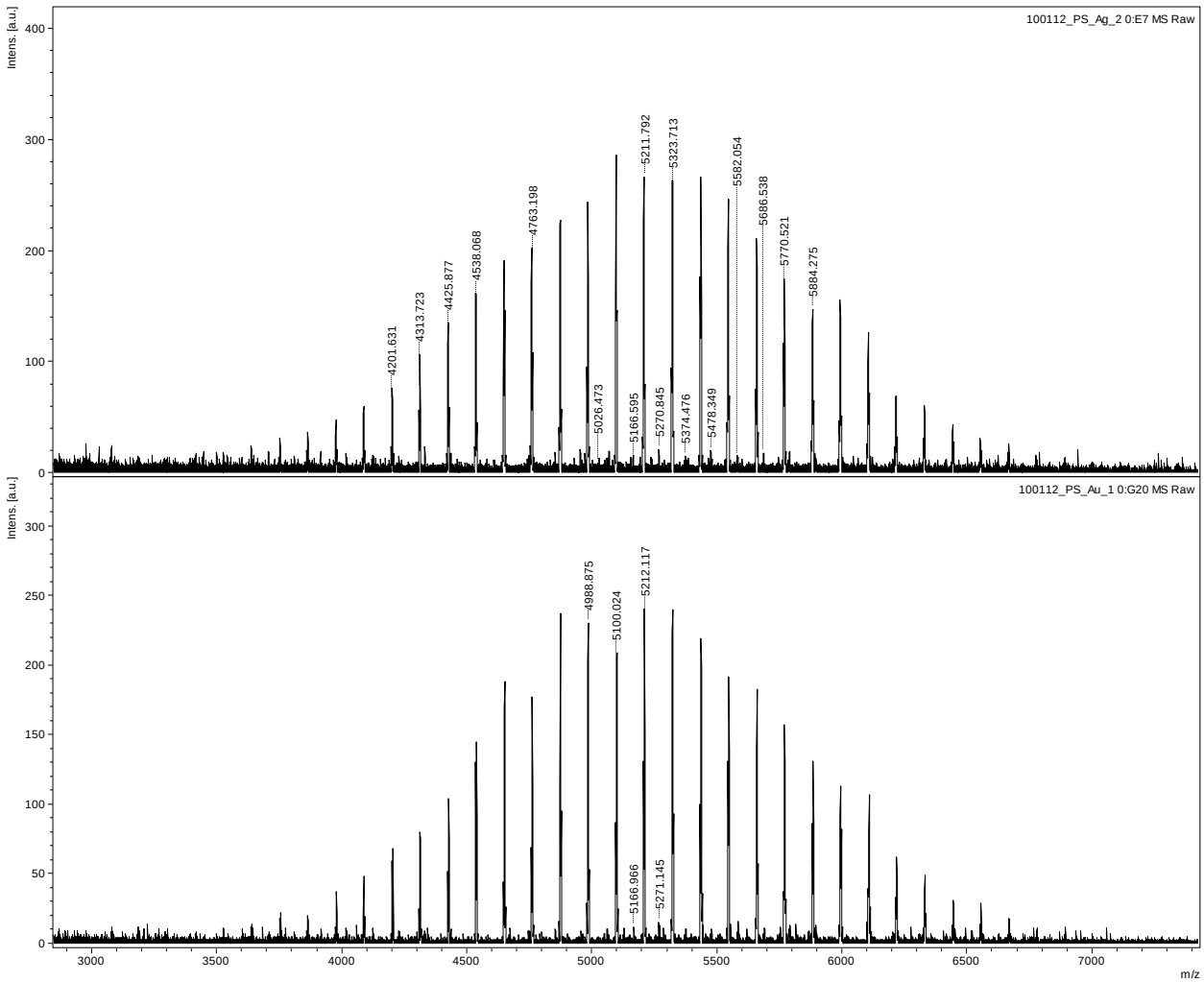

Figure 62. SL-MALDI-TOF MS spectra showing distributions for a 5 kg/mol blend of d-LPS/h-LPS containing 80 wt % of the d-LPS species on silver (top) and gold (bottom). The peak positions and ratios are in agreement within experimental error.

In summary, a new technique, SL-MALDI-TOF MS, was developed to quantitatively study the surface composition of polymer blends in the UA home laboratory. This new technique, with a monomolecular probing depth, can be used to characterize standards to test if TERS blinking can be used to quantitatively investigate the surface composition of polymer blends.

Summary

Significant progress has been achieved on developing material design principles for optimizing optically inactive ultrathin coatings that enhance the lifetimes of plasmonic structures useful for two transformational technologies: high resolution optical spectroscopies for characterization of material surfaces and very high sensitivity, highly selective detection of chemical, biological, and explosive threats in air or aqueous environments using surface enhanced Raman spectroscopy (SERS). These plasmonic structures could be nanoparticles, nanoparticle arrays or clusters, rough coatings on scanning probe tips, or complex compound structures. Characterization of the chemical composition and roughness of ultrathin protective

alumina oxide coatings on silver plasmonic structures has been performed and the composition of the protective coating was confirmed to be Al_2O_3. Changes in the optical spectra of silver metallized tips before and after deposition of a protective coating have been quantified over a time span of two weeks. The optical spectra were observed to vary significantly from tip to tip, even without aging. Progress was also made in determining to what degree a protective coating prevents morphological changes in plasmonic structures on tips with heating as well as scanning. The alumina protected tips were observed to last at least 2x longer than unprotected tips when scanning a hard, silicon grating. The same protective coating extends the chemical stability of silver nanostructures to three months when stored in a dessicator.

Protected silver films were subjected to various aqueous environments to improve plasmonic structure robustness for *in-situ* measurements. The optimal structure on a flat substrate was found to be an alumina protected silver film with an underlying chromium adhesive layer. Silica and DLC protected silver films were also investigated. The silica coatings did provide some protection, but did not preserve underlying morphology as well as the alumina coatings when exposed to aqueous environments. The DLC coatings were found to be inferior under all aqueous conditions investigated.

Extreme enhancement was observed using TERS probes. Using protected probes, insight into the mechanism behind this phenomenon was obtained. Results are consistent with thermal diffusion of molecules into and then back out of hot spots as the predominate mechanism behind blinking. The ability to distinguish isotopic polymeric species with TERS was also demonstrated for the first time using a nonresonant analyte. A new technique, SL-MALDI-TOF MS, was developed to quantitatively study the surface composition of polymer blends in the UA home laboratory. This new technique, with a monomolecular probing depth, can be used to characterize standards for testing if TERS blinking can be used to quantitatively investigate the surface composition of blend films. Replacing the gold substrates for SL-MALDI-TOF MS with silver substrates will make the technique more cost effective.

References:

1. Agapov, R. L.; Sokolov, A. P.; Foster, M. D. *J. Raman Spectro.* **2012,** In final review prior to submission.
2. Wang, S.-F.; Li, X.; Agapov, R. L.; Wesdemiotis, C.; Foster, M. D. *ACS Macro Letters* **2012,** 1, 1024-1027.
3. Agapov, R. L.; Sokolov, A. P.; Foster, M. D. *Proc. of SPIE Vol. 8378* **2012**, 837813.
4. Wytenburg, W. J.; Lambert, R. M. *J. Vac. Sci. Technol. A.* **1992,** 10, 3597-3608.
5. Donnett, C.; Grill, A. *Surf. Coat. Tech.* **1997,** 94-95, 456-462.
6. Mehtani, D.; Lee, N.; Hartschuh, R. D.; Kisliuk, A.; Foster, M. D.; Sokolov, A. P.; Čajko, R.; Tuskerman, I. *J. Opt. A.: Pure Appl. Opt.* **2006,** 8, S183-S190.
7. Mehtani, D.; Lee, N.; Hartschuh, R. D.; Kisliuk, A.; Foster, M. D.; Sokolov, A. P.; Tsukerman, I. *J Opt. A: App. Pure Opt.* **2005,** 36, 1068-1075.
8. Wagner, C. D.; Naumkin, A. V.; Kraut-Vass, A.; Allison, J. W.; Powell, C. J.; Rumble, J. R., Jr., NIST X-ray Photoelectron Spectroscopy Database (V3.5). 2007.
9. Reichel, F.; Jeurgens, L. P. H.; Richter, G.; Mittemeijer, E. J. *J. Appl. Phys.* **2008,** 103, 093515/1-093515/10.
10. Barrios, C. A.; Malkovskiy, A. v.; Kisliuk, A. M.; Sokolov, A. P.; Foster, M. D. *J. Phys. Chem. C* **2009,** 113, 8158-8161.
11. Kundu, S.; Hazra, S.; Banerjee, S.; Sanyal, M. K.; Mandal, S. K.; Chaudhuri, S.; Pal, A. K. *J. Phys. D: Appl. Phys.* **1998,** 31, L73-L77.
12. Reiter, G.; Bubeck, C.; Stamm, M. *Langmuir* **1992,** 8, 1881-1884.
13. Shipway, A. N.; Lahav, M.; Gabai, R.; Willner, I. *Langmuir* **2000,** 16, 8789-8795.
14. Cañamares, M. V.; Garcia-Ramos, J. V.; Gómez-Varga, J. D.; Domingo, C.; Sanchez-Cortes, S. *Langmuir* **2005,** 21, 8546-8553.
15. Zhang, W.; Schmid, T.; Yeo, B. S.; Zenobi, R. *J. Phys. Chem. C* **2008,** 112, 2104-2108.
16. *CRC Materials Science and Engineering Handbook*. CRC Press: New York, NY, 2001.
17. *Materials Handbook*. McGraw-Hill: New York, 1997.
18. Benck, R. F.; Crisco, C.; Spies, H. L. *J. Vac. Sci. Technol.* **1973,** 10, 562-563.
19. Budnitzki, M.; Pierron, O. *Appl. Phys. Lett.* **2009,** 94, 141906/1-141906/3.
20. Haanappel, V. A. C.; van Corbach, H. D.; Fransen, T.; Gellings, P. J. *Surf. Coat. Tech.* **1994,** 63, 145-153.
21. Smith, D. L., *Thin-Film Deposition Principles & Practice*. McGraw-Hill, Inc.: New York, 1995.
22. Liu, Y.; Erdemir, A.; Meletis, E. I. *Surf. Coat. Tech.* **1996,** 82, 48-56.
23. Crombez, R.; McMinis, J.; Veerasamy, V. S.; Shen, W. *Tribol. Int.* **2011,** 44, 55-62.
24. Eryilmaz, O. L.; Erdemir, A. *Surf. Coat. Tech.* **2007,** 201, 7401-7407.
25. Chiba, K.; Tada, M. *Thin Solid Films* **2012,** 520, 1993-1996.
26. Nie, S.; Emory, S. R. *Science* **1997,** 275, 1102-1106.
27. Kneipp, K.; Wang, Y.; Kneipp, H.; Perelman, L. T.; Itzkan, I.; Dasari, R.; Feld, M. S. *Phys. Rev. Lett.* **1997,** 78, 1667-1670.
28. Michaels, A. M.; Jiang, J.; Brus, L. *J. Phys. Chem. B* **2000,** 104, 11965-11971.
29. Xu, H.; Bjerneld, E. J.; Käll, Bŏrjesson, L. *Phys. Rev. Lett.* **1999,** 83, 4357-4360.
30. Neacsu, C. C.; Dreyer, J.; Behr, N.; Raschke, M. B. *Phys. Rev. B* **2006,** 73, 193406-193409.
31. Domke, K. F.; Zhang, D.; Pettinger, B. *J. Phys. Chem. C* **2007,** 111, 8611-8616.
32. Zhang, W.; Yeo, B. S.; Schmid, T.; Zenobi, R. *J. Phys. Chem. C* **2007,** 111, 1733-1738.
33. Ichimura, T.; Watanabe, H.; Morita, Y.; Verma, P.; Kawata, S.; Inouye, Y. *J. Phys. Chem. C* **2007,** 111, 9460-9464.
34. Xie, X. S.; Trautmann, J. K. *Annu. Rev. Phys. Chem.* **1998,** 49, 441-480.
35. Futamata, M. J. *Faraday Discuss.* **2006,** 132, 45-61.
36. Camden, J. P.; Dieringer, J. A.; Wang, Y.; Masiello, D. J.; Marks, L. D.; Schatz, G. C.; Van Duyne, R. P. *J. Amer. Chem. Soc.* **2008,** 130, 12616-12617.
37. Theiss, J.; Pavaskar, P.; Echternach, P. M.; Muller, R. E.; Cronin, S. B. *Nano Lett.* **2010,** 10, 2749-2754.
38. Futamata, M.; Y., M.; Ishikawa, M. *Vib. Spectrosc.* **2002,** 30, 17-23.
39. Busbee, B. D.; Obare, S. O.; Murphy, C. J. *Adv. Mater.* **2003,** 15, 414-416.
40. Wu, H.-Y.; Chu, H.-C.; Kuo, T.-J.; Kuo, C.-L.; Huang, M. H. *Chem. Mater.* **2005,** 17, 6447-6451.
41. van der Zande, B. M. I.; Koper, G. J. M.; Lekkerkerker, H. N. W. *J. Phys. Chem. B* **1999,** 103, 5754-5760.
42. van der Zande, B. M. I.; Böhmer, M. R.; Fokkink, L. G. J.; Schönenberger, C. *Langmuir* **1999,** 16, 451-458.
43. Jain, P. K.; Eustis, S.; El-Sayed, M. A. *J. Phys. Chem. B* **2006,** 110, 18243-18253.
44. Funston, A. M.; Novo, C.; Davis, T. J.; Mulvaney, P. *Nano Lett.* **2009,** 9, 1651-1658.
45. Garreau, S.; Louarn, G.; Buisson, J. P.; Froyer, G.; Lefrant, S. *Macromolecules* **1999,** 32, 6807-6812.

46. Agapov, R. L.; Malkovskiy, A. V.; Sokolov, A. P.; Foster, M. D. *J. Phys. Chem. C* **2011,** 115, 8900-8905.
47. Malkovskiy, A. V.; Malkovsky, V. I.; Kisliuk, A. M.; Barrios, C. A.; Foster, M. D.; Sokolov, A. P. *J. Raman Spectrosc.* **2009,** 40, 1349-1354.
48. *CRC Handbook of Chemistry and Physics*. 84th ed.; CRC Press: New York, 2003.
49. Piranha etching consists of using hydrogen peroxide and sulfuric acid, which can be dangerous. Acid-resistant gloves, protective goggles, and lab coats must be worn when handling the piranha solution.
50. Otto, A. *J. Raman Spectrosc.* **2002,** 33, 593-598.
51. Ishikawa, M.; Maruyama Ye, M. J.; Futamata, M. *J. Biol. Phys.* **2002,** 28, 573-585.
52. Ishikawa, M.; Ye, J. Y.; Maruyama, Y.; Futamata, M. *J. Lumin.* **2002,** 98, 81-89.
53. Maruyama, Y.; M., I.; Futamata, M. J. *J. Phys. Chem. B* **2004,** 108, 673-378.
54. Maruyama, Y.; Ishikawa, M.; Futamata, M. J. *J. Phys. Chem. B* **2004,** 108, 13119-13127.
55. Emory, S. R.; Jensen, R. A.; Wenda, T.; Han, M.; Nie, S. *Faraday Discuss.* **2006,** 132, 249-259.
56. Weiss, A.; Haran, G. J. *J. Phys. Chem. B* **2001,** 105, 12348-12354.
57. Lukatsky, D. B.; Haran, G.; Safran, S. A. *Phys. Rev. E* **2003,** 67, 062402/1-062402/4.
58. Jiang, J.; Bosnick, K.; Maillard, M.; Brus, L. E. *J. Phys. Chem. B* **2003,** 107, 9964-9972.
59. Le Ru, E. C.; Blackie, E.; Meyer, M.; Etchegoin, P. G. *J. Phys. Chem. C* **2007,** 111, 13794-13803.
60. Sonntag, M. D.; Klingsporn, J. M.; Gairbay, L. K.; Roberts, J. M.; Dieringer, J. A.; Seideman, T.; Schedit, K. A.; Jensen, L.; Schatz, G. C.; Van Duyne, R. P. *J. Phys. Chem. C* **2012,** 116, 478-483.
61. Hong, P. P.; Boerio, F. J.; Clarson, S. J.; Smith, S. D. *Macromolecules* **1991,** 24, 4770-4776.
62. MacDonald, R. J.; King, B. V., SIMS - Secondary Ion Mass Spectrometry. In *Surface Analysis Methods in Materials Science*, 1st ed.; O'Connor, D. J.; Sexton, B. A.; Smart, R. S. C., Eds. Springer-Verlag: New York, 1992.
63. Hariharan, A.; Kumar, S. K.; Russell, T. P. *J. Chem. Phys.* **1993,** 98, 4163-4173.
64. Sikka, M.; Singh, N.; Karim, A.; Bates, F. S.; Satija, S. K.; Majkrzak, C. F. *Phys. Rev. Lett.* **1993,** 70, 307-310.
65. Walton, D. G.; Soo, P. P.; Mayes, A. M.; Allgor, S. J. S.; Fujii, J. T.; Griffith, L. G.; Ankner, J. F.; Kaiser, H.; Johansson, J.; Smith, G. D.; Barker, J. G.; Satija, S. K. *Macromolecules* **1997,** 30, 6947-6956.
66. Dabney, D. E. Analysis of Synthetic Polymers by Mass Spectrometry and Tandem Mass Spectrometry. The Univerisity of Akron, Akron, 2009.
67. Wesdemiotis, C.; Solak, N.; Polce, M. J.; Dabney, D. E.; Chaicharoen, K.; Katzenmeyer, B. C. *Mass Spectrom. Rev.* **2011,** 30, 523-559.
68. Rader, H. J.; Schrepp, W. *Acta Polym.* **1998,** 49, 272-293.
69. Knochenmuss, R. *Anal. Chem.* **2004,** 76, 3179-3184.
70. Zenobi, R.; Knochenmuss, R. *Mass Spectrom. Rev.* **1998,** 17, 337-366.
71. Knochenmuss, R. Z., R. *Chem. Rev.* **2003,** 103, 441-452.
72. Quirk, R. P.; Wang, S.; Foster, M. D.; Wesdemiotis, C.; Yol, A. M. *Macromolecules* **2011,** 44, 7538-7545.
73. Jones, R. A. L.; Kramer, E. J.; Rafailovich, M. H.; Sokolov, J.; Schwarz, S. A. *Phys. Rev. Lett.* **1989,** 62, 280-283.
74. Yethiraj, A. *Chem. Eng. J.* **1999,** 74, 109-115.
75. Yethiraj, A.; Hall, C. K. *J. Chem. Phys.* **1991,** 95, 3749.
76. Tormet, C.; Wu, D. T., Unpublished results. 2011.